

AD \_\_\_\_\_

Award Number: W81XWH-12-1-0159

TITLE: Screening and Monitoring Response to Treatment Using Subsecond Molecular Imaging and Hyperpolarized Contrast Agents

PRINCIPAL INVESTIGATOR: Eduard Y. Chekmenev, Ph.D.

CONTRACTING ORGANIZATION: Vanderbilt University  
Nashville, TN 37240-0001

REPORT DATE: May 2013

TYPE OF REPORT: Annual

PREPARED FOR: U.S. Army Medical Research and Materiel Command  
Fort Detrick, Maryland 21702-5012

DISTRIBUTION STATEMENT: Approved for Public Release;  
Distribution Unlimited

The views, opinions and/or findings contained in this report are those of the author(s) and should not be construed as an official Department of the Army position, policy or decision unless so designated by other documentation.

# REPORT DOCUMENTATION PAGE

*Form Approved  
OMB No. 0704-0188*

Public reporting burden for this collection of information is estimated to average 1 hour per response, including the time for reviewing instructions, searching existing data sources, gathering and maintaining the data needed, and completing and reviewing this collection of information. Send comments regarding this burden estimate or any other aspect of this collection of information, including suggestions for reducing this burden to Department of Defense, Washington Headquarters Services, Directorate for Information Operations and Reports (0704-0188), 1215 Jefferson Davis Highway, Suite 1204, Arlington, VA 22202-4302. Respondents should be aware that notwithstanding any other provision of law, no person shall be subject to any penalty for failing to comply with a collection of information if it does not display a currently valid OMB control number. PLEASE DO NOT RETURN YOUR FORM TO THE ABOVE ADDRESS.

<b>1. REPORT DATE</b> May 2013			<b>2. REPORT TYPE</b> Annual		<b>3. DATES COVERED</b> 1 May 2012 – 30 April 2013	
<b>4. TITLE AND SUBTITLE</b>  Screening and Monitoring Response to Treatment Using Subsecond Molecular Imaging and Hyperpolarized Contrast Agents			<b>5a. CONTRACT NUMBER</b>			
			<b>5b. GRANT NUMBER</b> W81XWH-12-1-0159			
			<b>5c. PROGRAM ELEMENT NUMBER</b>			
<b>6. AUTHOR(S)</b>  Eduard Y. Chekmenev, Ph.D.  E-Mail: eduard.chekmenev@vanderbilt.edu			<b>5d. PROJECT NUMBER</b>			
			<b>5e. TASK NUMBER</b>			
			<b>5f. WORK UNIT NUMBER</b>			
<b>7. PERFORMING ORGANIZATION NAME(S) AND ADDRESS(ES)</b>  Vanderbilt University Nashville, TN 37240-0001			<b>8. PERFORMING ORGANIZATION REPORT NUMBER</b>			
			<b>10. SPONSOR/MONITOR'S ACRONYM(S)</b>			
<b>9. SPONSORING / MONITORING AGENCY NAME(S) AND ADDRESS(ES)</b> U.S. Army Medical Research and Materiel Command Fort Detrick, Maryland 21702-5012			<b>11. SPONSOR/MONITOR'S REPORT NUMBER(S)</b>			
			<b>12. DISTRIBUTION / AVAILABILITY STATEMENT</b> Approved for Public Release; Distribution Unlimited			
<b>13. SUPPLEMENTARY NOTES</b>						
<b>14. ABSTRACT</b> We have been developing low-field MRI of breast cancer using hyperpolarized contrast agents capable of interrogating metabolic pathways <i>in vivo</i> . While this five-year project has several objectives, the main areas of focus according to the approved Statement of Work for Year 1 were (i) design and development of second-generation xenon-129 automated polarizer, and (ii) optimization of preclinical low-field MRI system. Our team has designed the polarizer and, through a series of prototyping efforts, began xenon-129 polarizer construction. While the polarizer construction and automation is to be finished in Year 2, we demonstrated very high level of xenon-129 polarization, including values approaching 100% for xenon-129 at densities needed to produce multi-gram quantities sufficient for clinical research: the ultimate goal of our efforts. Besides improving the polarization benchmarks over our first-generation polarizer (and any other polarizer operating in batch production mode) that is currently used in clinical research, the designed polarizer will also be significantly more automated, compact, and adaptable. We were also able to optimize our RF coil performance for the pre-clinical MRI system from the perspective of maximizing signal-to-noise ratios for carbon-13 imaging and proton imaging. Imaging studies on phantoms have been completed and we are now planning imaging experiments in tumor-bearing mice during the next Year of funding. The up-to-date results of both arms of the projects described above were presented at scientific conference meetings, and they are either already submitted as manuscripts to peer-reviewed scientific journals or will be prepared during Year 2. We have also demonstrated the <i>in vivo</i> utility of one metabolic carbon-13 contrast agent in an animal model of breast cancer. This tracer, 1-13C-phospholactate, is chosen to be evaluated in preclinical low-field MRI studies. Overall, our team significantly progressed with contrast agent validation, polarizing, and imaging instrumentation development, which will enable our long-term progress towards the ultimate goal of developing a suite of tools involving imaging, polarization, and chemistry of contrast agents for sub-second molecular imaging of breast cancer.						
<b>15. SUBJECT TERMS</b> Low-field breast cancer MRI, molecular imaging, response to treatment, breast cancer screening						
<b>16. SECURITY CLASSIFICATION OF:</b>			<b>17. LIMITATION OF ABSTRACT</b> UU	<b>18. NUMBER OF PAGES</b> 57	<b>19a. NAME OF RESPONSIBLE PERSON</b> USAMRMC	
<b>a. REPORT</b> U	<b>b. ABSTRACT</b> U	<b>c. THIS PAGE</b> U	<b>19b. TELEPHONE NUMBER (include area code)</b>			

## Table of Contents

	<u>Page</u>
<b>INTRODUCTION .....</b>	<b>4</b>
<b>BODY .....</b>	<b>5</b>
TASK 1.A. <sup>129</sup> XE POLARIZER: DESIGN .....	5
1. <i>Gas-handling manifold</i> .....	5
2. <i>VHG-narrowed 200 W LDA module</i> .....	6
3. <i>Variable-temperature (VT) oven</i> .....	6
4. <i>Electromagnet</i> .....	7
5. <i>Low-field NMR spectrometer with <i>in situ</i> detection</i> .....	7
6. <i>In situ infrared (IR) spectroscopy</i> .....	8
7. <i>Micro-controller</i> .....	8
8. <i>Integrating Frame / Chassis</i> .....	8
TASK 1.B. <sup>129</sup> XE POLARIZER: CONSTRUCTION .....	8
1. <i>Completed construction Work</i> .....	8
2. <i>Work in Progress on xenon-129 polarizer</i> .....	11
TASK 4.A. LOW FIELD MRI: PRE-CLINICAL DEVELOPMENT .....	12
TASK 4.B. LOW FIELD MRI: PRE-CLINICAL OPTIMIZATION .....	12
<b>KEY RESEARCH ACCOMPLISHMENTS .....</b>	<b>14</b>
<b>REPORTABLE OUTCOMES .....</b>	<b>14</b>
ORAL PRESENTATIONS .....	14
CONFERENCE ABSTRACTS .....	14
MANUSCRIPTS .....	15
FUNDING APPLIED FOR BASED ON WORK SUPPORTED BY THIS AWARD .....	15
<b>CONCLUSION .....</b>	<b>15</b>
<b>REFERENCES .....</b>	<b>15</b>
<b>APPENDICES .....</b>	<b>17</b>
APPENDIX 1: STATEMENT OF WORK, YEAR 1 .....	17
APPENDIX 2: PERFORMANCE EVALUATION FOR QPC LASER ES-6507-Z002, SN 1209201 .....	18
APPENDIX 3: ABSTRACTS PRESENTED .....	30
APPENDIX 4: MANUSCRIPTS PUBLISHED AND ACCEPTED .....	35

## Introduction

We are developing hyperpolarized MRI allowing for ultrafast (potentially sub-second) molecular imaging of breast cancer with specificity similar to that of FDG-PET, but significantly lower cost than conventional MRI due to much higher patient throughput/much faster exams and the use of low field = low cost MRI. We focus our research effort on the high-risk and critical challenges that must be solved to enable clinical implementation of hyperpolarized metabolic imaging of breast cancer.

To enable efficient imaging of these agents, this proposal explores the fundamental property of hyperpolarized contrast agents, namely large nuclear spin polarization, which is independent of the applied magnetic field used for MRI. This key feature of these agents allows for sub-second imaging with smaller (lower magnetic field), less costly scanners, while still achieving sensitivity comparable to, or greater than that of conventional high field MRI scanners.

Specifically, the research efforts during Year 1 have focused on two specific aims as described in Statement of Work:

**1) Preparation of pure hyperpolarized contrast agents approved for injection in humans**

**1.a.** Y1Q1-Y1Q3. Design of 2<sup>nd</sup> generation <sup>129</sup>Xe polarizer. The design took advantage of the design and development process of the 1<sup>st</sup> generation XENA device (1, 2), also see Appendix 3. Xenon-129 polarizer is needed to perform Xenon-Induced Polarization of <sup>13</sup>C-acetate and <sup>13</sup>C-pyruvate that will serve as hyperpolarized contrast agents of molecular imaging of breast cancer.

**1.b.** Y1Q4-Y2Q2. Construction of the open-source 2<sup>nd</sup> generation <sup>129</sup>Xe polarizer is an on-going process, which is reported here.

**2) Development of low field (low cost) sub-second *in vivo* imaging suitable for preclinical models of breast cancer and clinical trials**

**4.a.** Y1Q1-Y1Q2. Low field MRI: pre-clinical development was done based on our existing hardware that was developed during our preliminary work. The work focused on developing and construction of multiple RF coils intended for optimal direct and indirect detection of hyperpolarized contrast agents *in vivo*.

**4.b.** Y1Q3-Y1Q4. Low field MRI: pre-clinical optimization was conducted to optimize developed hardware and MRI sequences for specific metabolic contrast agents and their metabolites *in vivo*. Specifically, we optimized the detection sensitivity and developed a theoretical framework for future clinical scale RF coil designs as well as limits of detection sensitivity for low-field MRI.

## Body

### Task 1.a. $^{129}\text{Xe}$ Polarizer: design

The second-generation xenon-129 polarizer design was largely based on the first-generation device with significant improvements that enhance stability, polarization yield of the contrast agent, automation, ease of operation/maintenance, and future integration with xenon-induced polarization module and smaller footprint. The device consists of the following main components:

1. Gas-handling manifold;
2. VHG-narrowed 200 W laser diode array (LDA) module;
3. Variable temperature oven;
4. Electromagnet;
5. Low-field NMR spectrometer with *in situ* detection;
6. *In situ* infrared (IR) spectroscopy;
7. Micro-controller;
8. Integrating frame / chassis;

The design was largely performed using SolidWorks CAD software available to our team free of charge via the core facility at the Imaging Institute. Provided below is the description of the components' design.

#### 1. Gas-handling manifold

The gas-handling manifold achieves oxygen-free operation by always maintaining high-pressure (i.e. above atmospheric) conditions upstream of the cell, as shown in Fig. 1. The manifold is mounted on the aluminum plate that is precision cut as a part of the component 8, the integrating frame.

### XEUS-MRKII POLARIZER MANIFOLD SCHEMATIC (OPTIONAL: NITROGEN For Purge Cycles)

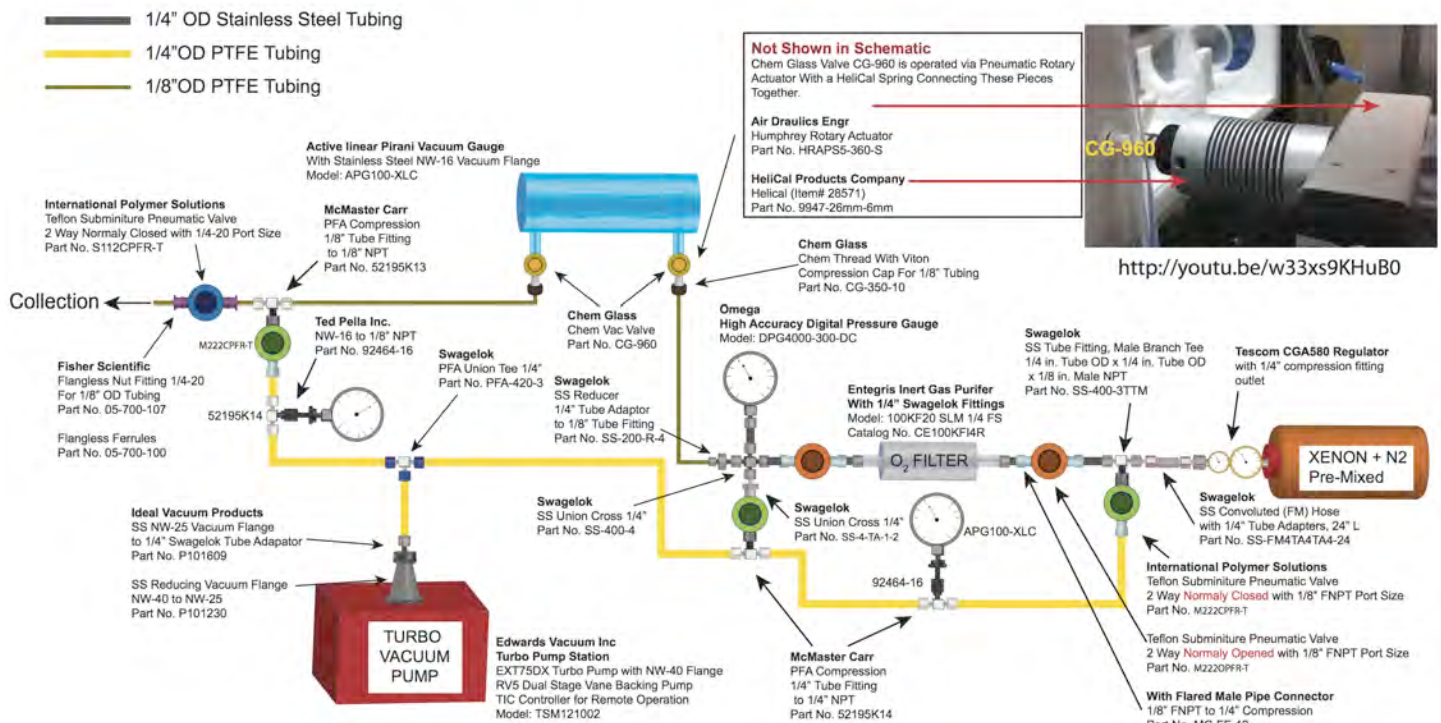


**Figure 1. Gas Loading Manifold Design.** By using a pre-mixed  $\text{Xe}/\text{N}_2$  gas cylinder, we have significantly reduced the number of pneumatic valves used from past designs—while also mitigating the purge cycle loading procedure, which vastly reduces the time required to load the Optical Pumping (OP)-Cell in preparation for the next run (increasing the overall HP $^{129}\text{Xe}$ -generating efficiency of the device). This approach also reduces the risk of O<sub>2</sub> contamination by always leaving the loading lines pressurized to the desired loading pressure, which are programmed via the microcontroller to re-pressurize if a drop in pressure is detected. The OP cell at the center of the polarizer is a 500 cc Pyrex cylinder with two stopcock-sealed valves to be

controlled by rotary actuators. Many such cells have now been delivered and may now be purchased as a stock part from our supplier (Midrivers Glass) guaranteed to fit our oven design (despite the otherwise inherently-custom nature of such glass pieces). Prior to gas loading and install, the cells are cleaned, coated with a siliconizing agent (Surfasil), loaded with ~200 mg Rb in an inert-atmosphere glove box, and the Rb is distributed as a thin film throughout the cell.

## 2. VHG-narrowed 200 W LDA module

The 200 W laser diode array (LDA) module consists of an LDA (internally narrowed via volume holographic grating (VHG) technology) purchased from a commercial vendor (QPC), which was approved in the original budget. We worked closely with the company to ensure that the laser module has an integrated optical train that delivers polarized light and expands it into a 2" OD beam that homogeneously irradiates the 2" optical pumping cell, Figs. 1-2. The module also contains two heat sinks providing efficient heat dissipation. The heat sink fans are gated by the micro-controller to suppress the background signal for high quality QA by *in situ* NMR spectroscopy. The laser temperature, which must be maintained constant to ensure operation at a desired output wavelength for optimal absorption by the Rb vapor, is controlled using a 1,400 W water chiller. Because laser performance is a key to overall polarization success of xenon-129 polarizer and because it is the first-of-its-kind integrated device made by this vendor, the SIUC team (Prof. Boyd Goodson lab) tested the performance of this laser and the results of this test are summarized in Appendix 2.

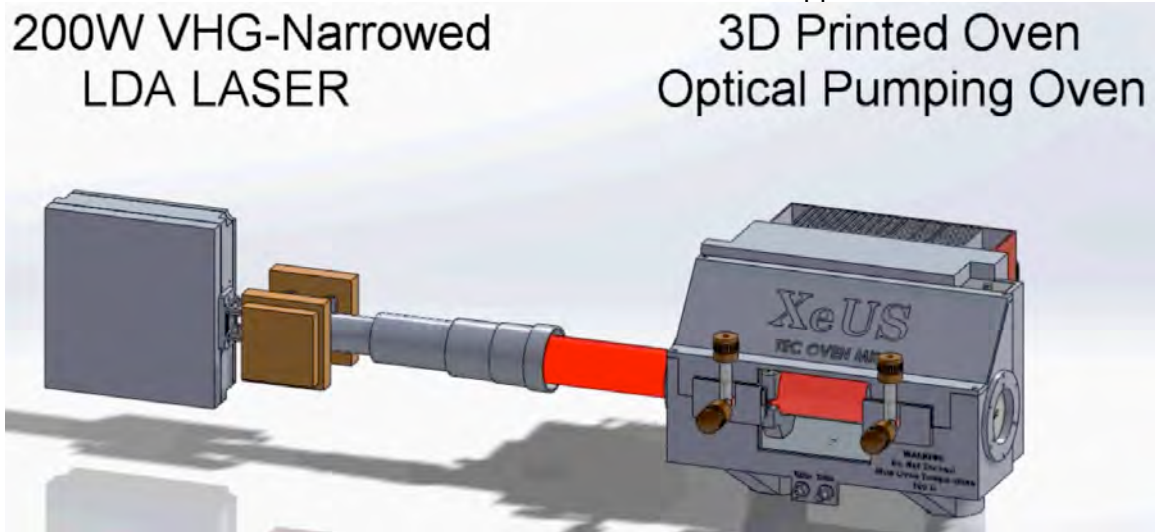


**Figure 2.** 200 W VHG-Narrowed LDA laser schematic aligned concentrically with the optical pumping oven.

## 3. Variable-temperature (VT) oven

The VT oven, Fig. 3, controls the surface temperature of the OP cell to maintain the Rb vapor density during spin-exchange optical pumping, the process by which spin angular momentum from circularly-polarized photons is converted into Rb electronic spin polarization, and ultimately, to  $^{129}\text{Xe}$  nuclear spin polarization. The oven was designed at VUIIS using SolidWorks CAD software and 3D printed in polycarbonate material in the laboratory of our collaborator Prof. Matthew Rosen (Harvard University). The oven also features a thermoelectric cooler (TEC)/heater that maintains oven temperature by controlling the temperature of flowing/re-circulating air pushed by an integrated blower. The resulting design does not require any chilling/cooling source besides electric power. That provides a clear advantage over the previous polarizer design (1, 3). The TEC module is controlled by a micro-controller for future complete automation during Year 2. The front on the oven has an optical flat allowing efficient transmission of the laser beam, while the back of the oven has a reflecting mirror to maximize the use of the laser flux (by providing a second pass of the beam through the OP cell) and improve the homogeneity of laser illumination along the OP the cell. The Oven also houses an RF coil for *in situ* NMR and a fiber optical cable in the back of the oven (not shown) for *in situ* IR spectroscopy. The NMR reports on the quality of the xenon-129 polarization, while the IR spectroscopy reports on the Rb polarization and the laser beam absorption.



**Figure 3.** Variable temperature (VT) oven housing the 0.5L (500 cc) optical pumping (OP) cell, 2" OD. The design and production using 3D printer is shown on the left and the exploded view is shown on the right.

#### 4. Electromagnet

The electromagnet utilizes a more efficient Barker coil design, Fig. 4. The design provides a homogenous magnetic field  $B_0$  for the optical polarization process and *in situ* NMR detection.

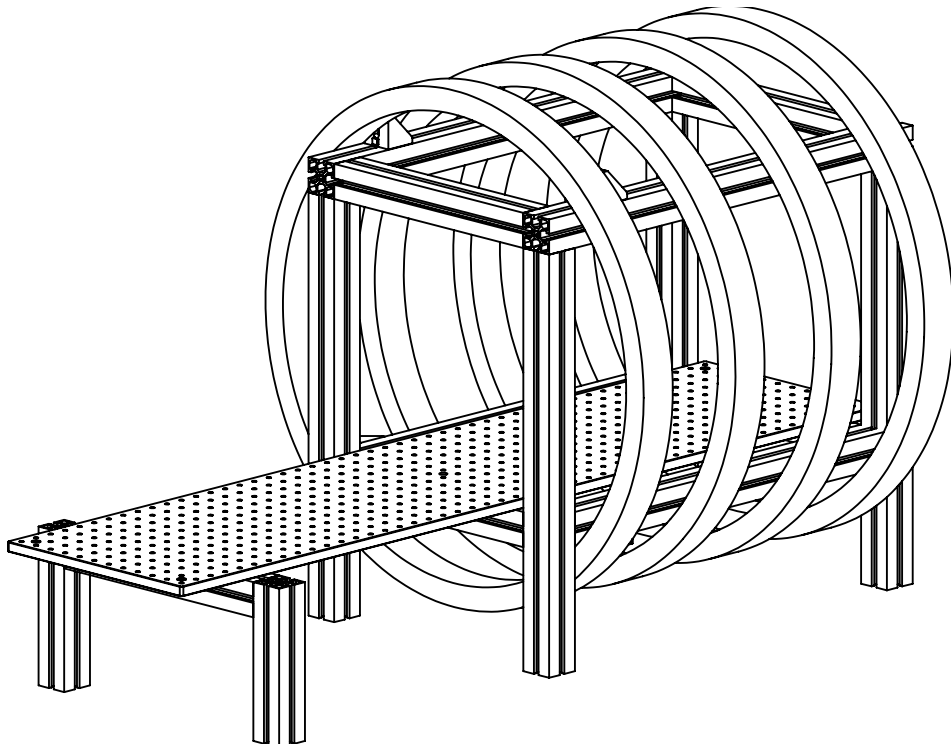


**Figure. 4.** Electromagnet design using four individual 23.6" OD coils comprising two 217 (outer) and two 96 (inner) turn coils. This Barker electromagnet coil design provides a sufficiently homogenous magnetic field that envelops the region of the OP cell while also embodying a more compact design (smaller footprint) compared to other coil configurations. The individual coils made by Acutran LP (Fombell, PA) and a custom-designed mechanism allows for primitive shimming of the magnetic field by moving the individual magnet coils with respect to each in four corners of the frame. The magnet coils are designed around the plane that houses VT oven.

#### 5. Low-field NMR spectrometer with *in situ* detection

Kea2 dual-channel NMR spectrometer, Magritek, New Zealand, with built-in 1 W (per channel) RF amplifier is used for *in situ* NMR detection capability. The spectrometer utilized an RF coil operating at 84 kHz and very recently was re-tuned to 47 kHz (work in progress). The RF coil is housed next to the OP cell and reports on the xenon-129 polarization. The advantage of lower-frequency detection is lower operating magnetic field

(which requires less energy and generates less waste heat). The NMR spectrometer can be triggered by the micro-controller.

## 6. *In situ* infrared (IR) spectroscopy

*In situ* IR spectroscopy is enabled with a HR4000 High-resolution User-configured Spectrometer, Ocean Optics, Dunedin, FL. This high-resolution IR spectrometer allows for monitoring the laser output spectral profile (including centroid wavelength, linewidth, and other features), as well as the Rb absorption spectral profile (including the fraction of laser light absorbed by the OP cell).

## 7. Micro-controller

The polarizer contains a micro-controller that utilizes the same design as previously described (1, 3), except that its shell was designed in SolidWorks CAD software for better integration with the Frame / Chassis (see below).

## 8. Integrating Frame / Chassis

The frame was designed using SolidWorks CAD software and precision cut to our design specifications by a private vendor (Minitec Systems LLC, Victor, NY). The frame integrates all components described above as well as other components: a silent air-compressor for actuating pneumatic valves, a vacuum pump (Edwards, vacuum level < 10 mTorr) and other minor electrical and ventilation components, Fig. 5. The frame also includes the mounting plates for the gas-handling manifold.

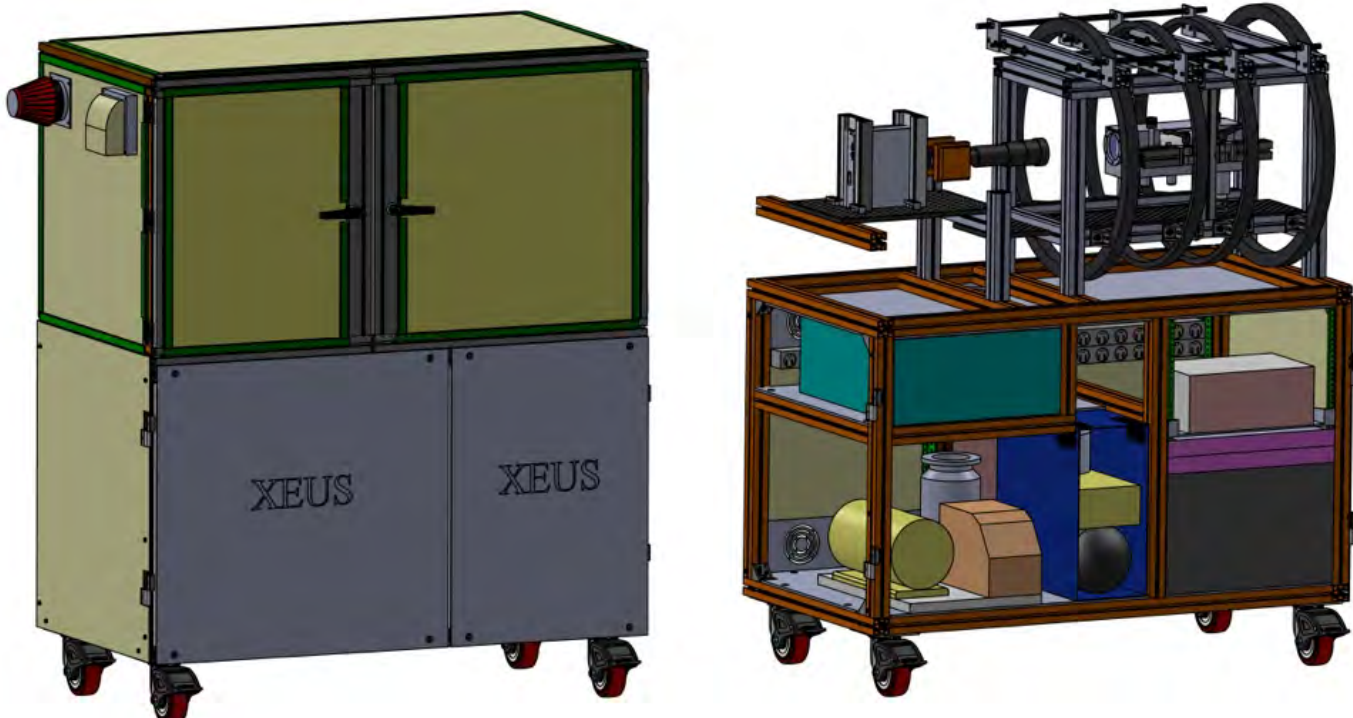


**Figure 5.** Polarizer 3D schematic rendering made during the design stages of the XeUS polarizer.

The overall design of xenon-129 polarizer was completed during Year 1 of the project.

### **Task 1.b. $^{129}\text{Xe}$ Polarizer: construction**

#### **1. Completed construction Work**

While the polarizer will be completed during the second year of the project, we have made significant progress with its construction. Nearly all components have been installed, Fig. 6, allowing for safe device operation in the manual polarization mode. The manual mode of operation does not currently allow recharging the cell with new batches of gas, but allows for device optimization, i.e. mapping optimal conditions for achieving maximum xenon-129 polarization. Two xenon density conditions were tested during Year 1: xenon : nitrogen 12.5% : 87.5% and 50% : 50% with total in cell pressure of 2000 Torr. These cells were prepared in the lab of co-PI

Prof. Boyd Goodson (SIU site). The preliminary optical pumping results, Fig. 7, are very encouraging indeed with record xenon-129 polarization levels, Fig. 8. The levels of xenon-129 polarization under these two conditions, Fig. 8c, are approaching the theoretical maximum of 100%. The *in situ* IR measurements of Rb polarization, Fig. 9, are in accord with the high xenon-129 polarization levels.

It should be noted that nearly all components have been assembled, although integration was not yet completed. The device integration and automation will be completed after optimal operating conditions are determined. Moreover, we have already demonstrated record levels of xenon-129 polarization in the partially completed device.

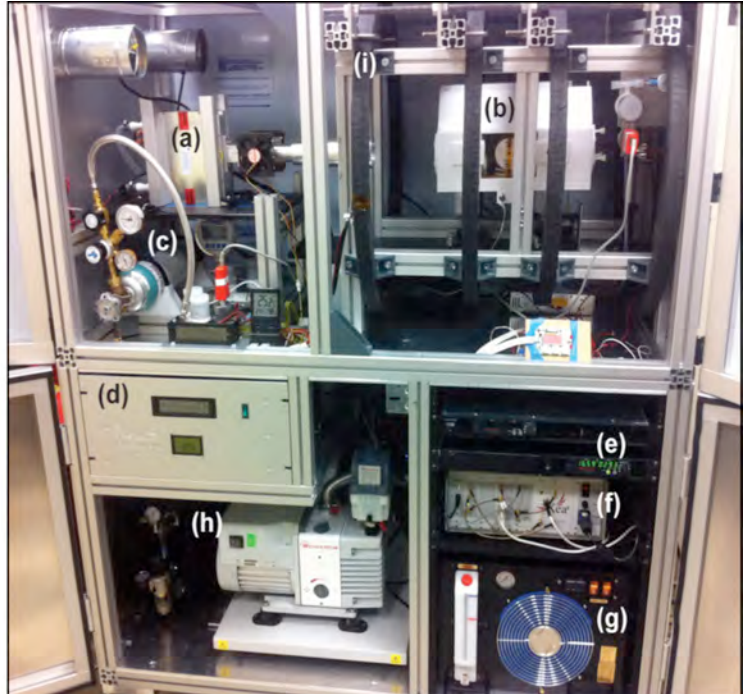
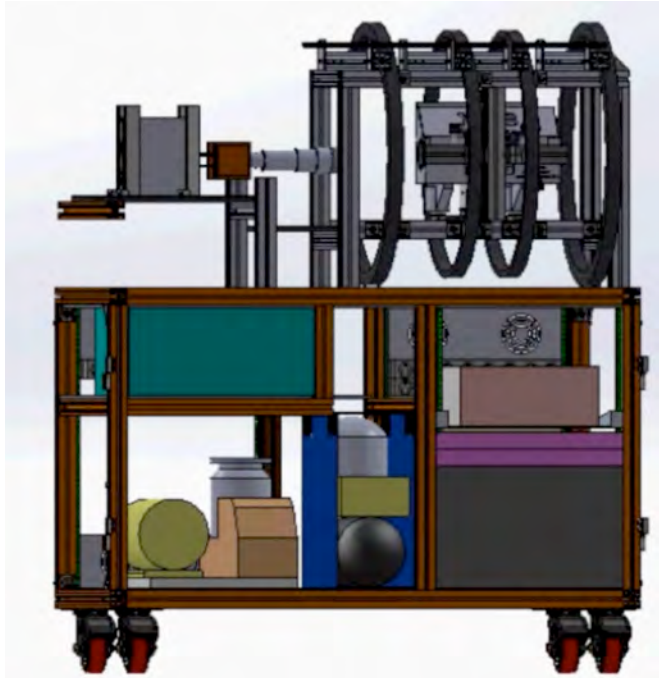


**Figure 6.** Left: design. Right: device under construction. XeUS Polarizer during testing phase: (a) 200 W VHG frequency-narrowed QPC laser with optical train aligned with OP cell producing 2" diameter beam @794.76 nm with a bandwidth of ~0.3 nm. (b) 3D Printed Optical Pumping Oven. (c) Gas loading manifold components. (d) Microcontroller box, responsible for controlling all pneumatic valves via GUI interface allowing manual and automated operation. (e) PSUs for Laser and Magnetic Coils. (f) Kea2 low-field NMR Spectrometer. (g) 1400 Watt Water Chiller for laser cooling. (h) Vacuum System and Air Compressor. (i)  $B_0$  Coil with Barker configuration.

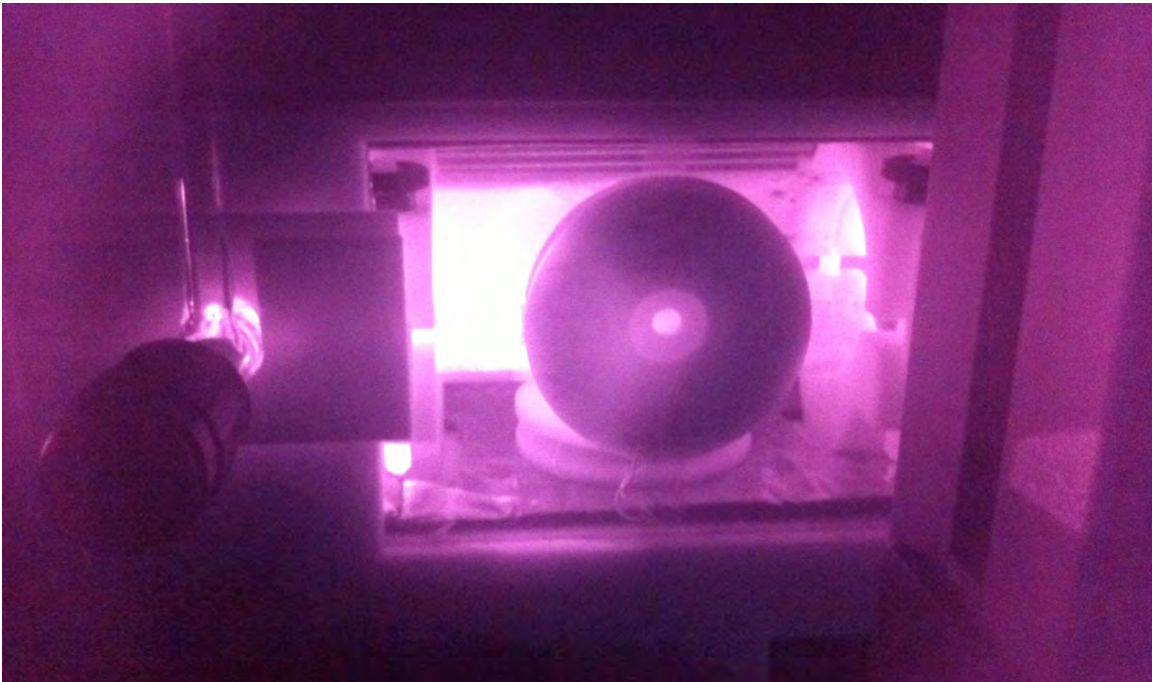


**Figure 7.** TEC oven during optical pumping with laser light illuminating the cell. The RF coil below the OP cell samples xenon-129 polarization *in situ*, Fig. 8.

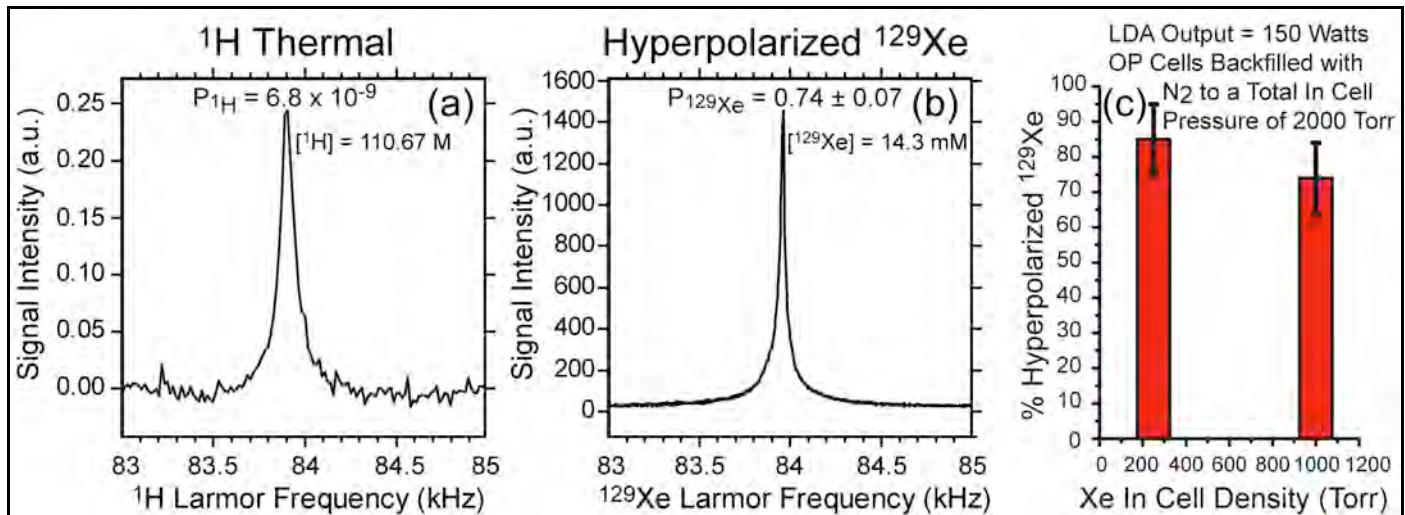


**Figure 8. *In situ* NMR spectroscopy at 84 kHz.** (a)  $^1\text{H}$  reference (Thermal) spectrum obtained from water,  $[^1\text{H}] = 110.7 \text{ M}$ , doped with 10 mM CuSO<sub>4</sub> inside 0.50 L OP cell. Spectrum was acquired at 84 kHz  $^1\text{H}$  Larmor frequency, with 100,000 averages using  $^1\text{H}$  thermal polarization  $P = 6.8 \times 10^{-9}$ . (b)  $^{129}\text{Xe}$  spectrum (nat. ab. = 26.44%) of 1000 torr Xe,  $[^{129}\text{Xe}] = 14.3 \text{ mM}$ , backfilled with N<sub>2</sub> to a total cell pressure of 2000 torr acquired at 84 kHz  $^{129}\text{Xe}$  Larmor frequency with 1 scan. *Both spectra were taken using the same circuit-detection coil with the same  $B_1$  tipping angle.* (c) Bar graph representing  $\%P_{xe}$  at 250 and 1000 torr with ~85% and 74% xenon polarization respectively.

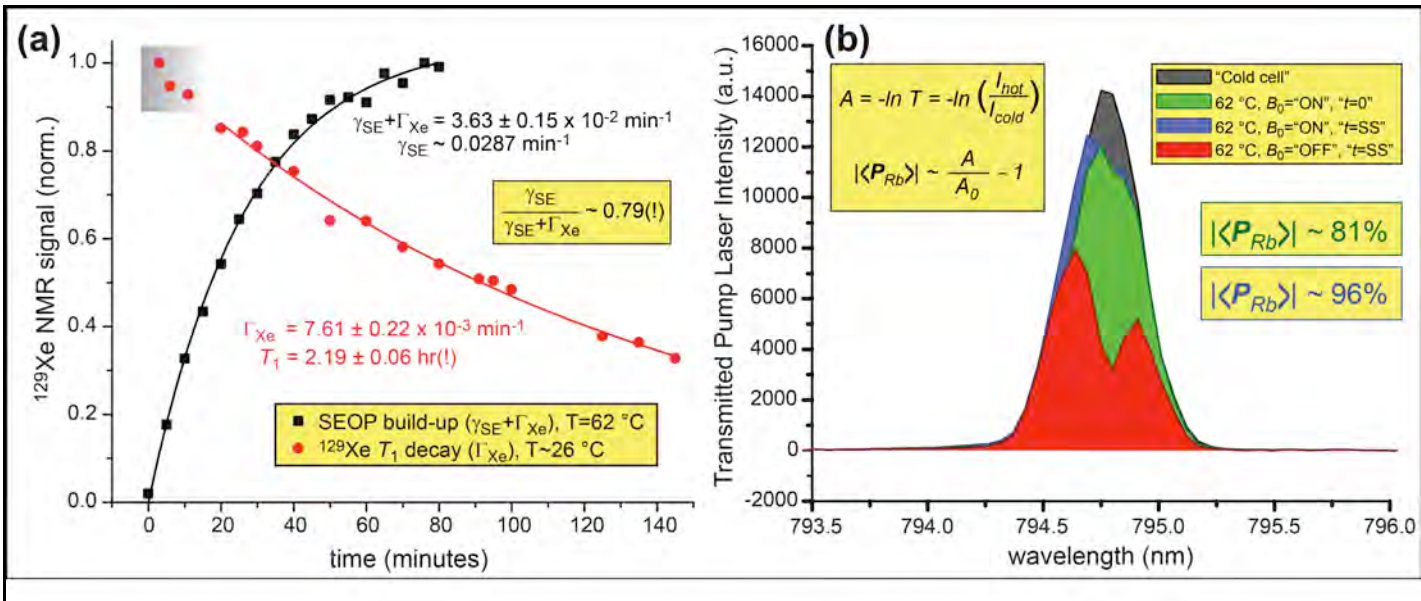


**Figure 9.** (a) Time-dependent *in situ*  $^{129}\text{Xe}$  low-field NMR for 1000 Torr Xe, 1000 Torr N<sub>2</sub>. The black curve is  $P_{Xe}$  build-up during SEOP at 62 °C; the red curve is subsequent  $^{129}\text{Xe}$  decay after the laser was turned off and the cell was cooled. Both datasets were fit to simple exponentials (curves); red data points were obtained with rf pulses possessing half the tipping angle. Red data points obtained before the cell reached room temperature (grey highlight) were not included in the fit. Losses from rf pulses were ignored during the fits. (b) *In situ* monitoring of global Rb electron spin polarization. Examples of near-IR spectra of the pump laser transmitted through the cell acquired under the following conditions: 1000 Torr Xe, 1000 Torr N<sub>2</sub>; room temperature ("cold cell"); 62 °C and  $B_0=7.13$  mT at the beginning of SEOP ("t=0"); 62 °C and  $B_0=7.13$  mT at steady-state for  $P_{Xe}$  ("t=SS", see adjacent figure); and 62 °C and  $B_0=0$  mT at steady-state. The large changes in transmitted laser intensity when the field is cycled indicate high Rb electronic spin polarization (see inset).

## 2. Work in Progress on xenon-129 polarizer

The polarizer construction work is still ongoing from the perspective of identifying the optimal operating conditions, completing device automation using the constructed micro-controller box, and testing the constructed gas-handling manifold. We will utilize the same Rb filter/getter as in the first-generation device. In case if it will be insufficient, a cold trap ( $t < 0$  °C) to catch residual Rb will be implemented using a TEC-cooled trap.

### Task 4.a. Low field MRI: pre-clinical development

We have developed and constructed low-field preclinical imaging system for mouse imaging in collaboration with Magritek, New Zealand. While the imager was developed prior the beginning of this project, the development of dedicated RF coil for low-field MRI was essential for the progress of preclinical optimization from the perspective of optimization of signal-to-noise ratio, which will ultimately determined the limits of spatial and temporal resolution. Fig. 10 below provides the summary of our pre-clinical MRI system.

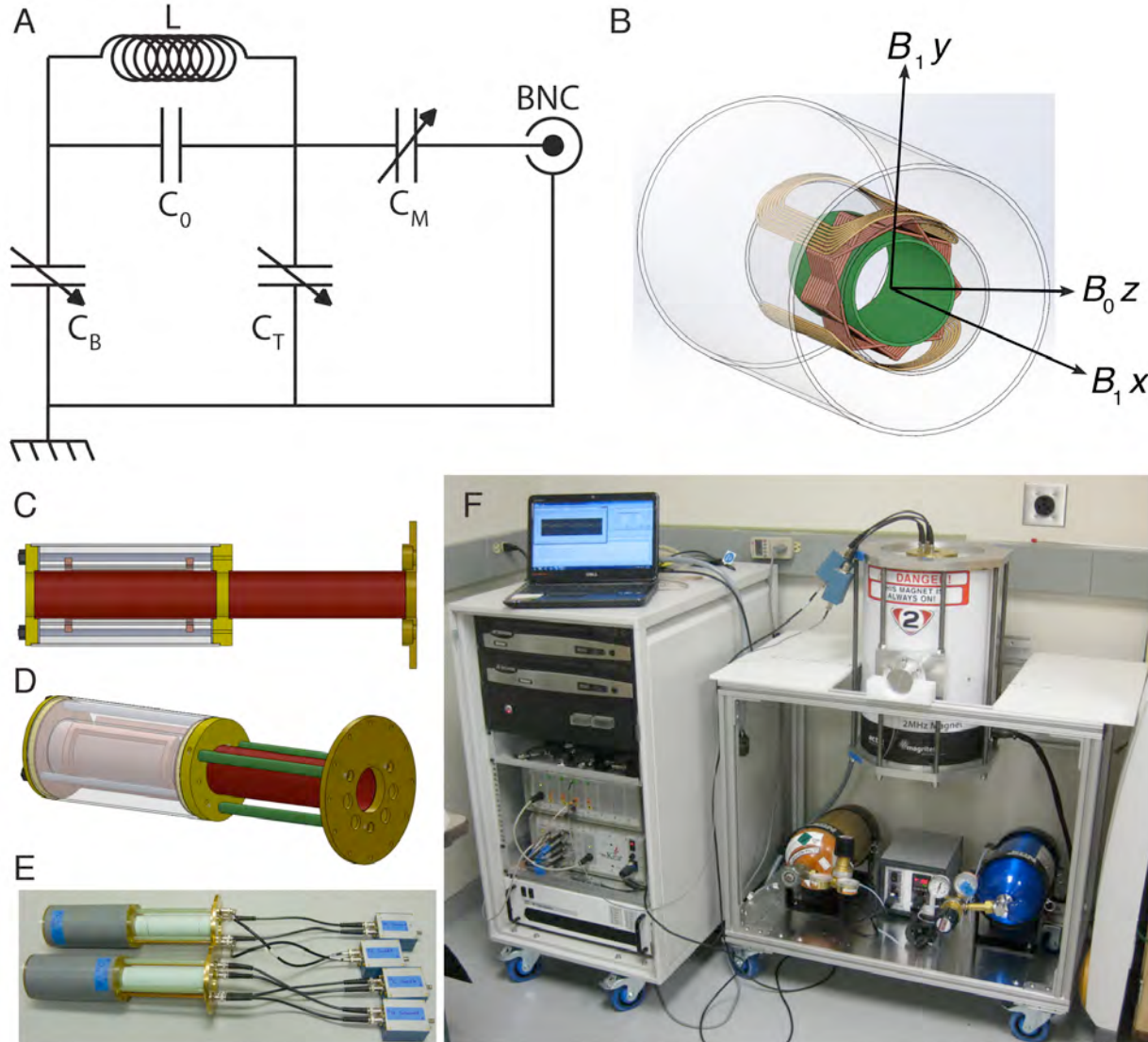


**Figure 10. The 0.0475 T MR scanner system.** A) The balanced tuning/matching circuit; B) Representation of the inner basket weave  $^1\text{H}/^{13}\text{C}$  detection coil, outer Helmholtz saddle coil for  $^{13}\text{C}/^1\text{H}$  excitation, and RF shield support tube; C) and D) views of the 0.0475 T probe design; E) realization of the H-X and X-H probes with attached tuning/matching boxes; F) View of overall MR scanner system in the vertical spectrometer configuration.

### Task 4.b. Low field MRI: pre-clinical optimization

The optimization was largely focused around optimization of detection RF coils. MRI acquisition parameters were also determined. Very high sensitivity RF coils were developed as well as the theory proving that low field detection of hyperpolarized contrast agents can be indeed more sensitive than that at high magnetic field (4). Fig. 11 summarizes the imaging work at low and high field. While 113% of high field SNR was theoretically possible, the limitations of our imaging system limited the actual RF coil performance to 40%. These are important lesson that will be taken into account when developing human scale MRI system.

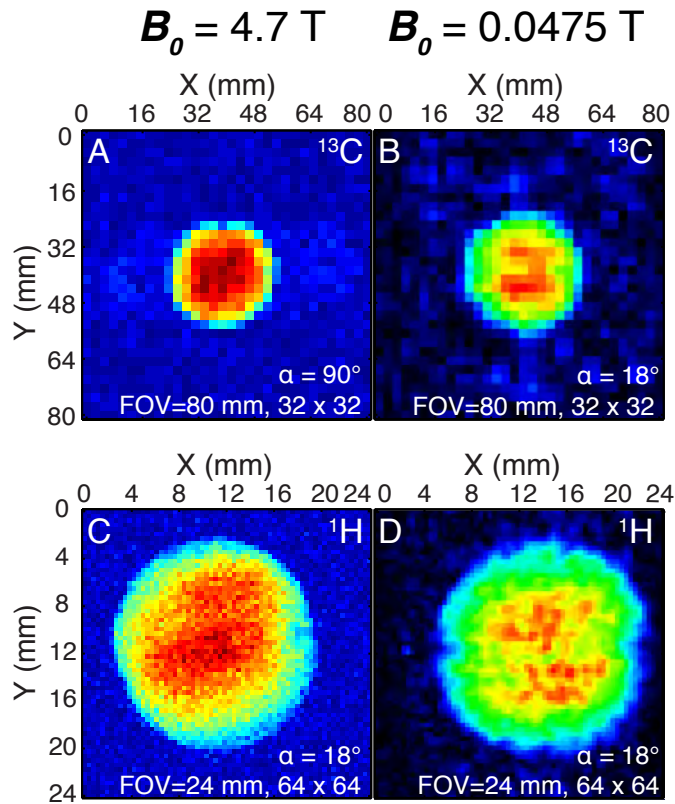


**Figure 11.  $^{13}\text{C}$  and  $^1\text{H}$  MRI of sodium  $1-^{13}\text{C}$ -acetate.** 4.7 T acquisition used Boltzmann  $^{13}\text{C} P = 4.06 \times 10^{-6}$  and  $^1\text{H} P = 1.61 \times 10^{-5}$ , and 0.0475 T used approximately the same polarization levels,  $^{13}\text{C} P = 4.70 \times 10^{-6}$  and  $^1\text{H} P = 1.05 \times 10^{-5}$ . All measurements used a spherical phantom: for  $^1\text{H}$  1.0 g sodium  $1-^{13}\text{C}$ -acetate in 99.8%  $\text{D}_2\text{O}$  with 2.8 mL total volume and for  $^{13}\text{C}$  5.18 g sodium  $1-^{13}\text{C}$ -acetate in 99.8%  $\text{D}_2\text{O}$  with 17.5 mL total volume. All acquisition and processing parameters were identical except  $^{13}\text{C}$  excitation pulse angle  $\alpha$ . No image extrapolation or zero filling was used.

We note the sub-millimeter resolution level achieved in proton scans of sodium  $1-^{13}\text{C}$ -acetate. For future imaging efforts in Year 2-3 in preclinical models of breast cancer, the following initial imaging parameters will be utilized.

Imaging sequence: 2D GRE without slice selection using direct  $^{13}\text{C}$  detection

TE/TR: 6.4 ms / 14 ms

Imaging matrix: 32 x 32

FOV: 80x80 mm<sup>2</sup>

Spatial Resolution: 2.5x2.5 mm<sup>2</sup>

Total Scan Speed: <0.5 s

Excitation pulse angle: 15 degrees for a single image acquisition to maximize SNR and 5 degree excitation RF pulse for dynamic acquisitions with ~2 s temporal resolution.

We will optimize the pulse sequence further once we have more preclinical experience and will extend the detection to indirect proton detection, full 3D acquisition and compressed sensing with the goals of optimizing concentration limits and spatial/temporal resolution.

We will use similar or identical acquisition parameters on pre-clinical 4.7 T system for quantitative comparison of imaging at low and high magnetic fields.

## Key Research Accomplishments

- Designed second-generation clinical scale xenon-129 polarizer
- Achieved nearly 100% theoretical maximum xenon-129 polarization in partially constructed polarizer demonstrating its future success and utility for future use as a part of xenon-induced polarization setup for polarization of <sup>13</sup>C metabolic contrast agents
- The *in situ* NMR quality assurance resonance frequency of developed xenon-129 polarizer was decreased to record low 47 kHz to minimize power requirements of xenon-129 polarizer and minimize its thermal management
- Developed novel dual channel low-field NMR RF coils for high detection sensitivity of hyperpolarized contrast agents in pre-clinical molecular imaging of breast cancer
- Achieved 40% detection sensitivity of MRI at 0.0475 T compared to that of 4.7 T pre-clinical MRI scanner for direct <sup>13</sup>C detection and indirect proton detection. More than 100% was theoretically possible, but not achieved due to hardware limitations
- Developed quantitative theory of MRI detection sensitivity of hyperpolarized contrast agents in low field from the perspective of RF coil design. This will pave the road to theoretical RF coil design for future clinical scale system
- Developed imaging protocols for 2D *in vivo* molecular preclinical imaging of breast cancer in mouse model using 0.0475 T MRI scanner with optimized RF coils

## Reportable Outcomes

### Oral Presentations

1. Chekmenev, E. Y., <sup>13</sup>C and <sup>15</sup>N PHIP and XIP polarized contrast agents for molecular imaging of cancer, COST Action TD1103 EuroHyperPol, Jun. 29, Dublin, Ireland, **2012**.
2. Chekmenev, E. Y., PHIP polarizing and imaging strategies for <sup>13</sup>C-lactate and <sup>15</sup>N-choline, The Third International Workshop, on Metabolic Imaging, Jul. 27, Philadelphia, PA, USA, **2012**.
3. Chekmenev, E. Y., What about Choline, IN VIVO MAGNETIC RESONANCE GORDON RESEARCH CONFERENCE, Aug. 3, Colby College, Waterville, ME, USA, **2012**.
4. Chekmenev, E. Y. Molecular Imaging of Breast Cancer using Hyperpolarized MRI Contrast Agents, Vanderbilt-Ingram Cancer Center, Breast Cancer Program & SPORE Seminar, Oct. 1, Vanderbilt University Medical Center, Nashville, TN, USA, **2012**.
5. Chekmenev, E. Y. Molecular Imaging of Breast Cancer using Hyperpolarized MRI Contrast Agents, Vanderbilt University Institute of Imaging Science Seminar, Jan. 11, Vanderbilt University Medical Center, Nashville, TN, USA, **2013**.

### Conference Abstracts

1. Chekmenev, E. Y. (Jul. 27, 2012). PHIP polarizing and imaging strategies for <sup>13</sup>C-lactate and <sup>15</sup>N-choline. The Third International Workshop on Metabolic Imaging, Philadelphia, PA, USA.
2. Coffey, A. M., M. Truong and E. Y. Chekmenev (April 14-19, 2013). Improving imaging sensitivity of hyperpolarized MR at low magnetic detection field strengths. Experimental NMR Conference, Asilomar, California.
3. Nikolaou, P. and E. Y. Chekmenev (2012). An 'Open-Source' <sup>129</sup>Xe Polarizer for Clinical Imaging and Secondary Hyperpolarization of <sup>13</sup>C Tracers for Molecular Imaging of Cancer Vanderbilt University Imaging Institute Annual Retreat.
4. Nikolaou, P., A. Coffey, L. L. Walkup, B. Gust, H. Newton, I. Muradyan, M. Rosen, S. Patz, M. J. Barlow, B. M. Goodson and E. Y. Chekmenev (April 14-19, 2013). "XeUS";—A Second-Generation 'Open Source' Clinical-Scale <sup>129</sup>Xe Polarizer for Xenon-Induced Polarization. Experimental NMR Conference, Asilomar, California.
5. Nikolaou, P., A. Coffey, L. L. Walkup, B. Gust, N. Whiting, H. Newton, S. Barcus, I. Muradyan, M. Dabaghyan, G. D. Moroz, M. Rosen, S. Patz, M. J. Barlow, E. Y. Chekmenev and B. M. Goodson (April 14-19, 2013). High (~30-90%) <sup>129</sup>Xe Hyperpolarization at High Xe Densities Using an 'Open-Source' Polarizer for Clinical and Materials MRS/MRI. Experimental NMR Conference, Asilomar, California.

## **Manuscripts**

1. R. V. Shchepin, W. Pham, E. Y. Chekmenev, Towards Hyperpolarized Phospholactate Imaging: Dephosphorylation and Biodistribution of 1-13C-phospholactate In Vivo. *Contrast Media Mol. Imaging*, submitted (2013).
2. R. G. Abramson, L. R. Arlinghaus, J. Weis, i. X. L, A. N. Dula, E. Y. Chekmenev, S. Smith, M. I. Miga, V. Abramson, T. E. Yankelev, Current and emerging quantitative magnetic resonance imaging methods for assessing and predicting the response of breast cancer to neoadjuvant therapy. *Breast Cancer Targets and Therapy* **4**, 139 (2012).
3. P. Nikolaou, A. Coffey, L. L. Walkup, B. Gust, N. Whiting, H. Newton, S. Barcus, I. Muradyan, M. Dabaghyan, G. D. Moroz, M. Rosen, S. Patz, M. J. Barlow, E. Y. Chekmenev, B. M. Goodson, Near-unity nuclear polarization with an ‘open-source’ 129Xe hyperpolarizer for NMR and MRI. *Proc. Natl. Acad. Sci. U. S. A.*, conditionally accepted (2013).

## **Funding applied for based on work supported by this award**

1. *3D Printer for Biomedical Research and Engineering*, submitted to DoD FY2013 DEFENSE UNIVERSITY RESEARCH INSTRUMENTATION PROGRAM (DURIP), Department of Army, PI: Chekmenev, Requested amount: \$297,586.00, Date submitted: 2012-09-27.
2. *MRI Consortium: Portable Large Scale Low Field Xenon-129 Polarizer/Sub-Second MRI Scanner*, submitted to NSF MRI program, PIs: Chekmenev (Vanderbilt), Goodson (Southern Illinois University), Requested amount: \$ 840,200, Date submitted: 2013-02.

## **Conclusion**

Second-generation xenon-129 polarizer was designed, and it now undergoes the construction according to the DoD approved schedule. The second-generation polarizer includes several key engineering innovations. When combined, they resulted in more efficient polarizer operation. For example, the polarizer is a stand-alone device that does not require any every day consumables besides electric power. So far this has not been achieved with any clinical scale xenon-129 polarizer, so it definitely represents an engineering breakthrough, which can be utilized in biomedicine in the future. Relevant to our consortium on xenon-129 polarizers’ development this paves the road to the next generation devices that will be completely automated and can be potentially operated as push-button devices from the perspective of contrast agent production of hyperpolarized xenon-129. Scientifically, we have achieved very high level of xenon-129 polarization, which we currently attribute to more careful design and cell temperature management. Future work on optimization will provide better understanding during QA process in Year 2 of the project. High xenon-129 polarization is critical for xenon-induced polarization, because xenon-129 will serve as a source of nuclear spin polarization and approaching theoretical maximum with xenon-129 would potentially allows approaching theoretical maximum with <sup>13</sup>C hyperpolarized contrast agents.

We have demonstrated that low-field imaging of hyperpolarized contrast agent can be as sensitive as the high-field detection and potentially more sensitive (but would require cryogenic RF coils – these are outside the scope of the project and our current expertise) than high field detection. We have also demonstrated this concept with 40% detection sensitivity, which is in a good agreement due to known hardware limitations: magnet bore, non-ideal wire selection, etc.

The strategy of testing and optimizing RF coil sensitivity of low field at preclinical stage paid off, because we were able to developed a quantitative theory for SNR of hyperpolarized contrast agent in low field. The lessons learned about geometry and components interactions will be useful during clinical research system design and construction and will undoubtedly allow us to achieve optimal performance. This is essential as the development of clinical system in Years 3-5 is one of the ultimate goals of the project.

No changes for future work are requested.

## **References**

1. P. Nikolaou, A. Coffey, L. L. Walkup, B. Gust, N. Whiting, H. Newton, S. Barcus, I. Muradyan, M. Dabaghyan, G. D. Moroz, M. Rosen, S. Patz, M. J. Barlow, E. Y. Chekmenev, B. M. Goodson, Near-unity nuclear polarization with an ‘open-source’ 129Xe hyperpolarizer for NMR and MRI. *Proc. Natl. Acad. Sci. U. S. A.*, conditionally accepted (2013).

2. P. Nikolaou, A. Coffey, L. L. Walkup, B. Gust, N. Whiting, H. Newton, S. Barcus, I. Muradyan, M. Dabaghyan, G. D. Moroz, M. Rosen, S. Patz, M. J. Barlow, E. Y. Chekmenev, B. M. Goodson, in *Experimental NMR Conference*. (Asilomar, California, 2013), pp. April 14-19.
3. P. Nikolaou, A. Coffey, L. L. Walkup, B. Gust, H. Newton, I. Muradyan, M. Rosen, S. Patz, M. J. Barlow, B. M. Goodson, E. Y. Chekmenev, in *Experimental NMR Conference*. (Asilomar, California, 2013), pp. April 14-19.
4. A. M. Coffey, M. Truong, E. Y. Chekmenev, in *Experimental NMR Conference*. (Asilomar, California, 2013), pp. April 14-19.
5. E. Y. Chekmenev, in *The Third International Workshop on Metabolic Imaging*. (Philadelphia, PA, USA, 2012), pp. Jul. 27.
6. P. Nikolaou, E. Y. Chekmenev, in *Vanderbilt University Imaging Institute Annual Retreat*. (2012), pp. Summer 2012.
7. R. G. Abramson, L. R. Arlinghaus, J. Weis, i. X. L, A. N. Dula, E. Y. Chekmenev, S. Smith, M. I. Miga, V. Abramson, T. E. Yankeelov, Current and emerging quantitative magnetic resonance imaging methods for assessing and predicting the response of breast cancer to neoadjuvant therapy. *Breast Cancer Targets and Therapy* **4**, 139 (2012).

## Appendices

### Appendix 1: Statement of work, Year 1.

Milestones	Year 1 quarters			
	1	2	3	4
1.a. Open Source $^{129}\text{Xe}$ Polarizer: design	x	x	x	
1.b. Open Source $^{129}\text{Xe}$ Polarizer: construction				x
4.a. Low field MRI: pre-clinical development	x	x		
4.b. Low field MRI: pre-clinical optimization			x	x

This statement of work is divided in four different sections matching four Specific Aims of the proposal. Relevant to the Year 1 are the following:

#### 3) Preparation of pure hyperpolarized contrast agents approved for injection in humans

**1.a.** Y1Q1-Y1Q3. Design of open-source 2<sup>nd</sup> generation  $^{129}\text{Xe}$  polarizer. The design will take advantage of the design and development process of the 1<sup>st</sup> generation XENA device. More details are provided in the description of the sub-contract to Southern Illinois University.

**1.b.** Y1Q4-Y2Q2. Construction of the open-source 2<sup>nd</sup> generation  $^{129}\text{Xe}$  polarizer. The construction will require low field spectrometer and high power narrowed tunable laser requested in the original budget.

#### 4) Development of low field (low cost) sub-second *in vivo* imaging suitable for preclinical models of breast cancer and clinical trials

**4.a.** Y1Q1-Y1Q2. Low field MRI: pre-clinical development will be done based on our existing hardware that was developed during our preliminary work. The work will focus on developing and construction of multiple RF coils intended for optimal direct and indirect detection of hyperpolarized contrast agents *in vivo*. Additional time will be spent on implementation of ultra-fast MRI sequences.

**4.b.** Y1Q3-Y1Q4. Low field MRI: pre-clinical optimization will be conducted to optimize developed hardware and MRI sequences for specific metabolic contrast agents and their metabolites *in vivo*.

**Appendix 2: Performance Evaluation for QPC Laser ES-6507-Z002, SN 1209201**

**Performance Evaluation for QPC Laser ES-6507-Z002, SN 1209201  
(supplement to QPC Product Test Report)**

**Laura Walkup, Brogan Gust, Boyd Goodson**

*Department of Chemistry and Biochemistry, Southern Illinois University, Carbondale, IL 62901*

**Internal Document For: Hyperpolarized Xenon Technology Consortium (HXTC) &  
QPC Lasers**

**9 November 2012**

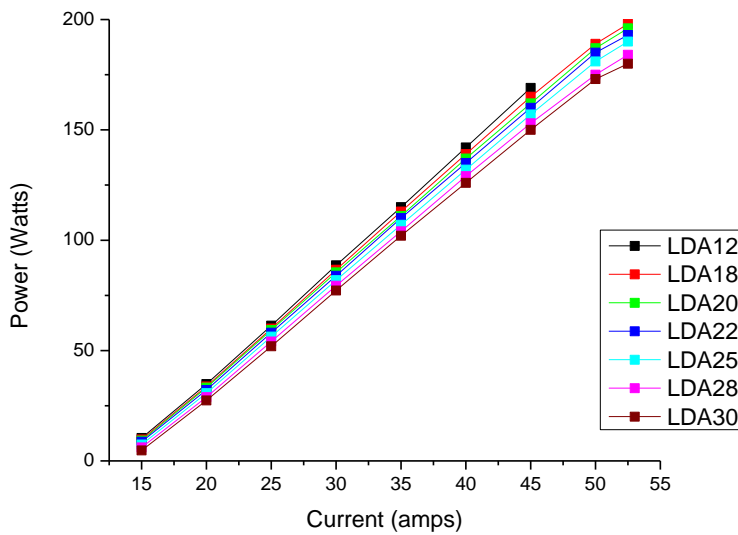
**Version 1.0**

**(Note: This document will be amended once the twin TEC-cooled side-arms and retro-reflection become operational, and once  
1" optics have been tested)**

<b>Reference Information:</b>	
<b>Nominal Current</b>	<b>52.5 A</b>
<b>Nominal Max Current (Overdrive)</b>	<b>55 A</b>
<b>Nominal Max Diode Temperature</b>	<b>35 °C</b>

## Performance without optical train—

Current versus power for various LDA temperatures:



Water chiller temperatures (°C) to achieve desired LDA temp at various currents:

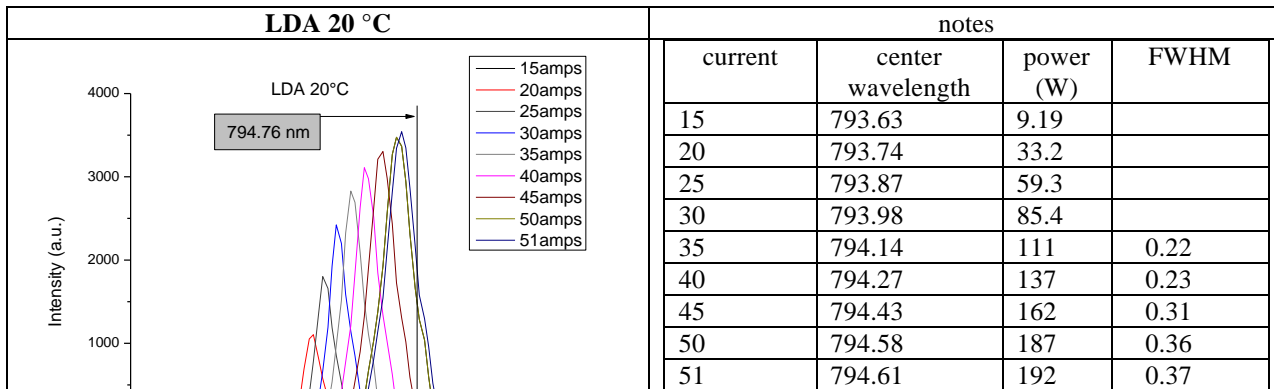
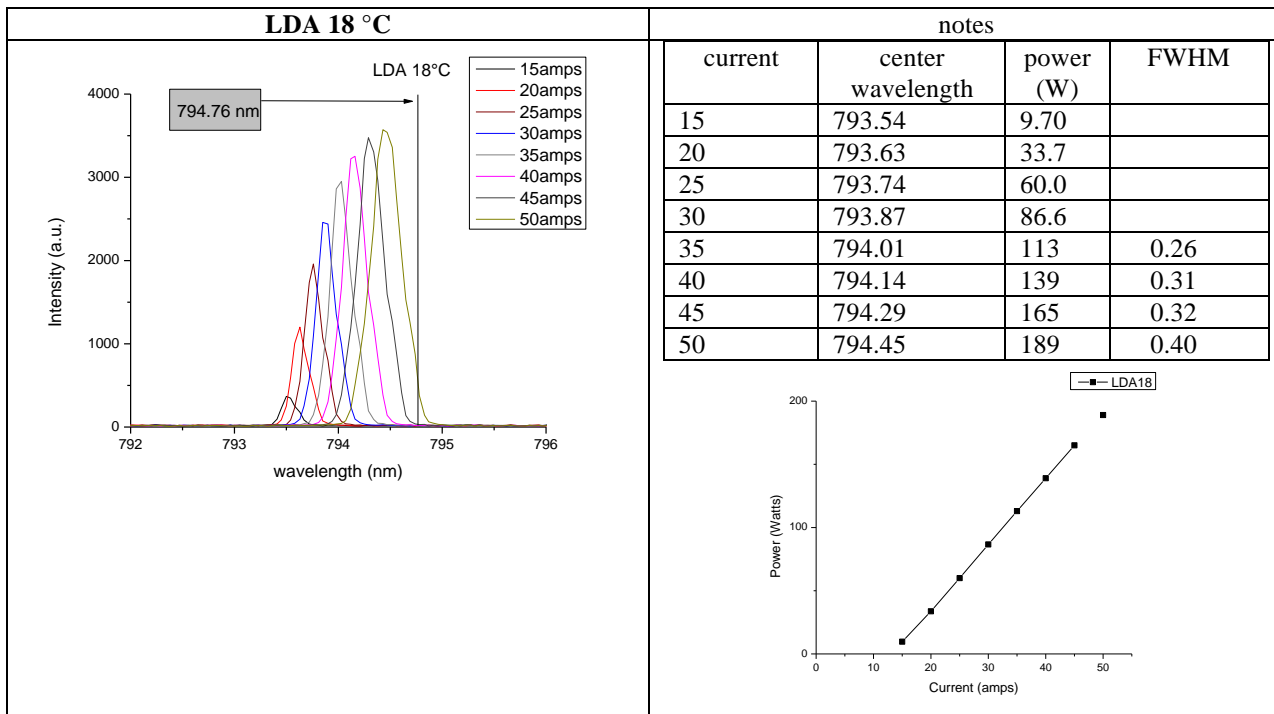
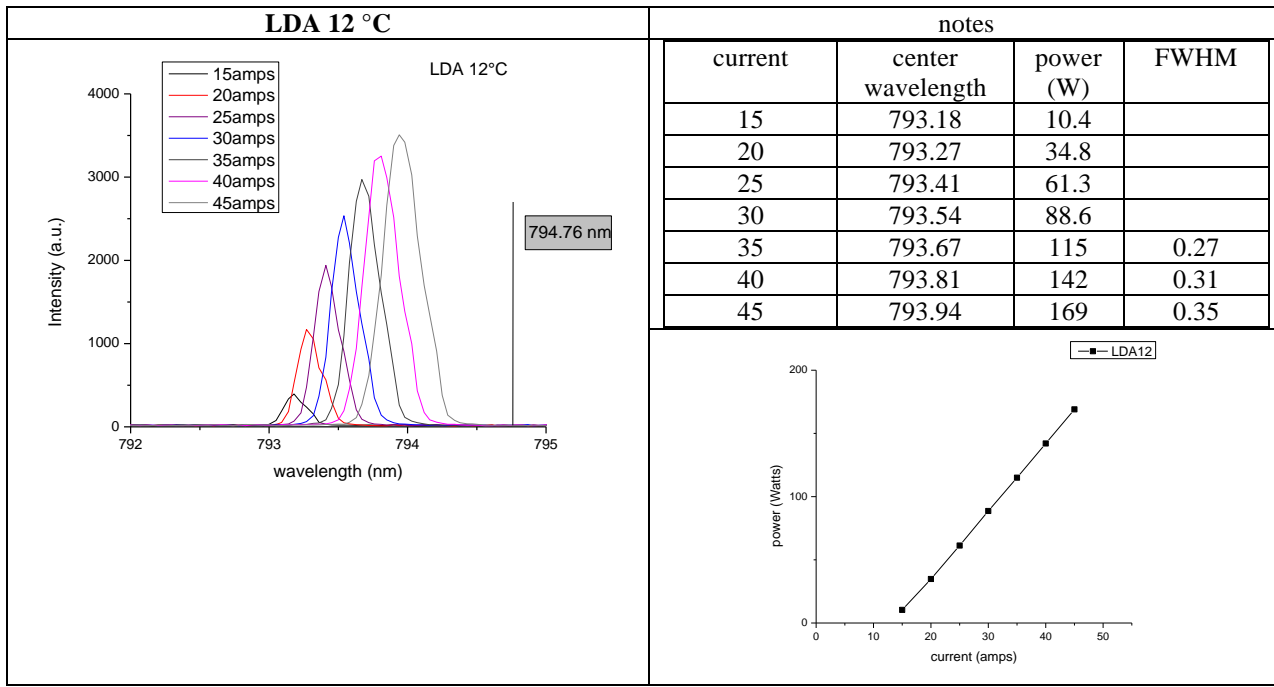
LDA (°C)	15amps	20amps	25amps	30amps	35amps	40amps	45amps	50amps	52.5amps
<b>12</b>	11.0	10.2	9.0	8.2	7.8	6.2	5.2	na*	na*
<b>18</b>	17.0	15.8	15.0	14.0	13.0	12.0	11.0	10.0	9.3
<b>20</b>	18.5	17.8	16.8	16.0	15.0	14.0	13.0	12.0	11.5
<b>22</b>	20.5	19.6	18.6	18.0	17.0	16.0	15.0	14.0	13.5
<b>25</b>	23.0	22.5	21.5	20.5	19.5	18.5	17.5	16.5	17.1
<b>28</b>	26.0	25.0	24.0	23.5	22.2	21.2	20.4	19.6	18.9
<b>30</b>	28.0	27.0	26.0	25.0	24.0	23.3	22.3	21.3	20.8

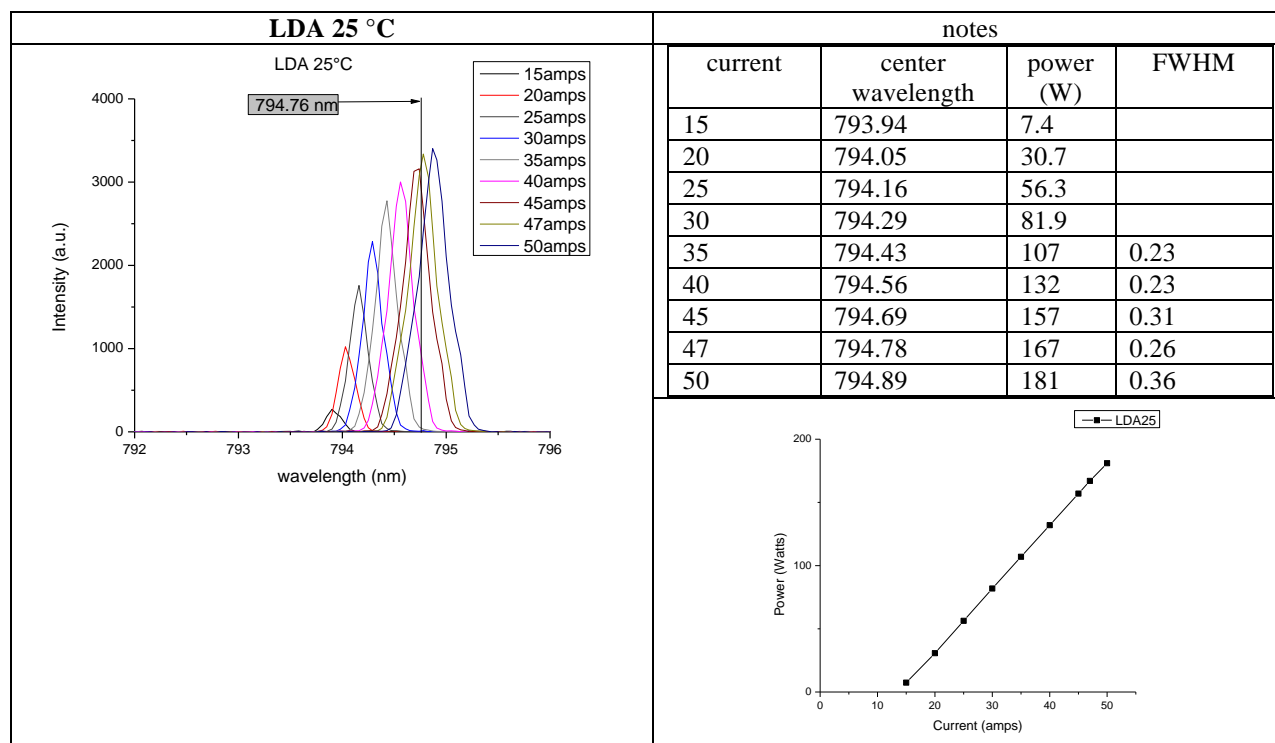
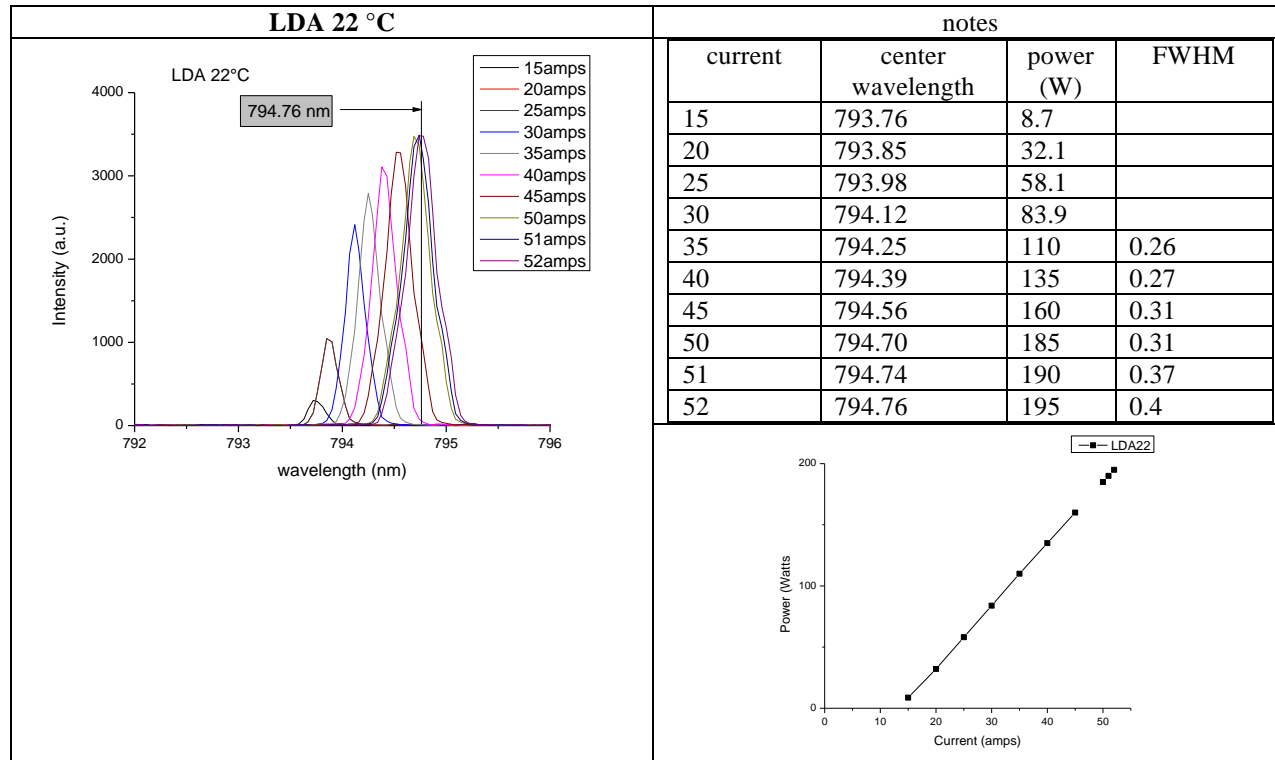
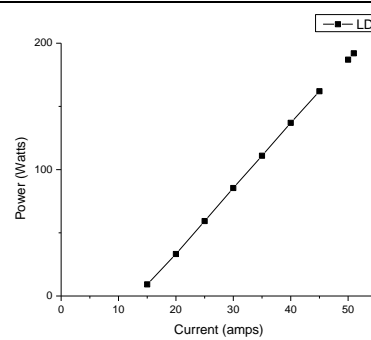
\*- lowest setting on water chiller is 5°C

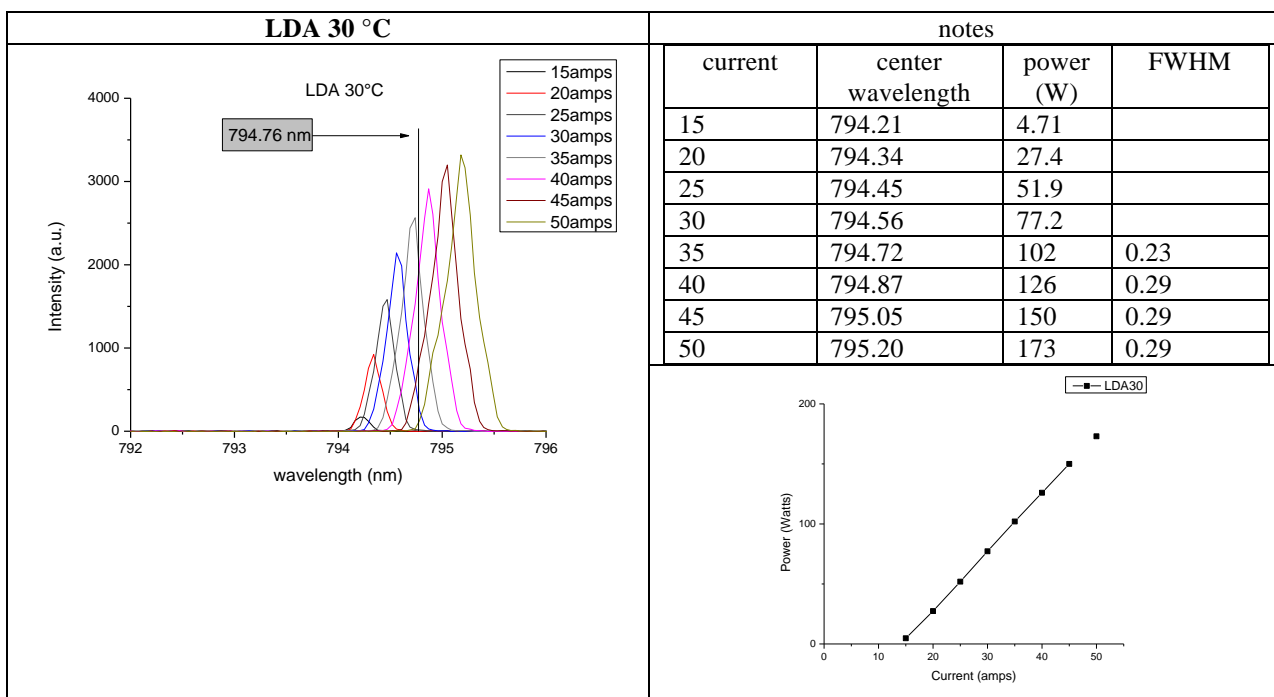
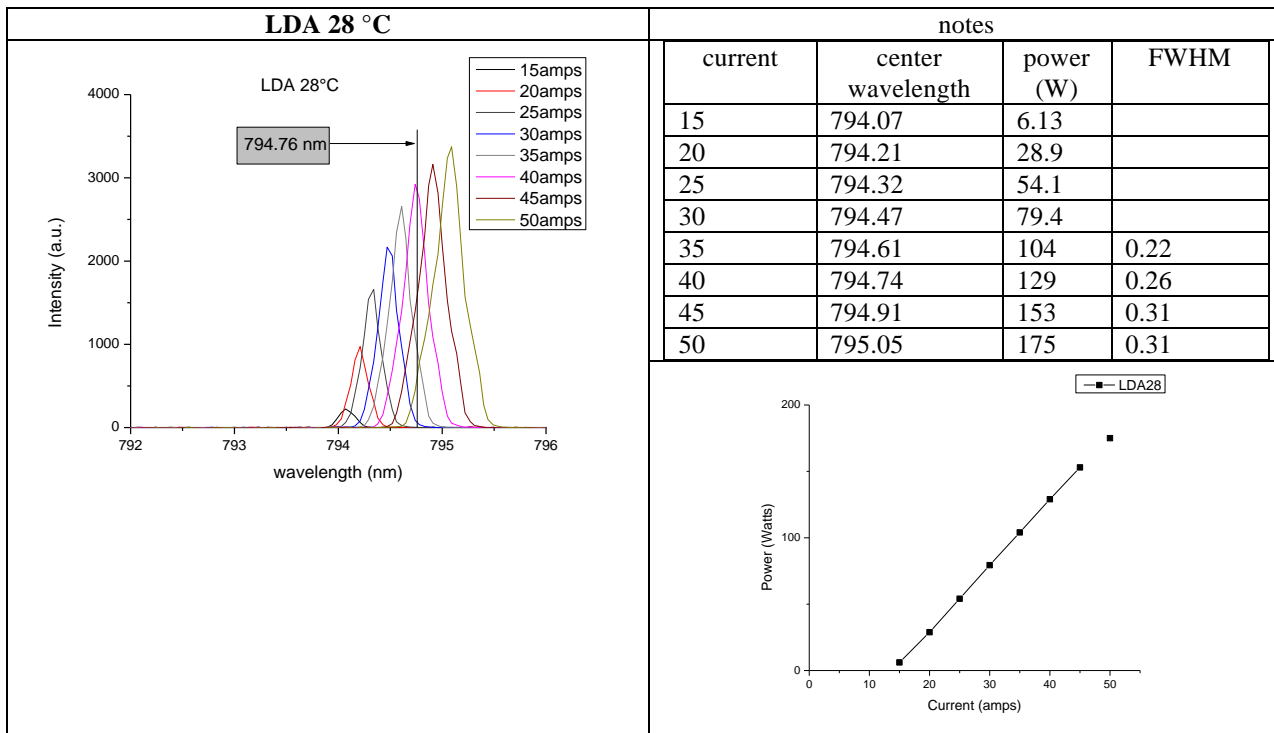
Output center wavelength, as a function of LDA temp and current:

LDA (°C)	15amps	20amps	25amps	30amps	35amps	40amps	45amps	50amps	52.5amps
<b>12</b>	793.18	793.27	793.41	793.54	793.67	793.81	793.94	na	na
<b>18</b>	793.54	793.63	793.74	793.87	794.01	794.14	794.29	794.45	794.53
<b>20</b>	793.63	793.74	793.87	793.98	794.14	794.27	794.43	794.58	794.61
<b>22</b>	793.76	793.83	793.98	793.12	794.25	794.39	794.56	794.70	794.74
<b>25</b>	793.94	794.05	794.16	794.29	794.43	794.56	794.69	794.89	794.91
<b>28</b>	794.07	794.21	794.32	794.47	794.61	794.74	794.91	795.05	795.00
<b>30</b>	794.21	794.34	794.45	794.56	794.72	794.87	795.05	795.20	795.27

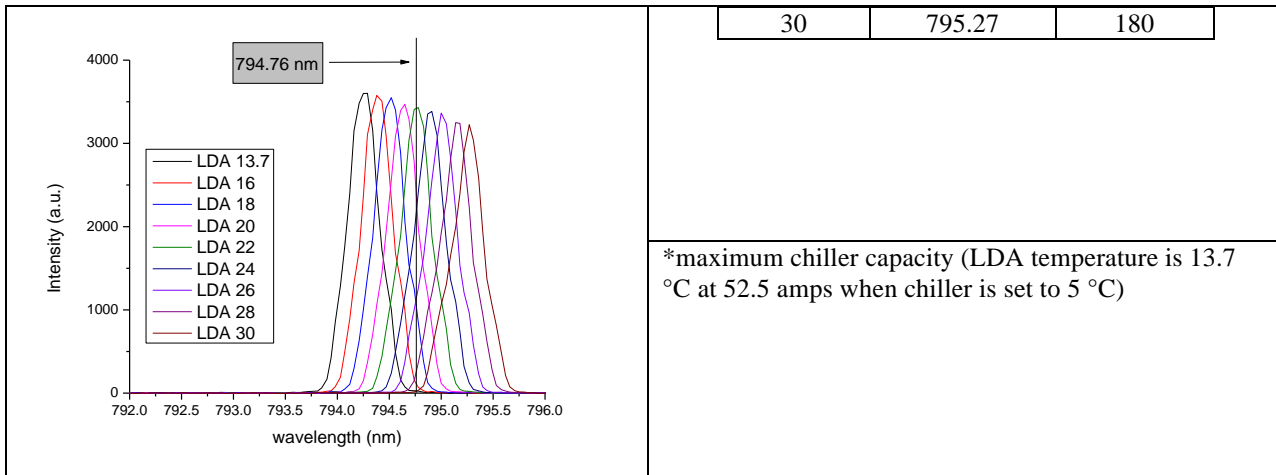
[Nominal resonance: 794.767 nm]



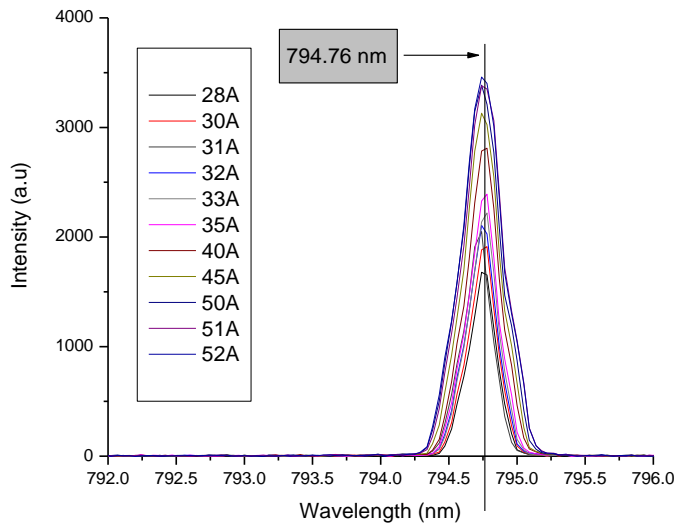




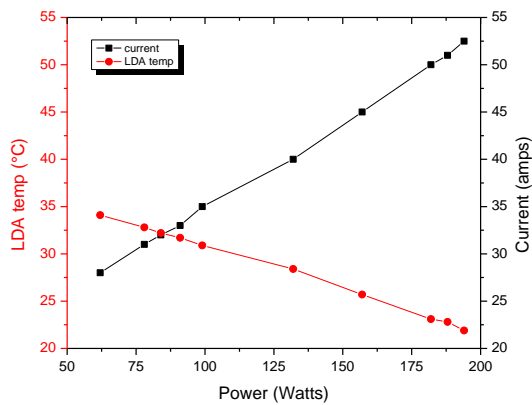
52.5 amps (nominal current)		notes			
		LDA	center wavelength	power	
		13.7*	794.26	202	
		16	794.40	200	
		18	794.53	198	
		20	794.65	196	
		22	794.76	193	
		24	794.91	190	
		26	795.00	187	
		28	795.16	184	



**"Resonance"**



LDA	current	power	center $\lambda$	FWHM
21.9	52.5	194	794.74	0.35
22.8	51	188	794.74	0.33
23.1	50	182	794.74	0.31
25.7	45	157	794.74	0.29
28.4	40	132	794.78	0.28
30.9	35	99	794.78	0.26
31.7	33	91	794.78	0.24
32.2	32	84	794.74	0.23
32.8	31	78	794.74	0.25
33.1	30	68	794.78	0.26
34.1	28	62	794.74	0.20



To mimic QPC specs but **without** optical train mounted (QPC specs *include* optical train)

Water chiller set at 13°C

Power measured directly out of laser fibre (no optical train)

LDA temp (°C)	Current (amps)	Voltage (volts)	Power (Watts)
14.1	15	13.34	10.2
15.0	20	13.51	34.4
15.9	25	13.66	60.8
17.0	30	13.80	87.2
18.1	35	13.93	113
19.1	40	14.06	133
20.3	45	14.17	162
21.2	50	14.29	186

To reproduce QPC specs **with** 2" optical train mounted, water chiller set to 13°C

Power measured at "front" position of optical cell (~9.85" from end of optical train)

LDA temp (°C)	current (amps)	voltage (volts)	QPC spec power (W)	front power (W)	dump power (W)	power sum (Watts)	split front/dump
14.1	15	13.34	9.5	9.48	0.20	9.68	98/2
15.0	20	13.50	32.0	32.0	0.83	32.83	97/3
16.0	25	13.65	57.0	56.2	1.58	57.78	97/3
17.1	30	13.79	80.8	81	2.34	83.34	97/3
18.1	35	13.93	106.2	105	3.14	108.14	97/3
19.1	40	14.05	129.2	128	4.06	132.06	97/3
20.1	45	14.17	151.2	150	5.09	155.09	97/3
21.2	50	14.29	172.0	171	6.00	177	97/3
21.7	52.5	14.34	180	181	6.42	187.42	97/3

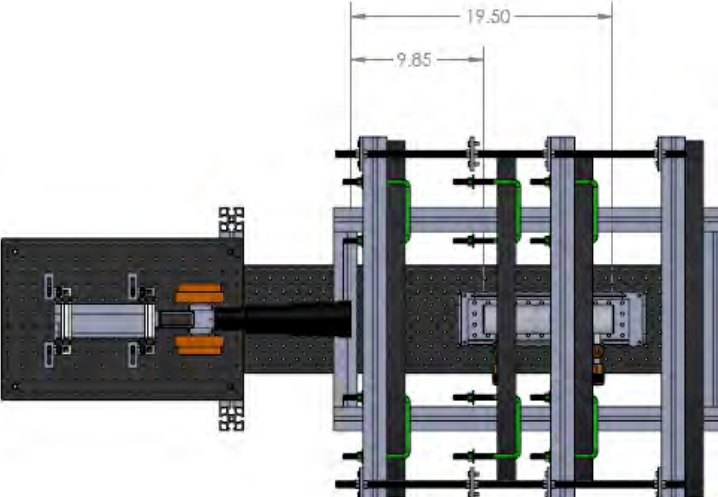
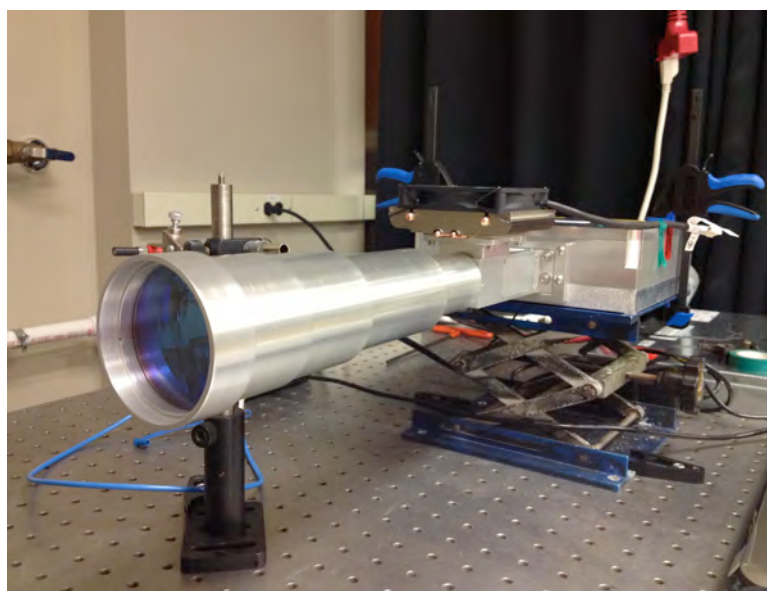
Power with and without optical train mounted (to approximate power loss to optics)

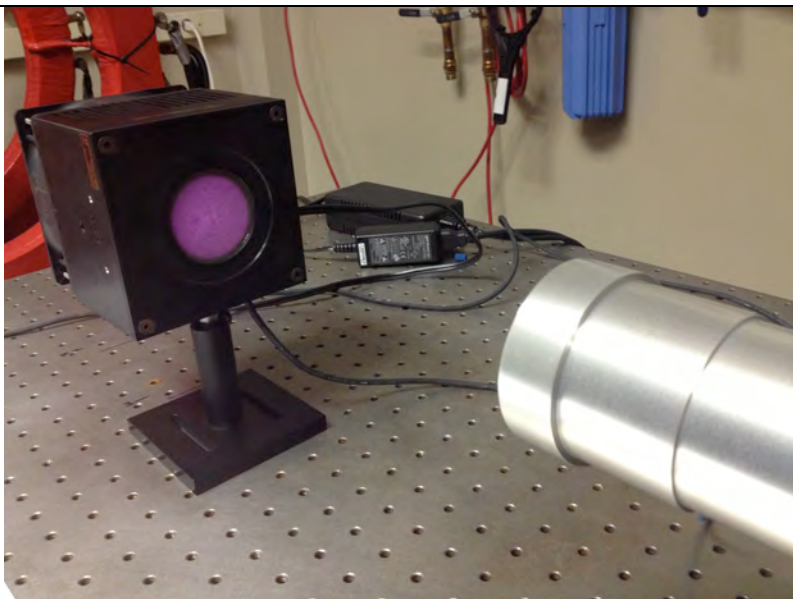
	W/O OT	W/ OT				
current (amps)	Power (Watts)	front power (W)	dump power (W)	power sum (Watts)	Difference	%-age power lost
15	<b>10.2</b>	9.48	0.20	<b>9.68</b>	0.52	5.1
20	<b>34.4</b>	32.0	0.83	<b>32.83</b>	1.57	4.6
25	<b>60.8</b>	56.2	1.58	<b>57.78</b>	3.02	5.0
30	<b>87.2</b>	81	2.34	<b>83.34</b>	3.86	4.4
35	<b>113</b>	105	3.14	<b>108.14</b>	4.86	4.3
40	<b>133</b>	128	4.06	<b>132.06</b>	0.94	0.7
45	<b>162</b>	150	5.09	<b>155.09</b>	6.91	4.3
50	<b>186</b>	171	6.00	<b>177</b>	9	4.8
52.5	<b>194</b>	181	6.42	<b>187.42</b>	6.58	3.4

Total effective efficiency

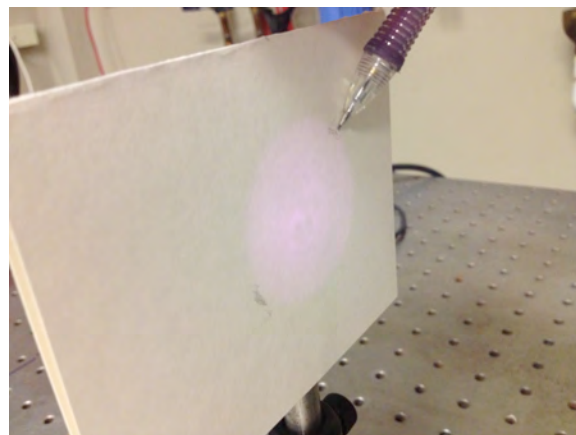
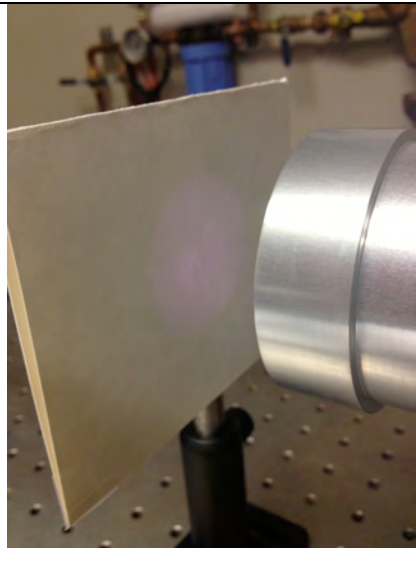
	<b>W/O OT</b>	<b>W/ OT</b>			
<b>current (amps)</b>	<b>Power (Watts)</b>	<b>front power (W)</b>	<b>dump power (W)</b>	<b>power sum (Watts)</b>	<b>Total effective efficiency (%-age)</b>
15	<b>10.2</b>	<b>9.48</b>	0.20	9.68	92.9
20	<b>34.4</b>	<b>32.0</b>	0.83	32.83	93.0
25	<b>60.8</b>	<b>56.2</b>	1.58	57.78	92.4
30	<b>87.2</b>	<b>81</b>	2.34	83.34	92.9
35	<b>113</b>	<b>105</b>	3.14	108.14	92.9
40	<b>133</b>	<b>128</b>	4.06	132.06	96.2
45	<b>162</b>	<b>150</b>	5.09	155.09	92.6
50	<b>186</b>	<b>171</b>	6.00	177	91.9
52.5	<b>194</b>	<b>181</b>	6.42	187.42	93.3

**Beam diameter through optical train:**

	<p>From XeUS schematics, distances from end of optical train to the OP cell:</p> <p>to cell front: 9.85" to cell middle: 14.68" to cell back: 19.5"</p>
	<p>Optical train mounted to laser module in the horizontal orientation.</p> <p>Beam dumping in this orientation:</p> <p>Retroreflection ↑ Dump beam ↓</p> <p>At 52.5 amps (highest operating current), dump beam measured as 6.42 W.</p> <p>One included heat sink was mounted for retroreflection; a second heat sink has been ordered.</p>
<a href="http://www.youtube.com/watch?v=gIE-SP1Rams">http://www.youtube.com/watch?v=gIE-SP1Rams</a>	<p>Beam collimation test through 2" optical train on YouTube</p> <p>LDA 16°C, 56W forward, ~1.5W dump beam</p>

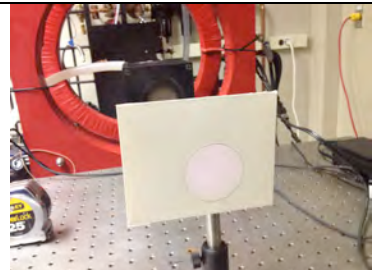


2" beam at approximate front of optical cell region

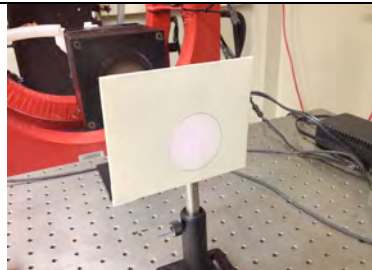


Measuring beam diameter: ~2W output (13 amps, WC 16°C, LDA 16.9°C) beam marked with pencil and measured.

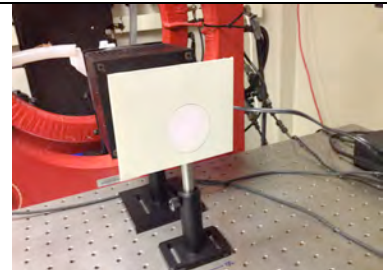
Card marked with 2" diameter circle:



front of cell



middle of cell



back of cell

## Conclusions

- Laser exhibits excellent lineshape lock quality over nearly the entire range of operating conditions.
- Beam quality and collimation through optical train are excellent throughout relevant operating condition range.
- All required specs (in terms of FWHM, centroid wavelength tuning range, output power, operating temperature range, and efficiency of optics train) are met.
- Heating of optical train is not significant-- even during periods of prolonged operation.
- Not yet tested: CP fidelity of output; operation under retroreflection; operation of heatsinks for cooling under retroreflection; 1" optics; long-term stability of output characteristics.

## Appendix 3: Abstracts Presented

### Abstract of Oral Presentation #2, reference # (5)

#### PHIP polarizing and imaging strategies for $^{13}\text{C}$ -lactate and $^{15}\text{N}$ -choline

Eduard Y. Chekmenev<sup>1,2,3,4,5</sup>, Kevin W. Waddell<sup>1,2</sup>, Roman V. Shchepin<sup>1,2</sup>, Aaron Coffey<sup>1,3</sup>

<sup>1</sup>Institute of Imaging Science, and Departments of <sup>2</sup>Radiology and Radiological Sciences, <sup>3</sup>Biomedical Engineering, <sup>4</sup>Biochemistry, <sup>5</sup>Vanderbilt-Ingram Cancer Center, Vanderbilt University, Nashville, TN 37232 United States

**Introduction:** One of the main bottlenecks for preclinical and clinical application of hyperpolarized MR is the development and validation of relevant contrast agents that can probe biochemical pathways *in vivo*. Dynamic nuclear polarization (DNP)<sup>1</sup> has been most widely used to date with the main drawback of long (~1 h) polarization cycles. Parahydrogen induced polarization (PHIP) offers significantly faster preparations with hyperpolarization cycles as short as 1 minute. However, it is limited by the availability of the required unsaturated molecular precursors that are necessary for molecular addition of parahydrogen<sup>2,3</sup>, which acts as a source of spin order. An additional requirement for increased relaxation time of the hyperpolarized  $^{13}\text{C}$  or  $^{15}\text{N}$  site is the absence of directly attached protons. As a result, the smallest PHIP moiety consists of an unsaturated C=C or C=C bond adjacent to a labeled  $^{13}\text{C}$  or  $^{15}\text{N}$  site. For  $^{13}\text{C}$  hyperpolarized compounds, this represents a three carbon limitation successfully exemplified by acrylate moiety by a number of groups.<sup>4,5</sup> In contrast, a leading DNP hyperpolarized metabolic agent  $1\text{-}^{13}\text{C}$ -pyruvate is also a three-carbon molecule carrying an extra oxygen atom in addition to the three-carbon skeleton of propionate. Hyperpolarized  $1\text{-}^{13}\text{C}$ -pyruvate is not amenable by PHIP. Here we present a strategy of using –OH phosphate protected precursor for preparation of PHIP hyperpolarized contrast agents. Nuclear spin polarization of hyperpolarized contrast agents is independent of the applied magnetic field when detected *in vivo*. As a result, low field MR detection of hyperpolarized contrast agents *in vivo* can potentially be as sensitive as the one at high field<sup>6</sup> as long as the sensitivity of detection RF coil is compensated with increased number of turns. We recently described 0.0475 T dual channel RF coil capable of sensitive *in situ* detection  $^{13}\text{C}$  detection<sup>7</sup> of PHIP hyperpolarized contrast agents.<sup>8</sup> First imaging results will be presented using this method adapted for preclinical molecular imaging of cancer in mice.

**Methods:** We used PHIP polarizer with *in situ* detection capability previously described<sup>8</sup> with the exception that we utilized a new dual channel RF coil optimized for  $^{13}\text{C}$  PHIP detection. 97% parahydrogen was produced using in-house built parahydrogen generator.<sup>9</sup> Catalyst and PHIP precursor preparations were done according to previously described protocols.  $1\text{-}^{13}\text{C}$ -phosphoenolpyruvate (Isotec) was used as PHIP precursor for hyperpolarization of  $1\text{-}^{13}\text{C}$ -phospholactate, Fig. 1.

**Results:** PHIP polarization P ~ 1% was achieved with  $1\text{-}^{13}\text{C}$ -phospholactate, Fig. 1.  $^{13}\text{C}$   $T_1$  of 36 s was measured *in situ* at 0.0475 T,<sup>10</sup> which is suitable for *in vivo* application, Fig. 1.

The NMR probe head for  $^1\text{H}$  and X nucleus (X =  $^{13}\text{C}$  or  $^{15}\text{N}$ ) was constructed for operation at a static field of  $B_0 = 0.0475$  T. The RF coil, Fig. 2a, consists of two single channel circuits sharing a ground with capacitors for achieving suitable tuning range and impedance matching for each channel. The NMR probe frequencies of interest are 2.02 MHz ( $^1\text{H}$ ), 0.508 MHz ( $^{13}\text{C}$ ), and 0.205 MHz ( $^{15}\text{N}$ ) at the Halbach array's 0.0475 T  $B_0$  field strength. The  $^1\text{H}$  circuit consists of an outer 16 turn (8 turns each side) 70 mm x 130 mm (I.D. x length) Helmholtz saddle coil. The second X channel coil is a 206 turn 50 mm x 170 mm (I.D. x length) single layer solenoid closely fitted to the high-pressure reactor used for molecular addition of parahydrogen to unsaturated molecular precursors. HEP (2-hydroxyethyl propionate-1- $^{13}\text{C}$ ,2,3,3-d3) was polarized with PASADENA<sup>3</sup> by catalytic hydrogenation from HEA (2-hydroxyethyl acrylate-1- $^{13}\text{C}$ ,2,3,3-d3) using up to 97 % enriched parahydrogen. Fig. 2b shows *in situ*  $^{13}\text{C}$  detection of 15 micromoles (< 2 mg) of HEP with 20% polarization, or signal and polarization enhancement  $\epsilon \sim 5,000,000$ , with a  $^{13}\text{C}$  SNR ~ 2, 300 and FWHM = 26 Hz. Furthermore, the  $^{13}\text{C}$  MR sensitivity of the presented 0.0475 T RF probe was compared to that of a commercial 4.7 T small-animal RF coil with smaller volume. We used a sample of sodium  $1\text{-}^{13}\text{C}$ -acetate (1 g in 2.8 mL  $\text{D}_2\text{O}$  solution) polarized to  $P \sim 4 \times 10^{-6}$  for single scan  $^{13}\text{C}$  acquisition, Fig. 2 using spectra width of 10 kHz. The high field (4.7 T) volume coil yielded an SNR of 120 with a FWHM of 6 Hz, while the  $^{13}\text{C}$  solenoid coil of the 0.0475 T H-X probe achieved an SNR of 28 with a FWHM of 25 Hz.

**Discussion:** The method of -OH phosphate protected and stabilized C=C bond offers an opportunity to polarize metabolic contrast agents not amenable in the past. Presented here is the preliminary result of PHIP hyperpolarization of  $1\text{-}^{13}\text{C}$ -phospholactate. PHIP hydrogenation is efficient and blood phosphatases cleave phosphate moiety after tracer injection in living organism (data not shown) producing metabolically relevant ( $1\text{-}^{13}\text{C}$ -lactate) contrast agent. The method can be potentially extended to protected  $^{15}\text{N}$ -cholines.<sup>11</sup>  $^{13}\text{C}$  hyperpolarized lactate is a potent metabolic imaging contrast agent.<sup>12</sup>

**Conclusion:** MR sensitivity compensation with multi-turn RF coils<sup>6,8</sup> offers an opportunity for sensitive MRI of hyperpolarized contrast agents in low magnetic fields, where magnetic susceptibility and subject induced  $B_1$  inhomogeneity can be significantly minimized to the extent that no scan preparation (e.g. shimming and  $B_1$  mapping) is required potentially allowing to true sub-second scan speed of hyperpolarized MR with minimized cost of MRI scanner.

**References:**

- (1) Abragam, A.; Goldman, M. *Rep. Prog. Phys.* **1978**, *41*, 395-467.
- (2) Bowers, C. R.; Weitekamp, D. P. *Phys. Rev. Lett.* **1986**, *57*, 2645-2648.
- (3) Bowers, C. R.; Weitekamp, D. P. *J. Am. Chem. Soc.* **1987**, *109*, 5541-5542.
- (4) Bhattacharya, P.; Harris, K.; Lin, A. P.; Mansson, M.; Norton, V. A.; Perman, W. H.; Weitekamp, D. P.; Ross, B. D. *Magn. Reson. Mat. Phys. Biol. Med.* **2005**, *18*, 245-256.
- (5) Goldman, M.; Johannesson, H. C. *R. Physique* **2005**, *6*, 575-581.
- (6) Tsai, L. L.; Mair, R. W.; Rosen, M. S.; Patz, S.; Wilsworth, R. L. *J. Magn. Reson.* **2008**, *193*, 274-285.
- (7) Waddell, K. W.; Coffey, A. M.; Chekmenev, E. Y. *J. Am. Chem. Soc.* **2011**, *133*, 97-101.
- (8) Coffey, A. M.; Shchepin, R. V.; Wilkens, K.; Waddell, K. W.; Chekmenev, E. Y. *J. Magn. Reson.* **2012**, *220*, 94-101.
- (9) Feng, B.; Coffey, A. M.; Colon, R. D.; Chekmenev, E. Y.; Waddell, K. W. *J. Magn. Reson.* **2012**, *214*, 258-262.
- (10) Shchepin, R. V.; Coffey, A. M.; Waddell, K. W.; Chekmenev, E. Y. *J. Am. Chem. Soc.* **2012**, *134*, 3957-3960.
- (11) Shchepin, R. V.; Chekmenev, E. Y.; Vanderbilt University; US patent 13/405,074 Unsaturated Choline Analogs and Chemical Synthesis Thereof, 2012.
- (12) Chen, A. P.; Kurhanewicz, J.; Bok, R.; Xua, D.; Joun, D.; Zhang, V.; Nelson, S. J.; Hurd, R. E.; Vigneron, D. B. *Magn. Reson. Imaging* **2008**, *26*, 721-726.

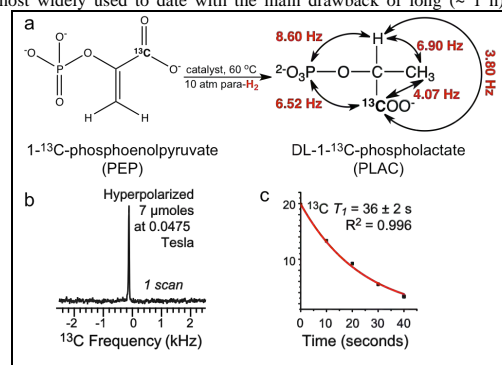


Figure 1. a) PHIP polarization of  $1\text{-}^{13}\text{C}$ -PEP resulting in phosphate protected  $1\text{-}^{13}\text{C}$ -lactate,  $1\text{-}^{13}\text{C}$ -phospholactate, b) single scan  $^{13}\text{C}$  spectrum of 7 micromoles of 1% hyperpolarized  $1\text{-}^{13}\text{C}$ -phospholactate recorded *in situ* at 0.0475 T PHIP polarizer, c)  $^{13}\text{C}$   $T_1$  decay of hyperpolarized  $^{13}\text{C}$ -phospholactate at 0.0475 T.

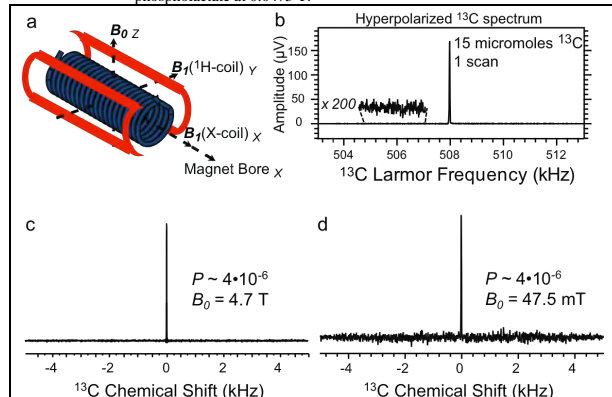


Figure 1. a) Alignment of H-X RF coils, magnetic field and magnet bore, b) Single acquisition spectrum of 15 micromoles (< 2 mg) of hyperpolarized HEP contrast agent with 20% polarization or enhancement  $\epsilon \sim 5,000,000$  at 0.0475 T, c) & d) sensitivity comparison at high and low field.  $^{13}\text{C}$  spectroscopy of 1.0 g of sodium  $1\text{-}^{13}\text{C}$ -acetate solution in 2.8 mL 99.8%  $\text{D}_2\text{O}$ .

**"XeUS"—A Second-Generation 'Open Source' Clinical-Scale  $^{129}\text{Xe}$  Polarizer for Xenon-Induced Polarization**

Panayiotis Nikolaou<sup>1</sup>, Aaron Coffey<sup>1</sup>, Laura Walkup<sup>2</sup>, Brogan Gust<sup>2</sup>, Hayley Newton<sup>3</sup>, Iga Muradyan<sup>4</sup>, Matthew Rosen<sup>5</sup>, Samuel Patz<sup>4</sup>, Michael J. Barlow<sup>3</sup>, Boyd M. Goodson<sup>2</sup> and Eduard Chekmenev<sup>1</sup>

<sup>1</sup>Vanderbilt University Institute of Imaging Science, Nashville, TN; <sup>2</sup>Southern Illinois University Carbondale, Department of Chemistry & Biochemistry, Carbondale, IL; <sup>3</sup>Sir Peter Mansfield Magnetic Resonance Centre, University of Nottingham, Nottingham, UK; <sup>4</sup>Brigham & Women's Hospital, Boston, MA; <sup>5</sup>Harvard University Department of Physics /Harvard Smithsonian Center of Astrophysics and Martinos Center for Biomedical Imaging, Cambridge MA

Owing to the detection sensitivity provided by their high, non-equilibrium magnetization, hyperpolarized (HP) gases (e.g.  $^{129}\text{Xe}$  and  $^3\text{He}$ ) are finding use in a growing number of MRS/MRI applications—ranging from biomedical imaging and spectroscopy, to probing molecular and materials surfaces [1-4]. Although  $^3\text{He}$  has a nearly three-fold greater gyromagnetic ratio (and until recently [5-8], was generally considered easier to hyperpolarize),  $^{129}\text{Xe}$  is more naturally abundant (by several orders of magnitude), and xenon possesses higher solubility in blood and other tissues. Moreover,  $^{129}\text{Xe}$ 's proclivity for interacting with other substances and its much wider chemical shift range make it a more sensitive MR probe of chemical and biological environments [1].

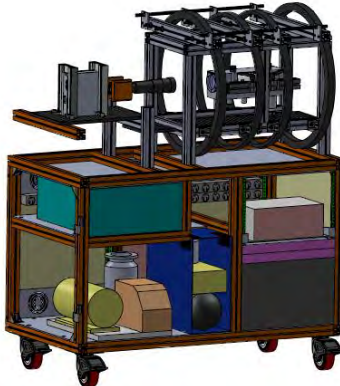
HP $^{129}\text{Xe}$  is usually created by spin-exchange optical pumping (SEOP) [9]. It is traditionally expected that high  $^{129}\text{Xe}$  polarizations ( $P_{\text{Xe}}$ ) can only be obtained with low in-cell Xe densities, because: (1) higher Xe densities increase the destruction of the alkali metal polarization from non-spin-conserving collisions; and (2) higher total pressures tend to quench the (more efficient) van der Waals contribution to Rb-Xe spin exchange [9]. Indeed, many polarizer designs tend to go to great lengths to produce large amounts of HP $^{129}\text{Xe}$  while still satisfying this condition within the cell. In past work from the SIUC/Nottingham collaboration [10,11] exploring batch-mode and "stopped-flow" [12] Rb/Xe SEOP under conditions of high resonant laser flux, an unexpected, inverse relationship was found between the optimal temperature for performing Rb/Xe SEOP and the in-cell Xe density that could be exploited to provide surprisingly high  $P_{\text{Xe}}$  values at high in-cell Xe densities [10,11].



Scaling up from these results, our consortium recently constructed an automated large-scale (>1 L/hr) first-generation 'open-source'  $^{129}\text{Xe}$  polariser (dubbed "XeNA"). Comprised mostly of off-the-shelf components (including a 200 W VHG-narrowed LDA laser), XeNA can be used for clinical, pre-clinical, and materials NMR/MRI applications—and is now cleared by FDA for operation at Brigham & Women's Hospital. Unlike most clinical-scale Xe polarizers, this first-generation device runs with Xe-rich gas mixtures (up to 2000 Torr in a 500 cc cell) in either single-batch or stopped-flow mode, in part negating the usual requirement to cryo-collect the HP $^{129}\text{Xe}$ . In-cell (during SEOP)  $P_{\text{Xe}}$  values of up to ~90%, ~57%, ~50%, & ~28% have been measured for Xe partial pressures of ~300, ~500, ~760, & ~1570 Torr, respectively;  $P_{\text{Xe}}$  of ~41% and ~28% have been measured after transfer of the HP $^{129}\text{Xe}$  to Tedlar bags at 3 T [13].

Taking what we have learned from constructing our first-generation  $^{129}\text{Xe}$  polarizer, we have designed (and are currently constructing) our second-generation  $^{129}\text{Xe}$  polarizer (dubbed "XeUS"). XeUS's design includes a variety of improvements and new technologies. For example, the next-generation water-cooled 200 W VHG-narrowed LDA laser possesses a novel attached air-cooled optical train assembly (designed by QPC and the consortium). Implementation of a large thermoelectric cooler (TEC) and quiet miniature air compressor eliminates the need for external gas or liquid-N<sub>2</sub> supplies for heating / cooling of the OP cell oven or for pneumatic valve operation; the polycarbonate oven for the OP cell is manufactured via 3D printing and houses the TEC heating and cooling of the cell. The GUI-controlled and automated gas manifold and its operation is simplified in part by the use a single tank of pre-mixed  $^{129}\text{Xe}/\text{N}_2$  gas and maintaining overpressure throughout the space upstream from the cell (a change that should also prolong the operational lifetime of the alkali metal in the OP cells by reducing oxidation, while also reducing the delay time between the preparation of different HPXe batches). The four magnetic-coil configuration follows a "Barker" design [14] providing a more homogeneous magnetic field compared to a regular Helmholtz setup. The device is expected to produce >1 L/hr of  $^{129}\text{Xe}$  with  $P_{\text{Xe}} > 20\%$ . Importantly, XeUS will be integrated with an apparatus that will utilize the resulting HPXe as a hyperpolarization source for the nuclear spins of other species ("Xenon-Induced Polarization", or XIP).

**Acknowledgments:** Work at SIUC and Vanderbilt is supported by a DoD CDMRP Era of Hope Award W81XWH-12-1-0159/BC112431. M.J.B is supported by the School of Medical & Surgical Sciences, U. of Nottingham. **References:** [1] Goodson, *JMR*, **155** 157 (2002); [2] Mugler, et al., *Magn. Reson.Med.* **37** 809 (1997), [3] Leawood, et al., *Concepts Magn. Reson.* **13** 277 (2001); [4] Patz, et al., *Eur J. Radiol.* **64** 335 (2007), [5] Driehuys, et al. *APL* **69**, 12 (1996); [6] Ruth, et al. *APB* **68**, 93 (1999); [7] Zook, et al., *JMR* **159**, 175 (2002); [8] Ruset et al., *PRL* **96**, 053002 (2006); [9] Walker & Happer, *Rev. Mod. Phys.* **69**, 629 (1997); [10] Whiting, Nikolaou, et al., *JMR* **208**, 298 (2011); [11] Nikolaou, et al. *JMR*, **197**, 249 (2009); [12] Rosen et al., *Rev. Sci. Inst.* **70**, 1546 (1999); [13] Nikolaou et al., in preparation for submission; [14] Barker, et al., *J. Sci. Instr.* **26**, 273 (1949).



## High (~30-90%) $^{129}\text{Xe}$ Hyperpolarization at High Xe Densities Using an ‘Open-Source’ Polarizer for Clinical and Materials MRS/MRI

Panayiotis Nikolaou<sup>1,2</sup>, Aaron Coffey<sup>1</sup>, Laura Walkup<sup>2</sup>, Brogan Gust<sup>2</sup>, Nicholas Whiting<sup>3,\*</sup>, Hayley Newton<sup>3</sup>, Scott Barcus<sup>2,4</sup>, Iga Muradyan<sup>5</sup>, Mikayel Dabaghyan<sup>5</sup>, Gregory D. Moroz<sup>6</sup>, Matthew Rosen<sup>7</sup>, Samuel Patz<sup>5</sup>, Michael J. Barlow<sup>3</sup>, Eduard Chekmenev<sup>1,8,9</sup>, and Boyd M. Goodson<sup>2</sup>

<sup>1</sup>Department of Radiology, Vanderbilt University Institute of Imaging Science, Nashville, TN; <sup>2</sup>Department of Chemistry & Biochemistry, Southern Illinois University Carbondale, Carbondale, IL; <sup>3</sup>Sir Peter Mansfield Magnetic Resonance Centre, University of Nottingham, Nottingham, UK; <sup>4</sup>REU undergraduate researcher, home institution: Department of Physics, Drake University, Des Moines, IA; <sup>5</sup>Brigham & Women’s Hospital and Harvard Medical School, Boston, MA; <sup>6</sup>Graduate School Central Research Shop, Southern Illinois University, Carbondale, IL; <sup>7</sup>Department of Physics, Harvard University/Harvard Smithsonian Center of Astrophysics and Martinos Center for Biomedical Imaging, Cambridge MA;

<sup>8</sup>Department of Biomedical Engineering, Vanderbilt University, Nashville, TN; <sup>9</sup>Department of Biochemistry, Vanderbilt University, Nashville, TN  
\* present address: MD Anderson Cancer Center, Houston, TX

Owing to the detection sensitivity provided by their high, non-equilibrium nuclear spin polarizations, hyperpolarized (HP) noble gases (e.g.  $^{129}\text{Xe}$  and  $^3\text{He}$ ) are utilized in a growing number of MRS/MRI applications—ranging from biomedical imaging and spectroscopy to probing molecular and materials surfaces [1]. Lung imaging with HP $^{129}\text{Xe}$  is of particular interest [2]; although the gyromagnetic ratio of  $^{129}\text{Xe}$  is smaller than that of  $^3\text{He}$ , xenon is far more naturally abundant (and possesses higher solubility in blood). However, a major obstacle towards implementing HP $^{129}\text{Xe}$  for clinical imaging has been the ability to cheaply and easily generate large quantities of HP gas with high  $^{129}\text{Xe}$  polarizations ( $P_{\text{Xe}}$ ). HP $^{129}\text{Xe}$  is

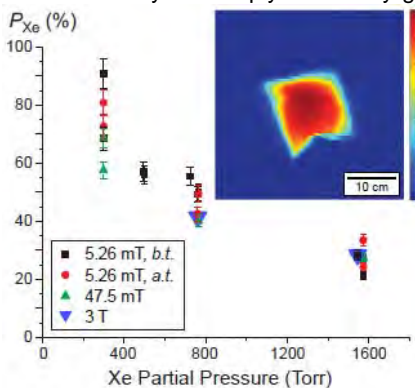


Fig. 1 (left):  $P_{\text{Xe}}$  values measured at 5.26 mT, 47.5 mT, and/or 3 T, plotted versus xenon partial pressure during SEOP. Labels ‘b.t.’ and ‘a.t.’ respectively refer to measurement obtained “before” and “after” Xe gas was transferred to another container. Inset: 2D FLASH  $^{129}\text{Xe}$  projection image of HPXe in a Tedlar bag following transport to 3 T (FOV: 40 cm; slice thickness: 1.7 cm; TE/TR: 2.6/5.1 ms, flip angle:  $\sim 4^\circ$ ; SNR ~40:1).

(during SEOP)  $P_{\text{Xe}}$  values of up to ~90%, ~57%, ~50%, and ~25% have been measured for Xe partial pressures of ~300, ~500, ~760, and ~1570 Torr, respectively (Fig. 1).  $P_{\text{Xe}}$  values of ~41% and ~28% have been measured after transfer of the HP $^{129}\text{Xe}$  to Tedlar bags at 3 T (Fig. 1, inset). In-bag  $T_1$ ’s of ~38 min and nearly 6 hr at low field and 3 T, respectively, have been recorded—more than long enough for a variety of potential experimental modalities. The device has received FDA and internal IRB approval. Finally, we will report on *in vivo* experiments, which are now underway.

usually created via spin-exchange optical pumping (SEOP [3]). It is generally anticipated that high  $P_{\text{Xe}}$  values are achievable via SEOP only with low in-cell Xe densities; thus, most large-scale xenon polarizing devices (“polarizers”, including those from commercial sources) go to great lengths to satisfy this condition within the cell. Such polarizers also tend to be complex, expensive, and strictly regulated by their controlling entities—factors that hinder large scale HP $^{129}\text{Xe}$  generation for many unaffiliated laboratories.

Building upon previous results exploring  $^{129}\text{Xe}$  SEOP under conditions of high resonant laser fluxes and high xenon densities [4,5], here we present results obtained with our collaboration’s first-generation large-scale (>1 L/hr) “open-source” xenon polarizer for clinical, pre-clinical, and materials NMR/MRI applications. Comprised of mostly off-the-shelf components (including a 200 W VHG-narrowed LDA laser), our automated, modular polarizer is easy to use and employs a simplified “open-source” design, readily implementable in other laboratories. Unlike most clinical-scale Xe polarizers, our device runs with xenon-rich gas mixtures (up to 1800 Torr in a 500 cc cell) in either single-batch or stopped-flow mode, in part negating the usual requirement to cryo-collect the HP $^{129}\text{Xe}$  (and potentially opening a door to studies of quadrupolar noble gas nuclei [6]). Up to four independent methods were utilized to probe the spin polarization achieved with the polarizer—including *in situ* field-cycled near-IR spectroscopy [4] (to probe the alkali metal electron spin polarization), *in situ* low-field  $^{129}\text{Xe}$  NMR (calibrated with thermal  $^1\text{H}$  NMR); xenon transfer to 47.5 mT for  $^{129}\text{Xe}$  NMR (calibrated with thermal  $^{13}\text{C}$  NMR), and xenon transfer and  $^{129}\text{Xe}$  NMR at 3 T (calibrated against thermal  $^{129}\text{Xe}$  NMR)—and excellent agreement was observed among these different approaches. In-cell

### References:

- [1] B.M. Goodson, *J. Magn. Reson.*, **155**, 157 (2002); [2] S. Patz, et al., *Eur J. Radiol.*, **64**, 335 (2007); [3] T. Walker & W. Happer, *Rev. Mod. Phys.*, **69**, 629 (1997); [4] P. Nikolaou, et al., *J. Magn. Reson.* **197**, 249 (2009); [5] N. Whiting, et al., *J. Magn. Reson.*, **208**, 298 (2011); [6] Z. I. Cleveland et al., *J. Chem. Phys.* **124**, 044312 (2006).

## Improving imaging sensitivity of hyperpolarized MR at low magnetic detection field strengths

Aaron M. Coffey<sup>1,2</sup>, Milton Truong<sup>2</sup>, Eduard Y. Chekmenev<sup>1,2</sup>

<sup>1</sup> Department of Biomedical Engineering, Vanderbilt University, Nashville, TN, 37235, United States

<sup>2</sup> Institute of Imaging Science, Vanderbilt University, Nashville, TN, 37232, United States

Hyperpolarization technologies have lead to sensitivities greater than conventional MRI or MRS by several orders of magnitude increasingly improving ability to assay cellular metabolism at the molecular level<sup>1,2</sup>. Clinical implementation has hinged on two critical developments: on-site production capacity for short-lived contrast agents and capability for efficient MRI of these agents<sup>3</sup>. While the increasing commercial availability of DNP, SABRE, PASADENA, and PHIP based systems<sup>4</sup> have made contrast agents more accessible, the latter remains largely unaddressed in the low field regime outside the domain of hyperpolarized noble gas imaging. The success of low field noble gas imaging systems<sup>5,6</sup> has demonstrated the utility of detection at low magnetic field strengths. Hyperpolarized technologies permit preparation of nuclear spin states where the detected nuclear spin polarization is independent of the applied magnetic field  $B_0$  and signal levels depend on the magnetic moment of the observed nucleus and Larmor frequency  $\omega_0$ . This NMR detected signal voltage, known<sup>7,8</sup> to correspond to the electromotive force ( $Emf$ ) arising from Faraday's law of induction, is linearly proportional to the number of turns ( $N$ ) of RF coil and the change of magnetic flux  $\Phi_B$  through a single loop. The  $Emf$  may also be expressed as  $|Emf| \propto N \cdot \omega_0 \cdot P \cdot \mu$ , where  $P$  is the nuclear spin polarization, and  $\mu$  is the magnetic moment of nuclear spin<sup>9</sup>. Multi-turn coils at low  $\omega_0$  creating high levels of induced  $Emf$  can provide a highly sensitive means for MR detection of hyperpolarized compounds. The practicality of this approach to achieving high sensitivity is demonstrated here for <sup>13</sup>C and <sup>1</sup>H imaging of sodium 1-<sup>13</sup>C-acetate phantoms with constant polarization simulating the condition of the hyperpolarized state at 2.02 MHz and 0.508 MHz Larmor frequencies.

Two spherical phantoms of sodium 1-<sup>13</sup>C-acetate were used for <sup>1</sup>H and <sup>13</sup>C imaging comparison. <sup>1</sup>H imaging was performed on 1.0 g of sodium 1-<sup>13</sup>C-acetate in 2.8 mL of 99.8% D<sub>2</sub>O (Fig. 1). <sup>1</sup>H (flip angle  $\alpha = 18^\circ$ , spectral width (SW) of 10 kHz, 6.4 ms acquisition time) and <sup>13</sup>C ( $\alpha = 90^\circ$ , SW = 5 kHz, 6.4 ms acquisition time) images were acquired on a 4.7 T Varian scanner using a multinuclear Doty Scientific RF probe with a FSSFP sequence. The phantoms were similarly imaged on a 0.0475 T Magritek spectrometer with a Magritek gradient coil insert and custom in-house multinuclear RF probes of same 38 mm diameter and very similar coil volume using a fast gradient echo sequence with the same imaging parameters except for <sup>13</sup>C flip angle  $\alpha = 18^\circ$ , not  $90^\circ$ . For <sup>13</sup>C, the phantom was imaged 5 s after pre-polarization at 7 T, after which <sup>13</sup>C polarization was  $116.0 \pm 0.5\%$  4.7 T thermal equilibrium polarization. <sup>1</sup>H imaging was performed 5 s after pre-polarization at 9.4 T with  $65 \pm 1\%$  4.7 T polarization.

To the best of our knowledge, this is the first demonstration that low field imaging can approach the sensitivity of high field one under conditions of field independent polarization. Based on these results, we anticipate that low field *in vivo* hyperpolarized MRI would outperform the sensitivity of the high field, because of (i) much lower magnetic field susceptibility resulting in much better  $B_0$  field homogeneity across the subject, (ii) potential use of cryo-cooled RF, and (iii) more homogeneous  $B_1$  and significantly reduced specific absorption rate (SAR).

Funding sources: NIH R25 CA136440, 3R00 CA134749, DOD W81XWH-12-1-0159/BC112431.

**References:** (1) Lupo, J.M.; et al. *Magn. Reson. Imaging* **28**, 153–162 (2010). (2) Day, S.E.; et al. *Nat. Med.* **13**, 1382–1387 (2007). (3) Kurhanewicz, J.; et al. *Neoplasia* **13**, 81–97 (2011). (4) Green, R.A.; et al. *Prog. Nucl. Mag. Res. Sp.* **67**, 1–48 (2012). (5) Lilburn, D.; Pavlovskaya, G.E.; Meersmann, T. *J. Magn Reson* (2012). (6) Tsai, L.; Mair, R.; Rosen, M.; Patz, S.; Walsworth, R. *J Magn Reson* **193**, 274–285 (2008). (7) Hoult, D. I.; Richards, R. E. *J Magn Reson* **24**, 71–85 (1976). (8) Hoult, D.; Bhakar, B. *Concept Magnetic Res* **9**, 277–297 (1997). (9) Coffey, A. M., Shchepin, R. V., Wilkens, K., Waddell, K. W. Chekmenev, E. Y. *J. Mag. Res.* **220**:94–101 (2012).

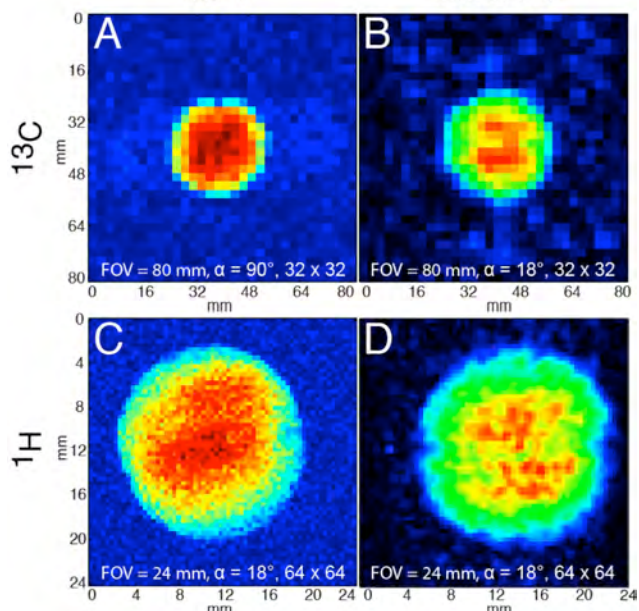


**Figure 1.** 2D images acquired on a 4.7 T Varian scanner with a multinuclear Doty RF coil and on a 0.0475 T Magritek spectrometer equipped with a gradient insert and in-house multinuclear RF coils for identical samples with identical imaging parameters except <sup>13</sup>C flip angle. <sup>13</sup>C imaging of 5.18 g of sodium 1-<sup>13</sup>C-acetate in 99.8% D<sub>2</sub>O (A) at 4.7 T and (B) at 0.0475 T 5 s after pre-polarization at 7 T. <sup>1</sup>H imaging of 1.0 g of sodium 1-<sup>13</sup>C-acetate in 99.8% D<sub>2</sub>O (C) at 4.7 T and (D) at 0.0475 T 5 s after pre-polarization at 9.4 T.

## An ‘Open-Source’ $^{129}\text{Xe}$ Polarizer for Clinical Imaging and Secondary Hyperpolarization of $^{13}\text{C}$ Tracers for Molecular Imaging of Cancer

Panayiotis Nikolaou, Eduard Chekmenev

### Background

Our collaboration (Rosen - Harvard University, Goodson - Southern Illinois University, Patz - Brigham and Women’s, Barlow – University of Nottingham, UK) has recently constructed a large-scale ( $>1 \text{ L/hr}$ )  $^{129}\text{Xe}$  polarizer (XENA) for clinical, pre-clinical, and materials NMR/MRI applications (Fig. 1). Comprised mostly of off-the-shelf components, our automated, modular polarizer is easy to use and employs a simplified “open-source” design that will be readily implementable in other laboratories. Furthermore, the 2<sup>nd</sup> generation polarizer funded by the Department of Defense will be constructed at VUIIS and will be implemented in Xenon Induced Polarization experiments of  $^{13}\text{C}$  tracers for molecular imaging of cancer.

### Approach

HP $^{129}\text{Xe}$  is usually prepared by spin-exchange optical pumping (SEOP) [1]. It is typically expected that high  $^{129}\text{Xe}$  polarizations ( $P_{\text{Xe}}$ ) can only be obtained with low in-cell Xe densities, because: (1) higher Xe densities increase the destruction of the alkali metal polarization from non-spin-conserving collisions; and (2) higher total pressures tend to quench the (more efficient) van der Waals contribution to Rb-Xe spin exchange [1]. Indeed, many polarizer designs produce large amounts of HP $^{129}\text{Xe}$  while still satisfying this low-density condition within the cell. In recent work from the SIUC/Nottingham collaboration [2,3] exploring batch-mode and “stopped-flow” [3] Rb/Xe SEOP under conditions of high resonant laser flux, an unexpected, inverse relationship was found between the optimal temperature for performing Rb/Xe SEOP and the in-cell Xe density [2,3]—an effect that was recently exploited to achieve surprisingly high  $P_{\text{Xe}}$  values at high in-cell Xe.

### Results

$^{129}\text{Xe}$  polarizations of ~70%, ~44%, and ~30% (calibrated with built-in low-field  $^1\text{H}$  NMR) have been measured for Xe partial pressures of 300, 760, and 1600 Torr, respectively using XENA. XENA was installed in Brigham and Women’s Hospital for on-going clinical trial.

### Significance

Unlike most other clinical-scale Xe polarizers, this device runs with xenon-rich gas mixtures (up to 2000 Torr in a 500 cc cell) in either single-batch or stopped-flow mode, in part negating the usual requirement to cryo-collect the hyperpolarized  $^{129}\text{Xe}$  (simplifying gas handling while eliminating polarization losses associated with freeze-thaw cycles). One goal with the open-source design is to facilitate greater implementation of HPXe MR technology in other labs and feedback for future improvements; moreover, shared designs in multiple locations should also facilitate comparisons of results, data sharing, accelerated development and clinical use. Our design will also allow exploration of alternate SEOP approaches including optical excitation geometries, HPXe storage and delivery methodologies, and the use of cesium.

### References

- [1] Walker & Happer, *Rev. Mod. Phys.* **69**, 629 (1997)
- [2] Whiting, et al., *J. Magn. Reson.* **208**, 298 (2011)
- [3] Nikolaou, et al. *J. Magn. Reson.* **197**, 249 (2009)

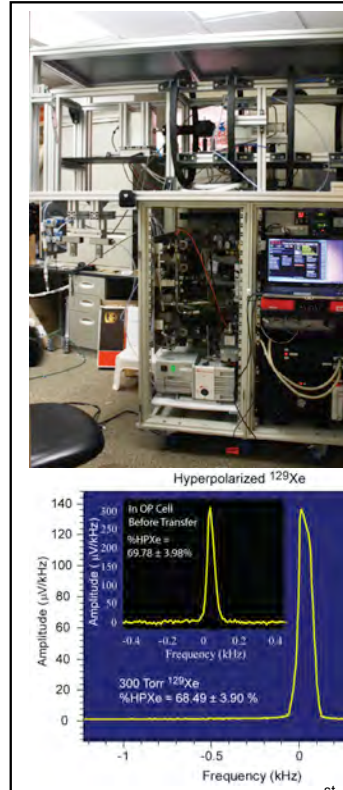


**Figure 1:** (top) Photograph of 1<sup>st</sup> generation automated Xe polarizer; (bottom) low field MR spectroscopy of produced hyperpolarized  $^{129}\text{Xe}$  at natural abundance of 26.4% at 300 torr Xe in external portable phantom measured at 47.5 mT and (inset) *in situ* quality assurance measurement in optical polarizing cell at 5.3 mT before transfer to 47.5 mT system (almost no  $P_{\text{Xe}}$  loss).

#### **Appendix 4: Manuscripts Published and Accepted**

One peer-reviewed manuscript supported by this funding was accepted (7) and one manuscript was conditionally accepted by *PNAS* (1). The copies of published and accepted manuscript are attached in the end of this report.

# Current and emerging quantitative magnetic resonance imaging methods for assessing and predicting the response of breast cancer to neoadjuvant therapy

Richard G Abramson<sup>1,2,9</sup>

Lori R Arlinghaus<sup>1,2</sup>

Jared A Weis<sup>1,2</sup>

Xia Li<sup>1,2</sup>

Adrienne N Dula<sup>1,2</sup>

Eduard Y Chekmenev<sup>1–4,9</sup>

Seth A Smith<sup>1–3,5</sup>

Michael I Miga<sup>1–3,6</sup>

Vandana G Abramson<sup>7,9</sup>

Thomas E Yankeelov<sup>1–3,5,8,9</sup>

<sup>1</sup>Institute of Imaging Science,

<sup>2</sup>Department of Radiology and Radiological Sciences, <sup>3</sup>Department of Biomedical Engineering,

<sup>4</sup>Department of Biochemistry,

<sup>5</sup>Department of Physics, <sup>6</sup>Department of Neurosurgery, <sup>7</sup>Department of Medical Oncology, <sup>8</sup>Department of Cancer Biology, <sup>9</sup>Vanderbilt-Ingram Cancer Center, Vanderbilt University, Nashville, TN, USA

**Abstract:** Reliable early assessment of breast cancer response to neoadjuvant therapy (NAT) would provide considerable benefit to patient care and ongoing research efforts, and demand for accurate and noninvasive early-response biomarkers is likely to increase. Response assessment techniques derived from quantitative magnetic resonance imaging (MRI) hold great potential for integration into treatment algorithms and clinical trials. Quantitative MRI techniques already available for assessing breast cancer response to neoadjuvant therapy include lesion size measurement, dynamic contrast-enhanced MRI, diffusion-weighted MRI, and proton magnetic resonance spectroscopy. Emerging yet promising techniques include magnetization transfer MRI, chemical exchange saturation transfer MRI, magnetic resonance elastography, and hyperpolarized MR. Translating and incorporating these techniques into the clinical setting will require close attention to statistical validation methods, standardization and reproducibility of technique, and scanning protocol design.

**Keywords:** treatment response, presurgical treatment, neoadjuvant chemotherapy

## Introduction

Chemotherapy and hormonal therapy for early stage breast cancer can be administered in either the adjuvant (after surgery) or neoadjuvant (before surgery) settings. Potential advantages to neoadjuvant therapy (NAT) include presurgical reduction of tumor burden, which may allow certain patients to undergo breast conservation therapy rather than mastectomy, and earlier treatment of possible occult micrometastatic disease with the primary breast mass acting as a “marker” for treatment effectiveness (as opposed to adjuvant chemotherapy, where no such marker exists for response of systemic micrometastases).<sup>1</sup> NAT also allows patients time to undergo genetic testing if there is a suspicion of an underlying BRCA 1/2 mutation, which if found may prompt patients to consider mastectomy rather than lumpectomy. At present, NAT is offered primarily to patients with larger tumors, tumors fixed to the chest wall, or clinically matted lymph nodes or skin involvement. However, current clinical trials are evaluating the use of different NAT regimens in multiple patient groups, including those with smaller tumors,<sup>2</sup> and it is anticipated that these studies will lead to increased use of NAT in early stage breast cancer across a broad spectrum of patients.

With more breast cancer patient receiving NAT, more available NAT regimens, and multiple emerging drug agents and combinations requiring evaluation and comparison with existing options, reliable assessment of treatment response has emerged

Correspondence: Richard G Abramson  
Vanderbilt University Medical Center,  
Department of Radiology and  
Radiological Sciences, CCC-1121 Medical  
Center North, 1161 21st Avenue South,  
CCC-1121 MCN, Nashville, Tennessee,  
37232-2675, USA  
Tel +1 615 322 6759  
Email richard.abramson@vanderbilt.edu

as an important challenge in both the clinical and research environments. Pathologic response has been established as an independent prognostic marker for overall survival in breast cancer and is currently the gold standard for assessing response to NAT,<sup>3</sup> but techniques that can provide reliable response assessment earlier in the course of therapy are in high demand, driven by several considerations. First, from a clinical perspective, accurate early response assessment would provide the opportunity to replace an ineffective treatment with an alternative regimen, and in so doing potentially avoid or curtail debilitating side effects or toxicities, such as cardiotoxicity from anthracycline agents or neuropathy from taxanes. Second, patients with disease that is refractory to multiple NAT regimens could be referred directly to surgery, assuming this determination is made early enough that their disease is still surgically resectable. Third, from a research perspective, accurate early response assessment would allow for determination of treatment efficacy on a much shortened timescale, with important ramifications for clinical trial design.

At present, there is no uniform approach to the early assessment of breast cancer response to NAT. Palpation, probably the most widely used technique in the clinical setting, is inaccurate for predicting pathologic response<sup>4,5</sup> and is poorly suited for assessment of small tumors. Serial biopsy is invasive and is associated with sampling problems in heterogeneous tumors. Noninvasive imaging techniques, including mammography, ultrasound, and conventional MRI, are often deployed in the clinical setting as ad hoc problem-solving tools and in the research setting as secondary endpoints, but no imaging-based, early-response biomarker has been suitably validated as sufficiently predictive of long-term outcomes to become incorporated either as standard of care in the clinical setting or as a routine component of all clinical trials. The stage is now set for development of accurate, noninvasive, early-response biomarkers for integration into both the clinical and research environments.

This contribution discusses quantitative magnetic resonance imaging (MRI) as a promising platform from which to develop and deploy these biomarkers. We begin by discussing the motivations for using quantitative MRI for assessing breast cancer response to NAT. We then describe, with illustrative examples, several currently available quantitative MRI methods including lesion size measurement, dynamic contrast-enhanced MRI (DCE-MRI), diffusion-weighted MRI (DW-MRI), and proton magnetic resonance spectroscopy (MRS). Looking a bit further on the horizon, we then discuss magnetization transfer (MT) MRI, chemical

exchange saturation transfer (CEST) MRI, MR elastography, and hyperpolarized MR, methods that have been deployed in other disease sites and that may be particularly well suited to breast cancer response assessment. We conclude by addressing certain practical challenges in the clinical translation of quantitative MRI methods.

## Rationale behind quantitative MRI methods for response assessment

Cancer imaging is undergoing a paradigm shift in which quantitative answers are increasingly being sought for questions that have historically motivated a qualitative response. The query “is this cancer responding to therapy” has traditionally been answered by clinical imaging based on the subjective impressions of the observer. However, modern cancer research and treatment now requires objective and reproducible response assessment variables with which to evaluate and compare different treatment strategies. For evaluating treatment response, qualitative imaging interpretation is yielding ground to quantitative imaging response parameters that can be integrated with other quantitative clinical datasets for rigorous statistical evaluations.<sup>6,7</sup>

The current mainstay of objective imaging-based response assessment for solid malignancies is the Response Evaluation Criteria in Solid Tumors (RECIST), a set of published guidelines for image acquisition, lesion evaluation and measurement, and response categorization.<sup>8</sup> RECIST has been successful in providing a standardized approach for imaging-based response assessment and facilitating “apples to apples” comparisons of different cancer treatments, but its emphasis on changes in lesion size has been criticized as failing to capture meaningful changes in tumor biology.<sup>9,10</sup> In particular, RECIST may underestimate the antitumor efficacy of newer drug agents with cytostatic rather than cytotoxic effect, where tumor shrinkage may be minimal or quite delayed. The future of imaging-based quantitative response assessment will likely involve supplementing traditional size-based techniques with more advanced morphological, functional, physiological, cellular, and molecular imaging methods.

For a variety of reasons, MRI is a very promising platform from which to develop advanced quantitative imaging biomarkers for assessing breast cancer response to NAT. First, MRI is already well established as a clinically useful technique in breast cancer detection and characterization,<sup>11</sup> and its use for response assessment would be a natural extension of its current role in clinical care. Second, as an intrinsically digital technique, MRI is capable of generating

quantitative datasets for direct entry into statistical analyses, thus bypassing the need for analog-to-digital conversion or subjective user interpretation that can add to measurement variability. Third, MRI is an extraordinarily flexible and powerful modality with the ability to report on multiple structural and functional parameters that may be relevant to lesion response assessment, as detailed in this review.

It is important to note that response assessment is only one of two goals for imaging during NAT, with the other being assessment of residual disease as an adjunct to surgical planning.<sup>11–14</sup> While it is tempting to think of these two objectives as one and the same, assessment for residual disease fundamentally seeks to depict anatomy, whereas response assessment seeks to evaluate changes in tumor biology and may do so with a variety of techniques reporting on either anatomical or functional changes. The distinction is especially important for MRI, where certain tradeoffs in how images are acquired (eg, between high temporal and high spatial resolution techniques) may theoretically render one imaging protocol more useful for response assessment and another protocol more useful for demonstrating tiny foci of residual tumor. This review focuses on MRI techniques for response assessment, but we address practical issues of protocol design in a later section on clinical translation.

## Currently available quantitative MRI techniques for response assessment

A number of MRI techniques are already available for potential deployment into both clinical and research settings for the assessment of breast cancer response to NAT. These methods include anatomical measurement of lesion size (unidimensional, multidimensional, and volumetric), DCE-MRI, DW-MRI, and MRS. In this section we review the basic theory underlying these techniques (including methods of quantitative analysis), provide examples of relevant clinical and research applications, and discuss opportunities for future development.

## Lesion size measurement

### Theory

By virtue of its exquisite soft tissue contrast and very high spatial resolution, MRI is an extremely powerful technique for demonstrating the morphology of breast lesions. MRI has therefore been evaluated for assessing breast cancer response to therapy using changes in lesion size as the primary measurement variable. MRI-based evaluation of lesion size relies almost exclusively on “contrast-enhanced” imaging ie, imaging following intravenous injection of a paramagnetic contrast

agent (typically a gadolinium chelate) so as to maximize the conspicuity of an enhancing breast lesion against a background of normal breast parenchyma.<sup>15</sup> The literature has incorporated unidimensional, bidimensional, and volumetric (ie, three-dimensional) tumor measurements (Figure 1).

## Applications

Evaluations of MRI-based lesion size measurement in the setting of NAT have focused on two clinical scenarios: (1) evaluation for residual disease at the end of NAT and (2) early assessment of treatment response. With regard to evaluation for residual disease, a significant literature has demonstrated the effectiveness of MRI-based lesion size measurement in predicting results at surgical pathology.<sup>5,16–22</sup> Abraham et al<sup>19</sup> showed that contrast-enhanced MRI at the end of NAT predicted pathologically determined residual disease in 97 percent of cases, outperforming both physical examination and mammography.<sup>19</sup> Balu-Maestro et al<sup>23</sup> compared physical examination, mammography, ultrasound, and MRI and found that MRI was the most reliable for evaluating residual tumor size after NAT. Londero et al<sup>22</sup> found that MRI after NAT identified residual disease better than mammography and also showed that MRI-measured tumor diameters correlated better with pathologic diameters than either mammography or sonography. Chou et al<sup>16</sup> found that tumor volume after NAT (calculated using a segmentation algorithm) was highly correlated with histopathologic estimation of tissue volume.<sup>16</sup>

With regard to early assessment of treatment response, a number of studies have evaluated the ability of early changes in MRI-based lesion size measurement to predict eventual response.<sup>24–26</sup> Martincich et al<sup>25</sup> found that a minimum 65 percent reduction in tumor volume after two cycles of NAT was associated with an eventual major histopathological response. Padhani et al<sup>27</sup> demonstrated that a decrease in bidimensional tumor area after two cycles of NAT predicted pathological response. Loo et al<sup>28</sup> showed that a change in the longest diameter of enhancing tumor

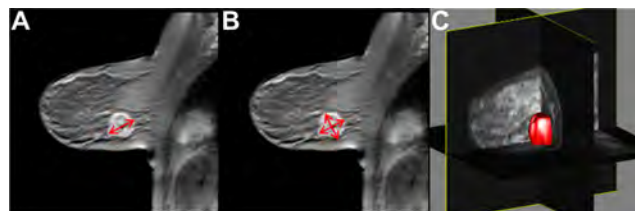


**Figure 1** Lesion size measurement by MRI. **(A)** Unidimensional measurement of tumor long axis diameter. **(B)** Bidimensional measurement of tumor long and short axis diameters. **(C)** Three-dimensional measurement of tumor volume.  
Abbreviation: MRI, magnetic resonance imaging.

predicted pathologic response after two cycles of NAT.<sup>28</sup> The recently published ISPY-1 trial showed that volumetric tumor measurement at mid-treatment outperformed clinical assessment in predicting pathologic response.<sup>29</sup>

### Future directions

Although MRI techniques for lesion size measurement are mature and have been shown to predict changes in true lesion size, MRI-based size measurement has not been widely incorporated into the clinical or research settings for NAT response assessment. In the clinical setting, this is probably due to the prevailing opinion that physical examination provides adequate response assessment in the patient population for whom NAT is currently indicated, ie, patients with large tumors. In the research setting, RECIST-based response biomarkers may be incorporated as secondary endpoints, but current trials invariably rely on pathologic response as the primary endpoint for determining antitumor efficacy. The latter remains true despite some preliminary studies correlating MRI-based size measurement changes with long-term outcomes.<sup>30</sup>

In the future, with the anticipated increased use of NAT in patients with smaller tumors that are poorly assessed by palpation, MRI-based lesion size measurement may become more integrated into clinical algorithms, but there remain several potential problems with lesion size-based response assessment. First, many breast cancers tend to have infiltrative, irregular, and/or multifocal growth, creating problems for reproducible size measurement. Second, as mentioned previously, some new and emerging treatment agents have cytostatic rather than cytotoxic effect and may produce delayed or attenuated lesion shrinkage such that a size-based response assessment methodology may not fully capture relevant changes in tumor biology. Third, when treated, breast cancers can exhibit a variety of different morphological changes including shrinkage from the outside, melting from the inside, and irregular internal ("Swiss cheese") liquefaction; these different patterns would be poorly assessed by methodologies focusing exclusively on unidimensional, bidimensional, or even volumetric measurement.

The biggest long-term challenge for lesion size measurement-based techniques will therefore probably involve integration with other techniques focused more on assessing functional changes in tumor biology, as described in subsequent sections. Integration of different techniques into a comprehensive, multi-purpose MRI examination may be challenging, and will also be described later.

## Dynamic contrast-enhanced MRI (DCE-MRI)

### Theory

DCE-MRI involves the rapid, sequential acquisition of  $T_1$ -weighted images before and after the injection of a paramagnetic contrast agent.<sup>31</sup> As the contrast agent perfuses or diffuses into a voxel or region of interest (ROI), it shortens the native magnetic relaxation times of the tissue as determined by the local concentration of contrast. When the contrast agent leaves the voxel, the relaxation times increase toward their baseline value at a rate determined by local tissue characteristics. Each voxel thus yields a signal intensity time course that can be analyzed to yield estimates of tissue vascularity parameters including perfusion, permeability, and tissue volume fractions.

Both semiquantitative and fully quantitative methods have been developed to perform DCE-MRI analyses. Semiquantitative methods include calculations of the signal enhancement ratio (SER) and the initial area under the enhancement curve (iAUC).<sup>32–36</sup> The SER method, used in the ISPY-1 trial, employs the following calculation:

$$SER = \frac{S_1 - S_0}{S_2 - S_0} \quad (1)$$

where  $S_0$  represents the signal intensity within the lesion before contrast administration,  $S_1$  represents the signal intensity early after contrast injection, and  $S_2$  represents the late postcontrast signal intensity.<sup>32</sup> Given a map of SER values, various derivative parameters are accessible including the SER total tumor volume, SER partial tumor volume, SER washout tumor volume, and the peak SER.

Fully quantitative DCE-MRI analysis typically involves the application of various pharmacokinetic equations to model the movement of contrast agent molecules between tissue and blood vessels over time.<sup>37</sup> Two main approaches have been deployed in breast cancer: the standard Tofts-Kety (TK) and the extended Tofts-Kety (ETK) models.<sup>38</sup> The standard TK model is summarized by:

$$C_t(T) = K^{trans} \cdot \int_0^T C_p(t) \cdot e^{-(K^{trans}/v_e) \cdot (T-t)} dt, \quad (2)$$

where  $K^{trans}$  is the volume transfer constant,  $v_e$  is the extravascular extracellular volume fraction,  $C_t(T)$  is the concentration of contrast in the tissue of interest, and  $C_p(t)$  is the concentration of contrast in blood plasma (also known as the arterial input function). The ETK model incorporates the blood plasma volume fraction,  $v_p$ , as follows:

$$C_t(T) = K^{trans} \int_0^T C_p(t) \exp\left(-(K^{trans}/v_e)(T-t)\right) dt + v_p C_p(t). \quad (3)$$

Both the TK and ETK models assume that all water compartments within tissue are well mixed (ie, are at the fast exchange limit of the nuclear magnetic resonance time scale) so that MRI signal change is completely described by a single relaxation rate constant.<sup>38</sup> After measurement (or estimation) of  $C_t(t)$  and  $C_p(t)$  on a voxel or ROI level, Equations 2 and/or 3 are used to return estimates of  $K^{trans}$ ,  $v_e$ , and  $v_p$ , along with the derived efflux rate constant  $k_{ep}$  ( $k_{ep} \equiv K^{trans}/v_e$ ). The working hypothesis for fully quantitative DCE-MRI in the setting of NAT is that observed changes in these pharmacokinetic parameters can predict treatment response, as illustrated in Figure 2. For a more extensive discussion of DCE-MRI methods in oncology, the interested reader is referred to the review by Yankeelov and Gore.<sup>31</sup>

## Applications

Both semiquantitative and fully quantitative DCE-MRI techniques have been evaluated for assessing treatment response in breast cancer patients undergoing NAT. The best known example of semiquantitative DCE-MRI in this setting is the I-SPY 1 trial,<sup>29</sup> in which patients underwent contrast-enhanced MRI at multiple time points before, during, and after NAT; the authors found that midtreatment change in SER predicted pathologic response with an area under the curve (AUC) of 0.71, higher than clinical assessment (0.63) but slightly lower than change in tumor volume measurement (0.72).<sup>29</sup> Other investigations of semiquantitative DCE-MRI include employment of iAUC for response assessment. For example, Tateishi et al<sup>36</sup> used the percentage area under the time-intensity curve (%AUC) to predict treatment response and reported that although the sensitivity of %AUC (50%)

was not acceptable, the specificity of %AUC of 95.2% was sufficiently high to predict pathologic complete response.<sup>36</sup> Our group has shown that semiquantitative analysis of high temporal resolution DCE-MRI data can predict pathologic response after a single cycle of NAT (unpublished data).

Quantitative analysis of DCE-MRI data has been shown to assess<sup>39</sup> and predict treatment response<sup>27,40</sup> and has also been shown to correlate with 5-year survival.<sup>41–44</sup> Padhani et al<sup>27</sup> found that after two cycles of NAT, both change in tumor size and change in  $K^{trans}$  range on histogram analysis were equally able to predict pathologic response. Ah-See et al<sup>40</sup> analyzed multiple quantitative DCE-MRI parameters and reported that change in  $K^{trans}$  was the best predictor of pathologic nonresponse.<sup>40</sup> Our group found that not only the mean but also the standard deviation of  $K^{trans}$  as estimated by the TK and ETK models, as well as  $v_p$ , can separate complete pathologic responders from nonresponders after a single cycle of NAT.<sup>45</sup>

## Diffusion-weighted MRI (DW-MRI) Theory

Like conventional MRI, DW-MRI records signals from mobile water molecules within tissues, but in DW-MRI the contrast reflects the distance water molecules can migrate or “diffuse” from their original spatial position over a short time interval due to random, thermally-induced motion (ie, Brownian motion). DW-MRI exploits applied gradients of the main magnetic field that allow for localization and calculation of the microscopic diffusion of water molecules. By acquiring two or more images with different degrees of “diffusion weighting” (obtained by applying the diffusion-sensitizing gradients with different amplitudes on successive image acquisitions), an estimate of the amount of molecular water diffusion, termed the apparent diffusion coefficient (ADC), can be calculated at each voxel from

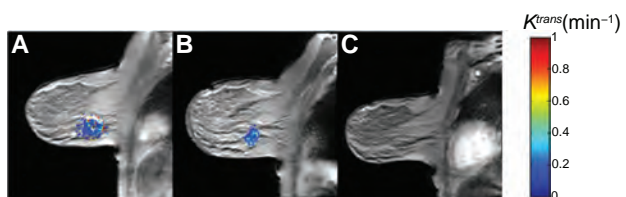


**Figure 2** Fully quantitative DCE-MRI analysis in a breast cancer patient undergoing NAT. **(A)** Pretreatment DCE-MRI analysis yields a baseline calculated mean tumor  $K^{trans}$  value of  $0.3 \text{ min}^{-1}$ . **(B)** DCE-MRI analysis after one cycle of NAT yields a calculated mean tumor  $K^{trans}$  value of  $0.2 \text{ min}^{-1}$ . **(C)** Imaging after completion of NAT shows that the lesion is no longer visible; at surgery, the patient had a pathologic complete response.

**Note:** Ongoing studies are investigating whether early changes in mean tumor  $K^{trans}$  can reliably differentiate pathologic responders from nonresponders.

**Abbreviations:** DCE-MRI, dynamic contrast-enhanced magnetic resonance imaging; NAT, neoadjuvant therapy;  $K^{trans}$ , volume transfer constant.

$$S = S_0 \exp(-b \cdot \text{ADC}), \quad (4)$$

where  $S$  is the signal intensity recorded with application of a diffusion-sensitizing gradient,  $S_0$  is the signal intensity with no diffusion-sensitizing gradient, and  $b$  is a composite variable reflecting various acquisition parameters (including the strength of the gradient pulse, duration of the pulse, and interval between pulses).<sup>46</sup> ADC values from successive voxels can then be aggregated to produce a map of ADC values over the volume of interest (Figure 3).

In general, experimentally-measured ADC values are lower in organized tissues than in free solution because

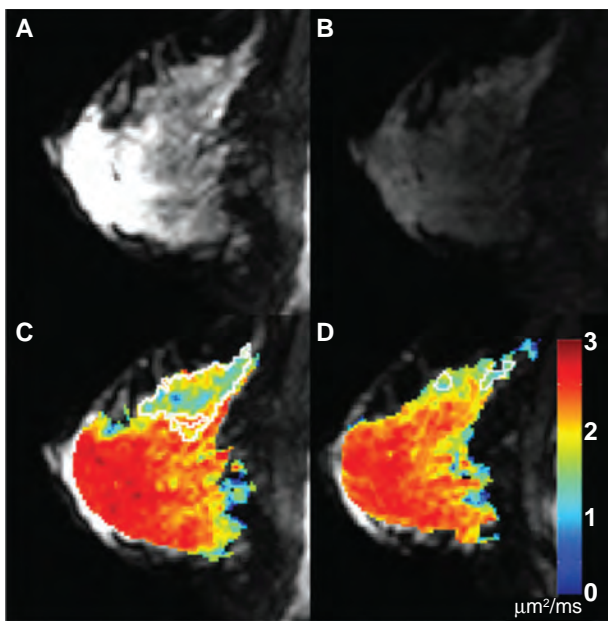


**Figure 3** DW-MRI in a breast cancer patient undergoing NAT. **(A)** On a pretreatment image with no diffusion gradient (ie,  $b = 0 \text{ s/mm}^2$ ), the tumor is difficult to distinguish from background normal parenchyma. **(B)** Pretreatment diffusion-weighted image ( $b = 660 \text{ s/mm}^2$ ) demonstrates subtle patchy increased signal in the deep upper breast, corresponding to an infiltrative tumor. **(C)** Pretreatment quantitative ADC map, with color-coded voxels corresponding to tissue ADC. The tumor region is outlined in white. **(D)** ADC map derived from DW-MRI after one cycle of NAT; the tumor volume (again outlined in white) has markedly decreased.

**Note:** This patient went on to have a complete pathologic response.

**Abbreviations:** DW-MRI, diffusion-weighted magnetic resonance imaging; NAT, neoadjuvant therapy; ADC, apparent diffusion coefficient.

various structures including cell membranes and intracellular organelles tend to restrict or hinder the free movement of water.<sup>47,48</sup> Moreover, cancerous tissues often show significantly reduced ADC values when compared with healthy tissues, a finding typically attributed to the increased cell density of many malignancies.<sup>49</sup> With treatment, intratumoral ADC values often rise, presumably because of decreases in cell density consequent to apoptosis and cell death, with concomitant disruption of cell membranes allowing water molecules to diffuse more freely. This basic paradigm – low tumor ADC values before treatment, followed by rising tumor ADC values with treatment – provides the basic model for DW-MRI as a response assessment technique. Importantly, it has been shown that rising ADC values can occur quite early during treatment,<sup>50–52</sup> thus providing the motivation for studying DW-MRI as an early response biomarker. For a more extensive discussion, the reader is referred to the review by Arlinghaus and Yankeelov.<sup>53</sup>

## Applications

Several studies have correlated changes in ADC on DW-MRI with treatment response in breast cancer patients

undergoing NAT. Early investigations demonstrated increases in mean tumor ADC following chemotherapy<sup>39</sup> and correlated mean tumor ADC increases with radiological response,<sup>54,55</sup> while subsequent studies examined the relationship between mean tumor ADC changes and pathological response. In general, mean tumor ADC has been found to increase after NAT in both pathologic responders and nonresponders but to increase more for pathologic responders.<sup>56–59</sup> Sharma et al<sup>52</sup> showed that at the end of therapy, DW-MRI had a lower sensitivity but a higher specificity than lesion size measurement for differentiating pathologic responders from nonresponders.

More recent studies have looked into changes in ADC early in the treatment course and have begun to investigate whether DW-MRI performed early in treatment can be used to predict response. Pickles et al<sup>51</sup> demonstrated a significant increase in mean tumor ADC after a single cycle of NAT and showed that mean tumor ADC began to change earlier than tumor longest diameter. In a study of 15 patients, mean tumor ADC increased significantly ( $P = 0.008$ ) by 11% after a single cycle of NAT.<sup>60</sup> Li et al<sup>50</sup> reported that after one cycle of NAT, mean tumor ADC significantly increased by 24% in patients who went on to have a complete or partial response and did not change in patients who ultimately exhibited stable or progressive disease.

## Proton magnetic resonance spectroscopy (MRS)

### Theory

In contrast to conventional MRI, which generates anatomical images using signal primarily arising from water, MRS provides information on the concentrations of different metabolites in tissue. This technique can be exploited to detect the altered metabolic signatures of cancer cells. For example, many malignancies demonstrate elevated levels of choline and lactate, the former due to high rates of membrane turnover and the latter due to utilization of anaerobic glycolysis. Choline is present in less than one millimolar concentrations in normal breast tissue but is significantly elevated in malignant breast tumors<sup>61,62</sup> due to choline kinase overexpression driven by HIF-1 $\alpha$ .<sup>63,64</sup>

MRS is more challenging in the breast than in other organs due to the large amount of signal from lipid and to increased magnetic susceptibility at air-tissue interfaces, although the latter is less relevant in single-voxel MRS of the breast. Despite the lower spectroscopic resolution and signal-to-noise ratio of breast MRS compared with MRS in other organs, measurements of choline levels and water-fat (W-F) ratios are feasible in the breast and have been used for

breast cancer diagnosis as well as for monitoring response to treatment during NAT.<sup>65–72</sup>

## Applications

A recent clinical trial reported by Kumar et al<sup>67</sup> demonstrated that malignant breast tissues have elevated W-F levels compared with controls, and that breast cancers decreasing in size with NAT also exhibited decreasing W-F ratios.<sup>67</sup> In a separate clinical trial reported by Tozaki et al<sup>71</sup> using choline MRS in patients undergoing NAT, the reduction rates of choline were statistically significantly different between pathological responders and nonresponders after two treatment cycles, with positive and negative predictive values of choline MRS of 89% and 100%, respectively. Moreover, it was found that the predictive power of choline MRS was greater than that of volumetric tumor measurements. Danishad et al<sup>73</sup> found that choline signal-to-noise ratio may be useful in predicting tumor response to NAT.

## Future directions

Although relatively high predictive power has been demonstrated in preliminary trials, the widespread clinical implementation of W-F and choline MRS for breast cancer treatment response assessment will confront several challenges. First, customized data postprocessing and internal/external signal referencing is required to convert raw spectroscopic data into quantitative information, especially for clinical analysis of multi-voxel MRS data. Second, because the majority of tissue metabolites in vivo besides lipids are present at millimolar concentrations, the MRS sampling voxel must typically be very large (1–8 cm<sup>3</sup>) in order to achieve sufficient signal-to-noise ratio for very dilute metabolites, and this low spatial resolution translates into limited ability to interrogate small tumors and to report on intralesional heterogeneity. Improvements on the low spatial resolution of conventional MRS may result from emerging methods including multivoxel chemical shift imaging<sup>61,70,74</sup> and hyperpolarized MR, discussed below.

## Emerging quantitative MRI techniques for response assessment

Several additional MRI techniques are on the horizon for possible future use in assessing breast cancer response to NAT. Some of these techniques have already been deployed in other disease sites. This section discusses possible applications of MT, CEST, and MR elastography as treatment response biomarkers. For each technique, we briefly discuss the underlying theory as well as opportunities and preliminary applications in breast cancer.

## Magnetization transfer (MT) MRI

### Theory

MT is a method for detecting and quantifying the protons associated with tissue macromolecules. These macromolecular protons cannot be routinely detected with conventional MRI; MT takes advantage of the communication between macromolecular protons and water to elicit an indirect measurement of their properties. MT is typically performed by applying a preparatory off-resonance radiofrequency pulse to selectively saturate protons associated with macromolecules and then measuring the attenuation of the water signal that occurs as a result of the exchange of spin information (magnetization transfer) between the saturated macromolecular protons and free water. The magnetization transfer itself takes place via dipolar coupling and/or chemical exchange.<sup>75</sup>

The typical method for characterizing the MT effect is to compare the signal intensity between a nonsaturated image (or so-called reference acquisition, designated as  $MT_{off}$ ) and an image acquired after application of the off-resonance radiofrequency (RF) pulse ( $MT_{on}$ ). The magnitude of the saturation is proportional to the quantity of saturated macromolecular protons and the efficiency of exchange (or exchange rate) with free water protons (Figure 4). The MT effect is thus characterized by the magnetization transfer ratio (MTR):

$$MTR = 1 - \frac{MT_{on}}{MT_{off}} \quad (5)$$

where  $MT_{on}$  represents the signal intensity with the saturation pulse and  $MT_{off}$  represents the signal intensity from the reference image. The MTR has been shown to be related to the amount of macromolecular protons in tissue.<sup>76</sup> It should be noted that since the MTR measurement is affected by the relaxation and exchange rates, the field strength, and the RF irradiation power, it is only a semiquantitative metric. A quantitative MT approach is necessary to separate the

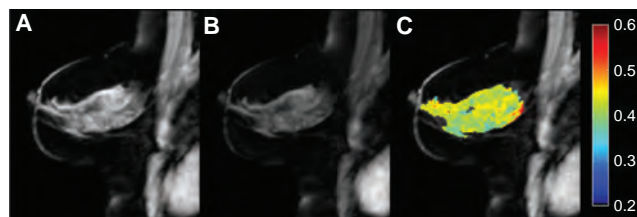


**Figure 4** MT results from a healthy volunteer. (A)  $MT_{off}$ . (B)  $MT_{on}$ . (C) MTR map demonstrating an average 40% reduction in signal (ie,  $MTR = 0.4$ ) in the fibroglandular tissue with good fat suppression.

**Abbreviations:** MT, magnetization transfer;  $MT_{on}$ , signal intensity with the saturation pulse;  $MT_{off}$ , signal intensity from the reference image; MTR, magnetization transfer ratio.

contributions from MT and relaxation effects,<sup>77,78</sup> and the development of clinically feasible quantitative MT techniques is an active area of research.<sup>79</sup> For a more extensive discussion of MT methods, the interested reader is referred to the review by Gochberg and Lepage.<sup>80</sup>

### Opportunities and preliminary applications in breast cancer

While the primary application of MT has been in studies of demyelinating diseases,<sup>81–83</sup> the demonstration of MT's sensitivity to collagen content in meningiomas<sup>84</sup> has led to interest in MT for studying changes in the extracellular matrix (ECM) of the breast. The ECM is a major component of the fibroglandular tissue of the breast and is comprised of a network of macromolecules, including collagen, fibronectin, and laminin. The ECM is known to play a role in tumor development and progression,<sup>85–87</sup> and the role of the ECM in breast cancer has gained increasing attention. For example, Ioachim et al<sup>88</sup> reported that the expression of the ECM macromolecules fibronectin, collagen type IV, and laminin is altered in breast cancer; Levantal et al<sup>89</sup> recently demonstrated that cross-linking of collagen type I is involved in the stiffening of the ECM and tumor migration in breast cancer; and Kakkad et al<sup>90</sup> reported that the concentration of collagen type I is reduced in the hypoxic tumor environment. An initial application of MT in breast cancer showed a significant reduction of MTR in malignancies compared with benign tumors, thought to represent a reduction of the macromolecular pool due to increased proteolytic activity.<sup>91</sup> In the NAT setting, it is hypothesized that changes in macromolecular content in response to successful treatment would result in measurable changes in MTR values. Also, as tumors respond to therapy and shrink, the tumor cells are typically replaced with fibrotic tissue,<sup>92–94</sup> which potentially could lead to an (ultimate) increase in MTR in the case of successful therapy.

## Chemical exchange saturation transfer (CEST) MRI

### Theory

CEST is similar to MT, but rather than focusing on macromolecules, CEST seeks to specifically irradiate tissue metabolites such as amides, amines, and hydroxyl groups that are also in exchange with free water.<sup>95–97</sup> The exchangeable protons on these metabolites have chemical shifts that are significantly smaller than the broad macromolecular pool and exchange at significantly slower rates, which allows for

spectrally selective irradiation via application of an off-resonance RF pulse.<sup>98,99</sup> Under experimental conditions, CEST has been shown to discriminate individual tissue metabolites with high specificity. In addition, because proton chemical exchange rates are pH-dependent, CEST can be used to interrogate for changes in tissue pH.<sup>100</sup> Like MT, CEST can be performed without the use of exogenous contrast agents.

CEST is performed through application of a spectrally-selective saturation pulse prior to an imaging sequence, as shown in Figure 5. This series is repeated while the resonance offset of the saturation pulse is swept through a range of frequencies, typically  $< \pm 10$  ppm. The saturation will affect specific protons, and the observed water signal will be attenuated via direct chemical exchange.<sup>100</sup> CEST results are often examined via a *z*-spectrum, a plot of the signal intensity of water as a function of saturation offset, normalized by the signal intensity of water in the absence of saturation.<sup>101</sup> Example *z*-spectra are shown in Figure 6, which depicts the results of CEST analysis at 3 T on a malignant breast tumor (black line) compared with healthy fibroglandular tissue (gray line). One way the CEST effect can be characterized is by examining the amount of asymmetry observed in the CEST spectra, with the effect at particular offset frequencies related to the exchanging protons of interest.

Perhaps the most widely reported CEST effect is derived from the exchange of amide protons on the backbone of proteins and peptides. In this case, the CEST effect of the amide proton resonance can be characterized by the so-called proton transfer ratio (PTR), a measure of the asymmetry of the *z*-spectrum about the water frequency ( $CEST_{asym}$ ) at  $\Delta\omega = 3.5$  ppm:

$$CEST_{asym} = \frac{S(-\Delta\omega) - S(\Delta\omega)}{S_0}, \quad (6)$$

where  $S(-\Delta\omega)$  and  $S(\Delta\omega)$  are the signal intensities with the saturation at  $\pm\Delta\omega$ , and  $S_0$  is the signal intensity in the absence of saturation. This calculation negates the confounding effects of direct water saturation, which are symmetric about the center of the *z*-spectrum.<sup>102</sup> The measured PTR can be affected



**Figure 5** General pulse sequence diagram for a CEST MRI experiment.  
Note: RF irradiation for a time  $t_s$  with an amplitude of  $B_i$  precedes the excitation ( $\alpha$  degrees) and image acquisition.

**Abbreviations:** CEST MRI, chemical exchange saturation transfer magnetic resonance imaging; RF, radiofrequency.

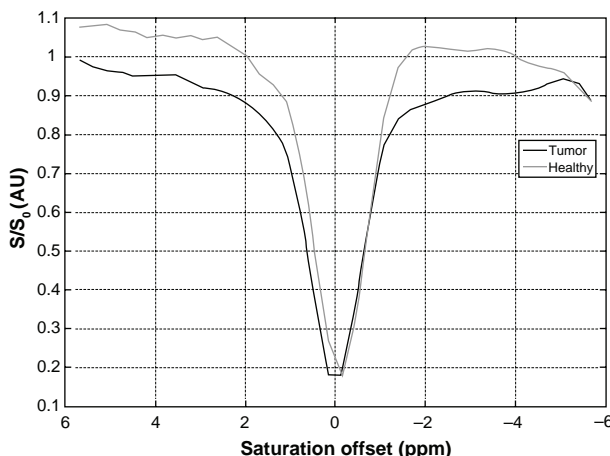


**Figure 6** Example z-spectra arising from a CEST MRI experiment at 3 T.

**Note:** The normalized signal ( $S/S_0$ ) is shown as a function of saturation offset frequency for regions of interest in malignant tumor (black line) and healthy fibroglandular tissue (gray line).

**Abbreviations:** CEST MRI, chemical exchange saturation transfer magnetic resonance imaging; S, signal intensity with saturation;  $S_0$ , signal intensity in the absence of saturation.

by the concentration of exchanging protons as well as the pH, which influences the proton exchange rate. Extensive research is underway to determine the underlying mechanism driving the measured CEST effect in both healthy and diseased tissue. Ongoing research is also investigating innovative pulse sequences<sup>103,104</sup> and alternative quantification strategies<sup>105–107</sup> that may minimize asymmetric magnetization transfer effects from macromolecules, which can confound the PTR measurement.<sup>108</sup> For a more comprehensive introduction to CEST, the reader is referred to the review by Gochberg and Lepage.<sup>80</sup>

### Opportunities and preliminary applications in breast cancer

CEST focused at the amide proton resonance (3.5 ppm) provides information on the amide protons of protein/peptide backbones and has been used to study tissues where either the protein/peptide concentration or the pH may be altered.<sup>95,109–111</sup> This technique, sometimes termed amide proton transfer (APT) imaging, is thought to be especially relevant to cancer imaging because tumor cells may accumulate defective proteins at a higher rate than normal and/or experience alterations in pH due to hypoxia.<sup>112</sup> APT-CEST has been applied to brain,<sup>110</sup> prostate,<sup>113</sup> and breast tumors<sup>106</sup> and has been used to differentiate cellular protein content between tumor and healthy cells.<sup>114</sup>

Our group is actively developing APT-CEST imaging as a potential early treatment response biomarker for breast cancer NAT.<sup>106,115</sup> Figure 7 depicts the measured APT overlaid on an anatomical image for three breast cancer patients before (left column) and after (right column) one cycle of NAT. The

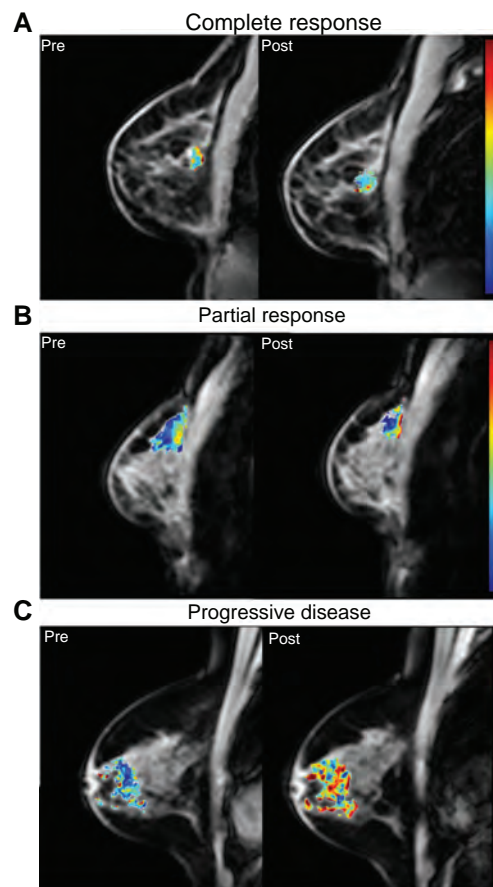


**Figure 7** Amide proton transfer (APT) maps derived from CEST MRI in breast cancer patients undergoing NAT. Baseline (pretreatment) images are presented on the left, and images after one cycle of NAT are presented on the right. **(A)**: patient with complete response after one cycle of therapy (27% decrease in measured APT from baseline). **(B)**: patient with partial response (49% increase in measured APT). **(C)**: patient with progressive disease (78% increase in measured APT).

**Abbreviations:** CEST MRI, chemical exchange saturation transfer magnetic resonance imaging; NAT, neoadjuvant therapy.

top row shows imaging data from a complete responder (27% decrease in measured APT from baseline), the middle row from a partial responder (49% increase in measured APT), and the bottom row from a patient with progressive disease (78% increase in measured APT). These preliminary results demonstrate the potential sensitivity of APT-CEST to the molecular changes occurring early during treatment.

In addition to APT-CEST, there is potential to examine breast cancer by deploying CEST to evaluate tissue glycosaminoglycan content (ie, gagCEST). Many different cell surface and matrix proteoglycan core proteins are expressed in the mammary glands. The level of expression of these core proteins, the structure of their glycosaminoglycan chains, and their degradation are regulated by many of the same effectors that control development and function.<sup>116</sup> Loss or overexpression of proteoglycans in carcinoma cells has been associated with malignant progression<sup>117,118</sup> and has correlated with poor

prognosis,<sup>119</sup> leading to the hypothesis that gagCEST may be developed as a treatment response biomarker in the future. The application of CEST targeting signatures of active tumors brings potential for noninvasive molecular imaging that could be predictive of prognosis.

## Magnetic resonance elastography (MRE)

### Theory

MRE is based on use of the elastic properties of tissue as an imaging contrast mechanism. The general concept of elastography, realized first in ultrasound<sup>120</sup> and later developed in MRI,<sup>121</sup> involves the use of imaging to measure tissue response to applied physical deformation. Sometimes described as a form of “21st century palpation,” elastography allows for generation of tissue elasticity maps providing spatial visualization and quantification of the distribution of elastic properties within an object. Generally, elastography methods employ the simplifying assumption of a linear elastic isotropic constitutive model where mechanical equilibrium is governed by:

$$\nabla \cdot G \nabla \vec{u} + \nabla \frac{G}{1-2v} (\nabla \cdot \vec{u}) + \vec{F} = -(\rho_{tissue} - \rho_{fluid}) \bar{g}, \quad (7)$$

where  $G$  is the shear modulus,  $u$  is the displacement vector,  $v$  is Poisson's ratio,  $F$  are body forces,  $\rho$  is density, and  $g$  is the gravitational constant vector. Given a measured tissue displacement field along with appropriate assumptions, the above equation can be used to reconstruct the spatial distribution of shear modulus (or Young's modulus,  $E = 2G[1+v]$ ).

MRE methods can be broadly classified as either dynamic or static. With dynamic excitation MRE, shear waves are applied to an area of interest by piezoelectric or pneumatic sources; oscillating motion-sensitized gradient sequences are synchronized to the externally-applied excitation, and induced three-dimensional tissue motion is recorded with phase-contrast imaging.<sup>121–124</sup> Static MRE methods<sup>125–128</sup> reconstruct elastic properties of tissue by incorporating a biomechanical finite element model into the nonrigid registration of images acquired under different static loading environments; the application of this technique is not unique to MRI modality, and in fact this methodology is also referred to as modality-independent elastography (MIE)<sup>128</sup> due to its foundation in image processing. All MRE methods require specially designed hardware to couple the deformation source (either static or dynamic) to the area of interest. Challenges to successful application of MRE include

synchronization of the dynamic deformation source to the motion-sensitized MR gradient and often complex biomechanical model-driven inversions of the deformation field to reconstruct tissue elasticity maps. For a more extensive review of MR-based elastography techniques, the interested reader is referred to Mariappan et al<sup>129</sup> and Manduca et al.<sup>130</sup>

### Opportunities and preliminary applications in breast cancer

The rationale for exploring MRE as a possible breast cancer treatment response biomarker derives from observations that cancer progression is accompanied by extracellular matrix remodeling and increasing mechanical stiffness.<sup>89</sup> MRE has been deployed in liver tumor assessment and has had promising preliminary success in distinguishing between benign and malignant lesions, with malignant tumors exhibiting a significant (>3–4 fold) stiffness increase over benign tumors.<sup>131</sup> While there are very few studies of MR-based elastography in breast cancer, preliminary results show initial promise in quantifying in vivo stiffness of breast tumors (as well as differentiation of fibroglandular and adipose tissue)<sup>132</sup> and have demonstrated the ability to improve diagnostic sensitivity and specificity over more traditional breast MRI.<sup>133</sup>

Our group is actively developing MRE as a mechanical property biomarker in breast cancer, and our novel MIE method has been under preliminary investigation in breast cancer.<sup>126,127</sup> Recent breakthroughs involving translation and automation<sup>127</sup> have generated promising preliminary results towards the ability to spatially reconstruct tissue elastic mechanical properties in breast cancer. Figure 8 depicts the results of MIE analysis on a breast cancer patient.

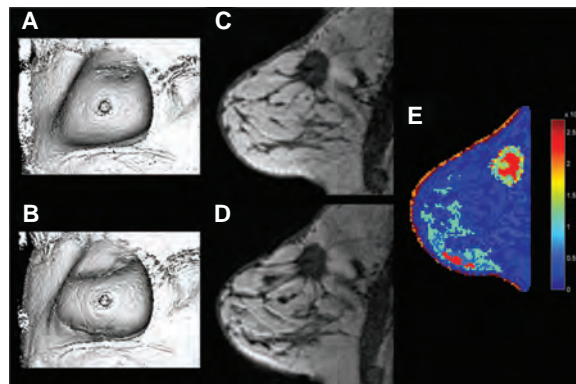


**Figure 8** Static MRE (MIE) results from a breast cancer patient. **(A)** undeformed image volume. **(B)** deformed image volume. **(C)** undeformed central slice. **(D)** deformed central slice. **(E)** reconstructed tissue elasticity map.

**Abbreviations:** MRE, magnetic resonance elastography; MIE, modality-independent elastography.

Monitoring the changes in mechanical properties along the NAT time course may provide a means of assessing response to therapy. Additionally, quantitative mechanical property information can also be used to inform patient-specific reaction-diffusion tumor growth models that are mechanically coupled to constrained tumor cell diffusion.<sup>134</sup> The growth and tumor cell diffusion parameters within the tumor growth models can be fit between the initial and intermediate time points and then projected forward to the final time point in order to help predict patient response.<sup>135,136</sup>

## Hyperpolarized MR

### Theory

Hyperpolarized MR seeks to overcome the limitations of conventional MRS by exploiting exogenous contrast agents that have been “hyperpolarized,” ie, a large proportion of their nuclear spins have been aligned with the magnetic field or polarized. Whereas conventional MR imaging depends on spins that have been polarized on the order of a few parts per million, hyperpolarization allows for polarizing nuclear spins to nearly unity. The resulting several-orders-of-magnitude increase in signal intensity translates into increased sensitivity for detecting metabolic markers of cancer such as lactate and bicarbonate that may be present at millimolar and potentially submillimolar concentrations<sup>137,138</sup> and that may not be amenable to conventional MRS.<sup>137,139</sup> The technique may also be exploited to provide better spatial resolution and significantly faster examination times compared with conventional proton MRS. Long-lived nuclear spin sites are typically selected for the preparation of hyperpolarized contrast agents that are suitable for injection into living organisms. Carbon-13 (<sup>13</sup>C) sites without directly-attached protons are most commonly used, due to their long  $T_1$  of ~20–40 seconds and their abundance within many metabolically-relevant molecules. At present, clinical translation of hyperpolarized MR technology is limited by demanding instrumentation and software requirements, including multinuclear MRI scanner capability, highly specialized RF pulse sequences (tailored to the RF coil, magnetic field strength, and metabolic contrast agent), and multinuclear RF coils.

### Opportunities and preliminary applications in breast cancer

While *in vivo* hyperpolarized MR technology is less than 10 years old, it has rapidly progressed from proof-of-principle studies in mice to the first clinical trial in humans, including analyses of choline, pyruvate, fumarate, and bicarbonate as potential biomarkers.<sup>137,140–143</sup> There have been as yet no

specific clinical applications to breast cancer, but preliminary biomarker studies in mice and in human prostate cancer suggest this technique may be applicable for breast cancer NAT response assessment in the future.<sup>143</sup>

## Challenges and opportunities for clinical translation

Several important challenges must be addressed in working toward the translation and adoption of quantitative MRI techniques. First, investigators will have to choose meaningful and clinically relevant statistical methods for validating novel MRI methods. Prior studies of MRI as a response assessment tool for NAT in breast cancer have chosen a variety of clinical outcome variables – including palpation, imaging-based size measurement change, and pathologic response – against which to evaluate imaging as a response biomarker. Pathologic response is the most clinically relevant of these outcome variables, having been established as an independent prognostic marker for overall survival in breast cancer,<sup>3</sup> yet researchers attempting to validate their methods against pathologic response will have to contend with the multiple different definitions of pathologic response now circulating in the breast cancer literature as well as the notion raised in certain recent studies that pathologic response may be a suitable surrogate endpoint for some but not all breast cancer subtypes.<sup>144</sup> Widespread incorporation of quantitative MRI response biomarkers in the clinical and research settings will probably require validation not just as predictors of pathologic response, but as predictors of long-term outcomes including recurrence rates and overall survival.

A second challenge involves ensuring standardization and reproducibility of MRI methods. MR imaging is a complex undertaking, with images and quantitative measurements dependent upon multiple precise software settings and hardware configurations. Results of a controlled experiment on a single scanner in a laboratory environment may be quite difficult to reproduce across multiple imaging sites. Researchers will have to work with vendors to increase reproducibility across platforms, and vendors will likely be called upon to provide increased transparency with regard to proprietary hardware and software architectures. A handful of government-industry consortia including the Radiological Society of North America’s Quantitative Imaging Biomarkers Alliance are attempting to facilitate these developments. We may also see continued incorporation of quantitative MRI techniques into commercially available computer-assisted detection software.

A third challenge for clinical translation lies in designing MR imaging protocols to meet the various objectives of a clinical scan. As mentioned earlier, there are two chief

goals for breast imaging during NAT – response assessment and demonstration of residual disease – and these goals may call for different MRI approaches that may be mutually exclusive. For example, basic MRI principles dictate a fundamental tradeoff between spatial and temporal resolution—in general, high spatial resolution images require longer acquisition times and therefore a necessary sacrifice of temporal resolution, and high temporal resolution images, by virtue of the rapidity with which they are acquired, do not provide sufficient time to gather high spatial resolution data. A scan tailored for demonstration of residual disease may call for high spatial resolution imaging, while a DCE-MRI scan tailored for early response assessment may call for high temporal resolution imaging in order to provide the most accurate model of vascular flow. These tradeoffs highlight the challenges in clinical MRI protocol design, where different clinical objectives sometimes compete with each other. Potential solutions may emerge from creating hybrid protocols incorporating a variety of imaging techniques; from exploring newer methods, such as compressed sensing, that may make the above tradeoffs less apparent; and/or from employing different scanning protocols for different settings such as, a high temporal resolution MRI protocol early in the course of therapy and a high spatial resolution protocol at the end of therapy as an adjunct to surgical planning.

Finally, investigators across multiple disciplines will have to work toward overcoming the challenge of information saturation that clinicians will inevitably face as the methods discussed in this article are translated into the clinical setting. As more quantitative MRI metrics are validated as useful biomarkers, we may see development of integrated clinical scoring systems that synthesize multiparametric imaging variables with other quantitative clinical parameters.

## Conclusion

There is growing demand for objective and standardized early-response biomarkers for breast cancer NAT, with such biomarkers to be used as an adjunct to and possibly eventually a replacement for pathologic assessment of treatment response. The imaging research community is responding to this demand by developing and testing novel approaches in preclinical models, in single site studies, and in large multisite clinical trials. Quantitative MRI techniques, including the current and emerging methods reviewed in this contribution, hold great potential for incorporation into both clinical and research algorithms. As these techniques are validated

and correlated with long-term clinical outcomes, we may witness a broad transformation in the use of imaging with breast cancer NAT.

## Acknowledgments

We thank the National Institutes of Health (NIH) for funding through NCI 1R01CA129961, NCI 1U01CA142565, R25CA092043, NCI 1P50 CA098131, NCI 5R00 CA134749-03, NCI P30 CA68485, and NCRR/NIH UL1 RR024975-01 (Vanderbilt CTSA grant). We thank the US Department of Defense for funding through BC112431. We would like to acknowledge the Pilot Award Program associated with the Vanderbilt Initiative in Surgery and Engineering (ViSE) center for their support in elastography. We also thank the Kleberg Foundation for generous support of the molecular imaging program at our Institution.

## Disclosure

The authors report no conflicts of interest in this work.

## References

1. Liu SV, Melstrom L, Yao K, Russell CA, Sener SF. Neoadjuvant therapy for breast cancer. *J Surg Oncol.* 2010;101(4):283–291.
2. A phase II neo-adjuvant study of cisplatin, paclitaxel with or without RAD001 in patients with triple-negative locally advanced breast cancer. NCT00930930. Available from: from [http://www.asco.org/ASCOv2/Meetings/Abstracts/?&vmview=abst\\_detail\\_view&confID=74&abstractID=47851](http://www.asco.org/ASCOv2/Meetings/Abstracts/?&vmview=abst_detail_view&confID=74&abstractID=47851). Accessed July 7, 2012.
3. Wolff AC, Berry D, Carey LA, et al. Research issues affecting pre-operative systemic therapy for operable breast cancer. *J Clin Oncol.* 2008;26(5):806–813.
4. Partridge SC, Gibbs JE, Lu Y, Esserman LJ, Sudilovsky D, Hylton NM. Accuracy of MR imaging for revealing residual breast cancer in patients who have undergone neoadjuvant chemotherapy. *AJR Am J Roentgenol.* 2002;179(5):1193–1199.
5. Yeh E, Slanetz P, Kopans DB, et al. Prospective comparison of mammography, sonography, and MRI in patients undergoing neoadjuvant chemotherapy for palpable breast cancer. *AJR Am J Roentgenol.* 2005;184(3):868–877.
6. Abramson RG, Su PF, Shyr Y. Quantitative metrics in clinical radiology reporting: a snapshot perspective from a single mixed academic-community practice. *Magn Reson Imaging.* 2012. Epub July 11.
7. Yankelev TE, Pickens DR, Price RR, editors. *Quantitative MRI in Cancer*: CRC Press, an imprint of Taylor & Francis Group, Boca Raton, Florida, USA. 2011.
8. Eisenhauer EA, Therasse P, Bogaerts J, et al. New response evaluation criteria in solid tumours: revised RECIST guideline (version 1.1). *Eur J Cancer.* 2009;45(2):228–247.
9. Ratain MJ, Eckhardt SG. Phase II studies of modern drugs directed against new targets: if you are fazed, too, then resist RECIST. *J Clin Oncol.* 2004;22(22):4442–4445.
10. Tuma RS. Sometimes size doesn't matter: reevaluating RECIST and tumor response rate endpoints. *J Natl Cancer Inst.* 2006;98(18): 1272–1274.
11. Kuhl CK. Current status of breast MR imaging. Part 2. Clinical applications. *Radiology.* 2007;244(3):672–691.
12. Houssami N, Hayes DF. Review of preoperative magnetic resonance imaging (MRI) in breast cancer: should MRI be performed on all women with newly diagnosed, early stage breast cancer? *CA Cancer J Clin.* 2009;59(5):290–302.

13. Pediconi F, Miglio E, Telesca M, et al. Effect of preoperative breast magnetic resonance imaging on surgical decision making and cancer recurrence rates. *Invest Radiol.* 2012;47(2):128–135.
14. Pettit K, Swatske ME, Gao F, et al. The impact of breast MRI on surgical decision-making: are patients at risk for mastectomy? *J Surg Oncol.* 2009;100(7):553–558.
15. Kuhl C. The current status of breast MR imaging. Part I. Choice of technique, image interpretation, diagnostic accuracy, and transfer to clinical practice. *Radiology.* 2007;244(2):356–378.
16. Chou CP, Wu MT, Chang HT, et al. Monitoring breast cancer response to neoadjuvant systemic chemotherapy using parametric contrast-enhanced MRI: a pilot study. *Acad Rad.* 2007;14(5):561–573.
17. Delille JP, Slanetz PJ, Yeh ED, Halpern EF, Kopans DB, Garrido L. Invasive ductal breast carcinoma response to neoadjuvant chemotherapy: noninvasive monitoring with functional MR imaging pilot study. *Radiology.* 2003;228(1):63–69.
18. Drew PJ, Kerin MJ, Mahapatra T, et al. Evaluation of response to neoadjuvant chemoradiotherapy for locally advanced breast cancer with dynamic contrast-enhanced MRI of the breast. *Eur J Surg Oncol.* 2001;27(7):617–620.
19. Abraham DC, Jones RC, Jones SE, et al. Evaluation of neoadjuvant chemotherapeutic response of locally advanced breast cancer by magnetic resonance imaging. *Cancer.* 1996;78(1):91–100.
20. Rieber A, Brambs HJ, Gabelmann A, Heilmann V, Kreienberg R, Kühn T. Breast MRI for monitoring response of primary breast cancer to neo-adjuvant chemotherapy. *Eur Radiol.* 2002;12(7):1711–1719.
21. Gilles R, Guinebretière JM, Toussaint C, et al. Locally advanced breast cancer: contrast-enhanced subtraction MR imaging of response to preoperative chemotherapy. *Radiology.* 1994;191(3):633–638.
22. Londero V, Bazzocchi M, Del Frate C, et al. Locally advanced breast cancer: comparison of mammography, sonography and MR imaging in evaluation of residual disease in women receiving neoadjuvant chemotherapy. *Eur Radiol.* 2004;14(8):1371–1379.
23. Balu-Maestro C, Chapellier C, Bleuse A, Chanalet I, Chauvel C, Largillier R. Imaging in evaluation of response to neoadjuvant breast cancer treatment benefits of MRI. *Breast Cancer Res Treat.* 2002;72(2):145–152.
24. Cheung YC, Chen SC, Su MY, et al. Monitoring the size and response of locally advanced breast cancers to neoadjuvant chemotherapy (weekly paclitaxel and epirubicin) with serial enhanced MRI. *Breast Cancer Res Treat.* 2003;78(1):51–58.
25. Martincich L, Montemurro F, De Rosa G, et al. Monitoring response to primary chemotherapy in breast cancer using dynamic contrast-enhanced magnetic resonance imaging. *Breast Cancer Res Treat.* 2004;83(1):67–76.
26. Wasser K, Klein SK, Fink C, et al. Evaluation of neoadjuvant chemotherapeutic response of breast cancer using dynamic MRI with high temporal resolution. *Eur Radiol.* 2003;13(1):80–87.
27. Padhani AR, Hayes C, Assersohn L, et al. Prediction of clinicopathologic response of breast cancer to primary chemotherapy at contrast-enhanced MR imaging: initial clinical results. *Radiology.* 2006;239(2):361–374.
28. Loo CE, Teerstra HJ, Rodenhuis S, et al. Dynamic contrast-enhanced MRI for prediction of breast cancer response to neoadjuvant chemotherapy: initial results. *AJR Am J Roentgenol.* 2008;191(5):1331–1338.
29. Hylton NM, Blume JD, Bernreuter WK, et al. Locally advanced breast cancer: MR imaging for prediction of response to neoadjuvant chemotherapy – results from ACRIN 6657/I-SPY TRIAL. *Radiology.* 2012;263(3):663–672.
30. Partridge SC, Gibbs JE, Lu Y, et al. MRI measurements of breast tumor volume predict response to neoadjuvant chemotherapy and recurrence-free survival. *AJR Am J Roentgenol.* 2005;184(6):1774–1781.
31. Yankelev TE, Gore JC. Dynamic contrast enhanced magnetic resonance imaging in oncology: theory, data acquisition, analysis, and examples. *Curr Med Imaging Rev.* 2009;3(2):91–107.
32. Arasu VA, Chen RC, Newitt DN, et al. Can signal enhancement ratio (SER) reduce the number of recommended biopsies without affecting cancer yield in occult MRI-detected lesions? *Acad Radiol.* 2011;18(6):716–721.
33. Miller KD, Trigo JM, Wheeler C, et al. A multicenter phase II trial of ZD6474, a vascular endothelial growth factor receptor-2 and epidermal growth factor receptor tyrosine kinase inhibitor, in patients with previously treated metastatic breast cancer. *Clin Cancer Res.* 2005;11(9):3369–3376.
34. Evelhoch JL, LoRusso PM, He Z, et al. Magnetic resonance imaging measurements of the response of murine and human tumors to the vascular-targeting agent ZD6126. *Clin Cancer Res.* 2004;10(11):3650–3657.
35. Morgan B, Thomas AL, Dreys J, et al. Dynamic contrast-enhanced magnetic resonance imaging as a biomarker for the pharmacological response of PTK787/ZK 222584, an inhibitor of the vascular endothelial growth factor receptor tyrosine kinases, in patients with advanced colorectal cancer and liver metastases: results from two phase I studies. *J Clin Oncol.* 2003;21(21):3955–3964.
36. Tateishi U, Miyake M, Nagaoka T, et al. Neoadjuvant chemotherapy in breast cancer: prediction of pathologic response with PET/CT and dynamic contrast-enhanced MR imaging – prospective assessment. *Radiology.* 2012;263(1):53–63.
37. Sourbron SP, Buckley DL. Tracer kinetic modelling in MRI: estimating perfusion and capillary permeability. *Phys Med Biol.* 2012;57(2):R1–R33.
38. Kety SS. The theory and applications of the exchange of inert gas at the lungs and tissues. *Pharmacol Rev.* 1951;3(1):1–41.
39. Yankelev TE, Lepage M, Chakravarthy A, et al. Integration of quantitative DCE-MRI and ADC mapping to monitor treatment response in human breast cancer: initial results. *Magn Reson Imaging.* 2007;25(1):1–13.
40. Ah-See ML, Makris A, Taylor NJ, et al. Early changes in functional dynamic magnetic resonance imaging predict for pathologic response to neoadjuvant chemotherapy in primary breast cancer. *Clin Cancer Res.* 2008;14(20):6580–6589.
41. Pickles MD, Manton DJ, Lowry M, Turnbull LW. Prognostic value of pre-treatment DCE-MRI parameters in predicting disease free and overall survival for breast cancer patients undergoing neoadjuvant chemotherapy. *Eur J Radiol.* 2009;71(3):498–505.
42. Heldahl MG, Bathen TF, Rydland J, et al. Prognostic value of pretreatment dynamic contrast-enhanced MR imaging in breast cancer patients receiving neoadjuvant chemotherapy: overall survival predicted from combined time course and volume analysis. *Acta Radiol.* 2010;51(6):604–612.
43. Johansen R, Jensen LR, Rydland J, et al. Predicting survival and early clinical response to primary chemotherapy for patients with locally advanced breast cancer using DCE-MRI. *J Magn Reson Imaging.* 2009;29(6):1300–1307.
44. Newitt DC, Partridge SC, Chang B, Joe BN, Hylton N. Optimization of the percent enhancement threshold for breast MRI tumor volume measurement during neoadjuvant treatment of breast cancer for predicting recurrence free survival time. *Proc Int Soc Mag Reson Med (ISMRM).* 2011;19:508. Available from: <http://submissions.miracd.com/isrmr2011/proceedings/files/508.pdf>. Accessed June 21, 2012.
45. Li X, Arlinghaus LR, Chakravarthy AB, et al. Towards optimization of DCE-MRI analysis for early prediction of the response of breast cancer patients to neoadjuvant chemotherapy. *Proc Int Soc Mag Reson Med (ISMRM).* 2012;20:1464. Available from: [http://www.google.ca/url?sa=t&rct=j&q=towards%20optimization%20of%20dce-mri%20analysis%20for%20early%20prediction%20of%20the%20response%20of%20breast%20cancer%20patients%20to%20neoadjuvant%20chemotherapy&source=web&cd=2&ved=0CCoQFjAB&url=ftp%3A%2F%2Fftp.cmrr.umn.edu%2Fforum%2Fismrm2012breast%2F1464.pdf&ei=BBBRUMXvHcjYywGoy4HQAw&usg=AFQjCNGYY7-cER4BpjS\\_l25btSw5qx75Fw&cad=rja](http://www.google.ca/url?sa=t&rct=j&q=towards%20optimization%20of%20dce-mri%20analysis%20for%20early%20prediction%20of%20the%20response%20of%20breast%20cancer%20patients%20to%20neoadjuvant%20chemotherapy&source=web&cd=2&ved=0CCoQFjAB&url=ftp%3A%2F%2Fftp.cmrr.umn.edu%2Fforum%2Fismrm2012breast%2F1464.pdf&ei=BBBRUMXvHcjYywGoy4HQAw&usg=AFQjCNGYY7-cER4BpjS_l25btSw5qx75Fw&cad=rja). Accessed September 12, 2012.
46. Le Bihan D, Breton E, Lallemand D, Grenier P, Cabanis E, Laval-Jeantet M. MR imaging of intravoxel incoherent motions: application to diffusion and perfusion in neurologic disorders. *Radiology.* 1986;161(2):401–407.

47. Anderson AW, Xie J, Pizzonia J, Bronen RA, Spencer DD, Gore JC. Effects of cell volume fraction changes on apparent diffusion in human cells. *Magn Reson Imaging*. 2000;18(6):689–695.

48. Hagemann P, Jonasson L, Maeder P, Thiran JP, Wedeen VJ, Meuli R. Understanding diffusion MR imaging techniques: from scalar diffusion-weighted imaging to diffusion tensor imaging and beyond. *Radiographics*. 2006;26 Suppl 1:S205–S223.

49. Charles-Edwards EM, deSouza NM. Diffusion-weighted magnetic resonance imaging and its application to cancer. *Cancer Imaging*. 2006;6:135–143.

50. Li XR, Cheng LQ, Liu M, et al. DW-MRI ADC values can predict treatment response in patients with locally advanced breast cancer undergoing neoadjuvant chemotherapy. *Med Oncol*. 2012;29(2):425–431.

51. Pickles MD, Gibbs P, Lowry M, Turnbull LW. Diffusion changes precede size reduction in neoadjuvant treatment of breast cancer. *Magn Reson Imaging*. 2006;24(7):843–847.

52. Sharma U, Danishad KK, Seenu V, Jagannathan NR. Longitudinal study of the assessment by MRI and diffusion-weighted imaging of tumor response in patients with locally advanced breast cancer undergoing neoadjuvant chemotherapy. *NMR Biomed*. 2009;22(1):104–113.

53. Arlinghaus LR, Yankeelov TE. Diffusion-weighted MRI. In: Yankeelov T, Pickens DR, Price RR, editors. *Quantitative MRI in Cancer*. Boca Raton: CRC Press, an imprint of Taylor & Francis Group, Boca Raton, Florida, USA. 2012:xviii:312.

54. Iacconi C, Giannelli M, Marini C, et al. The role of mean diffusivity (MD) as a predictive index of the response to chemotherapy in locally advanced breast cancer: a preliminary study. *Eur Radiol*. 2010;20(2):303–308.

55. Park SH, Moon WK, Cho N, et al. Diffusion-weighted MR imaging: pretreatment prediction of response to neoadjuvant chemotherapy in patients with breast cancer. *Radiology*. 2010;257(1):56–63.

56. Belli P, Costantini M, Ierardi C, et al. Diffusion-weighted imaging in evaluating the response to neoadjuvant breast cancer treatment. *Breast J*. 2011;17(6):610–619.

57. Fangberget A, Nilsen LB, Hole KH, et al. Neoadjuvant chemotherapy in breast cancer-response evaluation and prediction of response to treatment using dynamic contrast-enhanced and diffusion-weighted MR imaging. *Eur Radiol*. 2011;21(6):1188–1199.

58. Park SH, Moon WK, Cho N, et al. Comparison of diffusion-weighted MR imaging and FDG PET/CT to predict pathological complete response to neoadjuvant chemotherapy in patients with breast cancer. *Eur Radiol*. 2012;22(1):18–25.

59. Shin HJ, Baek HM, Ahn JH, et al. Prediction of pathologic response to neoadjuvant chemotherapy in patients with breast cancer using diffusion-weighted imaging and MRS. *NMR Biomed*. 2012. Epub May 6.

60. Jensen LR, Garzon B, Heldahl MG, Bathen TF, Lundgren S, Gribbestad IS. Diffusion-weighted and dynamic contrast-enhanced MRI in evaluation of early treatment effects during neoadjuvant chemotherapy in breast cancer patients. *J Magn Reson Imaging*. 2011;34(5):1099–1109.

61. Dorrius MD, Pijnappel RM, Jansen-van der Weide MC, et al. Determination of choline concentration in breast lesions: quantitative multivoxel proton MR spectroscopy as a promising noninvasive assessment tool to exclude benign lesions. *Radiology*. 2011;259(3):695–703.

62. Bartella L, Morris EA, Dershaw DD, et al. Proton MR spectroscopy with choline peak as malignancy marker improves positive predictive value for breast cancer diagnosis: preliminary study. *Radiology*. 2006;239(3):686–692.

63. Glunde K, Shah T, Winnard PT Jr, et al. Hypoxia regulates choline kinase expression through hypoxia-inducible factor-1 alpha signaling in a human prostate cancer model. *Cancer Res*. 2008;68(1):172–180.

64. Hanahan D, Weinberg RA. Hallmarks of cancer: the next generation. *Cell*. 2011;144(5):646–674.

65. Bathen TF, Heldahl MG, Sitter B, et al. In vivo MRS of locally advanced breast cancer: characteristics related to negative or positive choline detection and early monitoring of treatment response. *MAGMA*. 2011;24(6):347–357.

66. Jagannathan NR, Kumar M, Seenu V, et al. Evaluation of total choline from in-vivo volume localized proton MR spectroscopy and its response to neoadjuvant chemotherapy in locally advanced breast cancer. *Br J Cancer*. 2001;84(8):1016–1022.

67. Kumar M, Jagannathan NR, Seenu V, Dwivedi SN, Julka PK, Rath GK. Monitoring the therapeutic response of locally advanced breast cancer patients: sequential in vivo proton MR spectroscopy study. *J Magn Reson Imaging*. 2006;24(2):325–332.

68. Manton DJ, Chaturvedi A, Hubbard A, et al. Neoadjuvant chemotherapy in breast cancer: early response prediction with quantitative MR imaging and spectroscopy. *Br J Cancer*. 2006;94(3):427–435.

69. Murata Y, Hamada N, Kubota K, et al. Choline by magnetic spectroscopy and dynamic contrast enhancement curve by magnetic resonance imaging in neoadjuvant chemotherapy for invasive breast cancer. *Mol Med Report*. 2009;2(1):39–43.

70. Sijens PE, Dorrius MD, Kappert P, Baron P, Pijnappel RM, Oudkerk M. Quantitative multivoxel proton chemical shift imaging of the breast. *Magn Reson Imaging*. 2010;28(3):314–319.

71. Tozaki M, Sakamoto M, Oyama Y, Maruyama K, Fukuma E. Predicting pathological response to neoadjuvant chemotherapy in breast cancer with quantitative <sup>1</sup>H MR spectroscopy using the external standard method. *J Magn Reson Imaging*. 2010;31(4):895–902.

72. Meisamy S, Bolan PJ, Baker EH, et al. Neoadjuvant chemotherapy of locally advanced breast cancer: predicting response with in vivo (<sup>1</sup>H) MR spectroscopy – a pilot study at 4 T. *Radiology*. 2004;233(2): 424–431.

73. Danishad KK, Sharma U, Sah RG, Seenu V, Parshad R, Jagannathan NR. Assessment of therapeutic response of locally advanced breast cancer (LABC) patients undergoing neoadjuvant chemotherapy (NACT) monitored using sequential magnetic resonance spectroscopic imaging (MRSI). *NMR Biomed*. 2010;23(3):233–241.

74. Hu J, Yu Y, Kou Z, et al. A high spatial resolution <sup>1</sup>H magnetic resonance spectroscopic imaging technique for breast cancer with a short echo time. *Magn Reson Imaging*. 2008;26(3):360–366.

75. Wolff SD, Balaban RS. Magnetization transfer contrast (MTC) and tissue water proton relaxation in vivo. *Magn Reson Med*. 1989;10(1): 135–144.

76. Odrobina EE, Lam TYJ, Pun T, Midha R, Stanisz GJ. MR properties of excised neural tissue following experimentally induced demyelination. *NMR Biomed*. 2005;18(5):277–284.

77. Henkelman RM, Huang X, Xiang QS, Stanisz GJ, Swanson SD, Bronskill MJ. Quantitative interpretation of magnetization-transfer. *Magn Reson Med*. 1993;29(6):759–766.

78. Sled JG, Pike GB. Quantitative imaging of magnetization transfer exchange and relaxation properties in vivo using MRI. *Magn Reson Med*. 2001;46(5):923–931.

79. Dortsch RD, Li K, Gochberg DF, et al. Quantitative magnetization transfer imaging in human brain at 3 T via selective inversion recovery. *Magn Reson Med*. 2011;66(5):1346–1352.

80. Gochberg DF, Lepage M. Magnetization transfer and chemical exchange saturation transfer imaging in cancer imaging. In: Yankeelov TE, Pickens DR, Price RR, editors. *Quantitative MRI of Cancer*. New York, NY: CRC Press, an imprint of Taylor & Francis Group, Boca Raton, Florida, USA. 2012:99–106.

81. Filippi M, Agosta F. Magnetization transfer MRI in multiple sclerosis. *J Neuroimaging*. 2007;17 Suppl 1:S22–S26.

82. Filippi M, Rocca MA. Magnetization transfer magnetic resonance imaging in the assessment of neurological diseases. *J Neuroimaging*. 2004;14(4):303–313.

83. Ropele S, Fazekas F. Magnetization transfer MR imaging in multiple sclerosis. *Neuroimaging Clin N Am*. 2009;19(1):27–36.

84. Lundbom N. Determination of magnetization transfer contrast in tissue: an MR imaging study of brain tumors. *AJR. Am J Roentgenol*. 1992; 159(6):1279–1285.

85. Hanahan D, Weinberg RA. The hallmarks of cancer. *Cell*. 2000;100(1): 57–70.

86. Nelson CM, Bissell MJ. Of extracellular matrix, scaffolds, and signaling: tissue architecture regulates development, homeostasis, and cancer. *Annu Rev Cell Dev Biol*. 2006;22:287–309.

87. Stetler-Stevenson WG, Aznavoorian S, Liotta LA. Tumor cell interactions with the extracellular-matrix during invasion and metastasis. *Annu Rev Cell Biol.* 1993;9:541–573.

88. Ioachim E, Charchanti A, Briassoulis E, et al. Immunohistochemical expression of extracellular matrix components tenascin, fibronectin, collagen type IV and laminin in breast cancer: their prognostic value and role in tumour invasion and progression. *Eur J Cancer.* 2002; 38(18):2362–2370.

89. Levental KR, Yu H, Kass L, et al. Matrix crosslinking forces tumor progression by enhancing integrin signaling. *Cell.* 2009;139(5): 891–906.

90. Kakkad SM, Solaiyappan M, O'Rourke B, et al. Hypoxic tumor microenvironments reduce collagen I fiber density. *Neoplasia.* 2010;12(8):608–617.

91. Bonini RH, Zeotti D, Saraiva LA, et al. Magnetization transfer ratio as a predictor of malignancy in breast lesions: preliminary results. *Magn Reson Med.* 2008;59(5):1030–1034.

92. Rajan R, Esteva FJ, Symmans WF. Pathologic changes in breast cancer following neoadjuvant chemotherapy: implications for the assessment of response. *Clin Breast Cancer.* 2004;5(3):235–238.

93. Sahoo S, Lester SC. Pathology of breast carcinomas after neoadjuvant chemotherapy: an overview with recommendations on specimen processing and reporting. *Arch Pathol Lab Med.* 2009;133(4):633–642.

94. Sneige N, Kemp B, Pusztai L, Asmar L, Hortobagyi GN. Chemotherapy-induced histologic changes in mastectomy specimens and their potential significance. *Breast.* 2001;10(6):492–500.

95. Zhou J, Payen JF, Wilson DA, Traystman RJ, van Zijl PC. Using the amide proton signals of intracellular proteins and peptides to detect pH effects in MRI. *Nat Med.* 2003;9(8):1085–1090.

96. Jin T, Wang P, Zong X, Kim SG. Magnetic resonance imaging of the Amine-Proton EXchange (APEX) dependent contrast. *Neuroimage.* 2012;59(2):1218–1227.

97. van Zijl PC, Jones CK, Ren J, Malloy CR, Sherry AD. MRI detection of glycogen in vivo by using chemical exchange saturation transfer imaging (glycoCEST). *Proc Natl Acad Sci U S A.* 2007;104(11): 4359–4364.

98. van Zijl PC, Zhou J, Mori N, Payen JF, Wilson D, Mori S. Mechanism of magnetization transfer during on-resonance water saturation. A new approach to detect mobile proteins, peptides, and lipids. *Magn Reson Med.* 2003;49(3):440–449.

99. Wolff SD, Balaban RS. NMR imaging of labile proton-exchange. *J Magn Reson.* 1990;86(1):164–169.

100. Ward KM, Aletras AH, Balaban RS. A new class of contrast agents for MRI based on proton chemical exchange dependent saturation transfer (CEST). *J Magn Reson.* 2000;143(1):79–87.

101. Bryant RG. The dynamics of water-protein interactions. *Annu Rev Biophys Biomol Struct.* 1996;25:29–53.

102. Smith SA, Bulte JW, van Zijl PC. Direct saturation MRI: theory and application to imaging brain iron. *Magn Reson Med.* 2009;62(2): 384–393.

103. Scheidegger R, Vinogradov E, Alsop DC. Amide proton transfer imaging with improved robustness to magnetic field inhomogeneity and magnetization transfer asymmetry using saturation with frequency alternating RF irradiation. *Magn Reson Med.* 2011;66(5):1275–1285.

104. Zaiss M, Schmitt B, Bachert P. Quantitative separation of CEST effect from magnetization transfer and spillover effects by Lorentzian-line-fit analysis of z-spectra. *J Magn Reson.* 2011;211(2):149–155.

105. Desmond KL, Stanisz GJ. Understanding quantitative pulsed CEST in the presence of MT. *Magn Reson Med.* 2012;67(4):979–990.

106. Dula AN, Arlinghaus LR, Dortch RD, et al. Repeatability of chemical exchange saturation transfer measurements in healthy fibroglandular breast tissue at 3 T. *Proc Intl Soc Mag Reson Med (ISMRM).* 2012;20:3376. Available from: <http://www.google.ca/url?sa=t&rct=j&q=repeatability%20of%20chemical%20exchange%20saturation%20transfer%20measurements%20in%20healthy%20fibroglandular%20breast%20tissue%20at%203t&sourc e=web&cd=1&ved=0CCMQFjAA&url=ftp%3A%2F%2Fftp.cmrr.umn.edu%2Fcorum%2Fisrmr2012breast%2F3376.pdf&ei=CyFRUNz2AsPlyAHegIHICA&usg=AFQjCNHcPUngall2lf7lxHceT-Ueghd6sQ&cad=rja>. Accessed September 12, 2012.

107. Jones CK, Polders D, Hua J, et al. In vivo three-dimensional whole-brain pulsed steady-state chemical exchange saturation transfer at 7T. *Magn Reson Med.* 2012;67(6):1579–1589.

108. Hua J, Jones CK, Blakeley J, Smith SA, van Zijl PC, Zhou J. Quantitative description of the asymmetry in magnetization transfer effects around the water resonance in the human brain. *Magn Reson Med.* 2007;58(4):786–793.

109. Jokivarsi KT, Gröhn HI, Gröhn OH, Kauppinen RA. Proton transfer ratio, lactate, and intracellular pH in acute cerebral ischemia. *Magn Reson Med.* 2007;57(4):647–653.

110. Jones CK, Schlosser MJ, van Zijl PC, Pomper MG, Golay X, Zhou J. Amide proton transfer imaging of human brain tumors at 3 T. *Magn Reson Med.* 2006;56(3):585–592.

111. Sun PZ, Murata Y, Lu J, Wang X, Lo EH, Sorensen AG. Relaxation-compensated fast multislice amide proton transfer (APT) imaging of acute ischemic stroke. *Magn Reson Med.* 2008;59(5): 1175–1182.

112. Salhotra A, Lal B, Laterra J, Sun PZ, van Zijl PC, Zhou J. Amide proton transfer imaging of 9L gliosarcoma and human glioblastoma xenografts. *NMR Biomed.* 2008;21(5):489–497.

113. Jia G, Abaza R, Williams JD, et al. Amide proton transfer MR imaging of prostate cancer: a preliminary study. *J Magn Reson Imaging.* 2011;33(3):647–654.

114. Zhou J, Lal B, Wilson DA, Laterra J, van Zijl PC. Amide proton transfer (APT) contrast for imaging of brain tumors. *Magn Reson Med.* 2003;50(6):1120–1126.

115. Dula AN, Arlinghaus LR, Dortch RD, et al. Amide proton transfer imaging of the breast at 3T: establishing reproducibility and possible feasibility assessing chemotherapy response. *Magn Reson Med.* 2012. [Epub ahead of print]

116. Delehedde M, Lyon M, Sergeant N, Rahmoune H, Fernig DG. Proteoglycans: pericellular and cell surface multireceptors that integrate external stimuli in the mammary gland. *J Mammary Gland Biol Neoplasia.* 2001;6(3):253–273.

117. Baba F, Swartz K, van Buren R, et al. Syndecan-1 and syndecan-4 are overexpressed in an estrogen receptor-negative, highly proliferative breast carcinoma subtype. *Breast Cancer Res Treat.* 2006;98(1):91–98.

118. Maeda T, Alexander CM, Friedl A. Induction of syndecan-1 expression in stromal fibroblasts promotes proliferation of human breast cancer cells. *Cancer Res.* 2004;64(2):612–621.

119. Barbareschi M, Maisonneuve P, Aldovini D, et al. High syndecan-1 expression in breast carcinoma is related to an aggressive phenotype and to poorer prognosis. *Cancer.* 2003;98(3):474–483.

120. Ophir J, Céspedes I, Ponnekanti H, Yazdi Y, Li X. Elastography: a quantitative method for imaging the elasticity of biological tissues. *Ultrason Imaging.* 1991;13(2):111–134.

121. Muthupillai R, Lomas DJ, Rossman PJ, Greenleaf JF, Manduca A, Ehman RL. Magnetic-resonance elastography by direct visualization of propagating acoustic strain waves. *Science.* 1995;269(5232): 1854–1857.

122. Sack I, McGowan CK, Samani A, Luginbuhl C, Oakden W, Plewes DB. Observation of nonlinear shear wave propagation using magnetic resonance elastography. *Magn Reson Med.* 2004;52(4): 842–850.

123. Sinkus R, Tanter M, Catheline S, et al. Imaging anisotropic and viscous properties of breast tissue by magnetic resonance-elastography. *Magn Reson Med.* 2005;53(2):372–387.

124. Van Houten EE, Paulsen KD, Miga MI, Kennedy FE, Weaver JB. An overlapping subzone technique for MR-based elastic property reconstruction. *Magn Reson Med.* 1999;42(4):779–786.

125. Miga MI, Rothney MP, Ou JJ. Modality independent elastography (MIE): potential applications in dermoscopy. *Med Phys.* 2005;32(5):1308–1320.

126. Ou JJ, Ong RE, Yankeelov TE, Miga MI. Evaluation of 3D modality-independent elastography for breast imaging: a simulation study. *Phys Med Biol.* 2008;53(1):147–163.

127. Pheiffer TS, Ou JJ, Ong RE, Miga MI. Automatic generation of boundary conditions using demons nonrigid image registration for use in 3-D modality-independent elastography. *IEEE Trans Biomed Eng.* 2011;58(9):2607–2616.

128. Miga MI. A new approach to elastography using mutual information and finite elements. *Phys Med Biol.* 2003;48(4):467–480.

129. Mariappan YK, Glaser KJ, Ehman RL. Magnetic resonance elastography: a review. *Clin Anat.* 2010;23(5):497–511.

130. Manduca A, Oliphant TE, Dresner MA, et al. Magnetic resonance elastography: non-invasive mapping of tissue elasticity. *Med Image Anal.* 2001;5(4):237–254.

131. Venkatesh SK, Yin M, Glockner JF, et al. MR elastography of liver tumors: preliminary results. *AJR Am J Roentgenol.* 2008;190(6):1534–1540.

132. McKnight AL, Kugel JL, Rossman PJ, Manduca A, Hartmann LC, Ehman RL. MR elastography of breast cancer: preliminary results. *AJR Am J Roentgenol.* 2002;178(6):1411–1417.

133. Siegmann KC, Xydeas T, Sinkus R, Kraemer B, Vogel U, Claussen CD. Diagnostic value of MR elastography in addition to contrast-enhanced MR imaging of the breast—initial clinical results. *Eur Radiol.* 2010;20(2):318–325.

134. Garg I, Miga MI. Preliminary investigation of the inhibitory effects of mechanical stress in tumor growth. *SPIE Medical Imaging 2008: Visualization, Image-Guided Procedures, and Modeling Conference.* 2008;6918. Available from: [http://spie.org/x648.html?product\\_id=773376](http://spie.org/x648.html?product_id=773376). Accessed September 12, 2012.

135. Atuegwu NC, Arlinghaus LR, Li X, et al. Integration of diffusion-weighted MRI data and a simple mathematical model to predict breast tumor cellularity during neoadjuvant chemotherapy. *Magn Reson Med.* 2011;66(6):1689–1696.

136. Atuegwu NC, Colvin DC, Loveless ME, Xu L, Gore JC, Yankeelov TE. Incorporation of diffusion-weighted magnetic resonance imaging data into a simple mathematical model of tumor growth. *Phys Med Biol.* 2012;57(1):225–240.

137. Day SE, Kettunen MI, Gallagher FA, et al. Detecting tumor response to treatment using hyperpolarized 13C magnetic resonance imaging and spectroscopy. *Nat Med.* 2007;13(11):1382–1387.

138. Park I, Bok R, Ozawa T, et al. Detection of early response to temozolamide treatment in brain tumors using hyperpolarized 13C MR metabolic imaging. *J Magn Reson Imaging.* 2011;33(6):1284–1290.

139. Gallagher FA, Kettunen MI, Day SE, et al. Magnetic resonance imaging of pH in vivo using hyperpolarized 13C-labelled bicarbonate. *Nature.* 2008;453(7197):940–943.

140. Cudalbu C, Comment A, Kurdzesau F, et al. Feasibility of in vivo 15N MRS detection of hyperpolarized 15N labeled choline in rats. *Phys Chem Chem Phys.* 2010;12(22):5818–5823.

141. Gabellieri C, Reynolds S, Lavie A, Payne GS, Leach MO, Eykyn TR. Therapeutic target metabolism observed using hyperpolarized 15N choline. *J Am Chem Soc.* 2008;130(14):4598–4599.

142. Gallagher FA, Kettunen MI, Hu DE, et al. Production of hyperpolarized [1,4-13C2]malate from [1,4-C-13(2)]fumarate is a marker of cell necrosis and treatment response in tumors. *Proc Natl Acad Sci U S A.* 2009;106(47):19801–19806.

143. Kurhanewicz J, Vigneron DB, Brindle K, et al. Analysis of cancer metabolism by imaging hyperpolarized nuclei: prospects for translation to clinical research. *Neoplasia.* 2011;13(2):81–97.

144. von Minckwitz G, Untch M, Blohmer JU, et al. Definition and impact of pathologic complete response on prognosis after neoadjuvant chemotherapy in various intrinsic breast cancer subtypes. *J Clin Oncol.* 2012;30(15):1796–1804.

## Breast Cancer: Targets and Therapy

**Publish your work in this journal**

Breast Cancer: Targets and Therapy is an international, peer-reviewed open access journal focusing on breast cancer research, identification of therapeutic targets and the optimal use of preventative and integrated treatment interventions to achieve improved outcomes, enhanced survival and quality of life for the cancer patient.

Submit your manuscript here: <http://www.dovepress.com/breast-cancer---targets-and-therapy-journal>

Dovepress

View the full aims and scopes of this journal here. The manuscript management system is completely online and includes a very quick and fair peer-review system, which is all easy to use. Visit <http://www.dovepress.com/testimonials.php> to read real quotes from published authors.

# Near-unity nuclear polarization with an ‘open-source’ <sup>129</sup>Xe hyperpolarizer for NMR and MRI

Panayiotis Nikolaou<sup>a,b</sup>, Aaron Coffey<sup>a,i</sup>, Laura L. Walkup<sup>b</sup>, Brogan Gust<sup>b</sup>, Nicholas Whiting<sup>c,\*</sup>, Hayley Newton<sup>c</sup>, Scott Barcus<sup>b,d</sup>, Iga Muradyan<sup>e</sup>, Mikayel Dabaghyan<sup>e</sup>, Gregory D. Moroz<sup>f</sup>, Matthew Rosen<sup>g,h</sup>, Samuel Patz<sup>e</sup>, Michael J. Barlow<sup>c</sup>, Eduard Chekmenev<sup>a,i,j</sup>, and Boyd M. Goodson<sup>b†</sup>

<sup>a</sup>Department of Radiology, Vanderbilt University Institute of Imaging Science (VUINS), Nashville, TN, 37232, United States; <sup>b</sup>Department of Chemistry & Biochemistry, Southern Illinois University, Carbondale, IL; <sup>c</sup>Sir Peter Mansfield Magnetic Resonance Centre, University of Nottingham, Nottingham, NG7 2RD, UK; <sup>d</sup>REU student; home institution: Department of Physics, Drake University, Des Moines, IA; <sup>e</sup>Brigham & Women’s Hospital and Harvard Medical School, Boston, MA; <sup>f</sup>Graduate School Central Research Shop, Southern Illinois University, Carbondale, IL; <sup>g</sup>Department of Physics, Harvard University, Cambridge MA; <sup>h</sup>MGH/A.A. Martinos Center for Biomedical Imaging, Boston MA; <sup>i</sup>Department of Biomedical Engineering, Vanderbilt University, Nashville, Tennessee, 37235, United States; <sup>j</sup>Department of Biochemistry, Vanderbilt University, Nashville, Tennessee, 37205, United States \*Present address: MD Anderson Cancer Center, Houston, TX Corresponding Author: Boyd M. Goodson, Department of Chemistry & Biochemistry, Southern Illinois University, Carbondale, IL. Phone: 618-453-6427; Fax: 618-453-6408; E-mail: bgoodson@chem.siu.edu

Submitted to Proceedings of the National Academy of Sciences of the United States of America

The exquisite NMR spectral sensitivity and negligible reactivity of hyperpolarized xenon-129 (HP<sup>129</sup>Xe) make it attractive for a number of magnetic resonance applications; moreover, HP<sup>129</sup>Xe embodies an alternative to rare and non-renewable <sup>3</sup>He. However, the ability to reliably and inexpensively produce large quantities of HP<sup>129</sup>Xe with sufficiently high <sup>129</sup>Xe nuclear spin polarization ( $P_{Xe}$ ) remains a significant challenge—particularly at high Xe densities. We present results from our ‘open-source’ large-scale (~1 L/hr) <sup>129</sup>Xe polarizer for clinical, pre-clinical, and materials NMR and MRI research. Automated and comprised mostly of off-the-shelf components, this ‘hyperpolarizer’ is designed to be readily implementable in other laboratories. The device runs with high resonant photon flux (up to 200 W at the Rb D<sub>1</sub> line) in the xenon-rich regime (up to 1800 Torr Xe in 500 cc) in either single-batch or stopped-flow mode, negating in part the usual requirement of Xe cryo-collection. Excellent agreement is observed among four independent methods utilized to measure spin polarization. In-cell  $P_{Xe}$  values of ~90%, ~57%, ~50%, and ~30% have been measured for Xe loadings of ~300, ~500, ~760, and ~1570 Torr, respectively.  $P_{Xe}$  values of ~41% and ~28% (with ~760 and ~1545 Torr Xe loadings) have been measured after transfer to Tedlar bags and transport to a clinical 3 T scanner for MR imaging as a prelude to *in vivo* experiments. Long ‘in-bag’ <sup>129</sup>Xe polarization decay times have been measured ( $T_1$ ~38 min and ~5.9 hr at ~1.5 mT and 3 T, respectively)—more than sufficient for a variety of applications.

hyperpolarization | NMR&MRI | laser-polarized xenon

Owing to the detection sensitivity provided by their high, non-equilibrium nuclear spin polarization, hyperpolarized (HP) noble gases (e.g. <sup>129</sup>Xe and <sup>3</sup>He) are utilized in a number of NMR/MRI applications (1, 2). Human lung imaging (e.g., Refs. (3-7)) with HP<sup>129</sup>Xe is of particular interest. Moreover, xenon is soluble in blood (8), other tissues (9), and many biologically compatible liquids (10), and its proclivity for interacting with other substances and its wide chemical shift range make HP<sup>129</sup>Xe a sensitive NMR probe of molecular and material surfaces (1, 2, 11-13). In many NMR and MRI applications HP<sup>129</sup>Xe can replace <sup>3</sup>He, and the relative abundance of <sup>129</sup>Xe can greatly reduce the impact of the world-wide <sup>3</sup>He shortage (14) in these instances. Despite considerable progress (e.g., Refs. (15-23)), a major obstacle towards implementing HP<sup>129</sup>Xe for clinical imaging has been the ability to reliably and inexpensively produce large quantities of HP<sup>129</sup>Xe

with high polarization ( $P_{Xe}$ )[1]. HP<sup>129</sup>Xe is usually created via spin-exchange optical pumping (SEOP (24)), a process whereby the unpaired *electronic* spins of an alkali metal vapor (typically Rb) are polarized via depopulation optical pumping with circularly polarized laser light, and the polarization is subsequently transferred to noble gas *nuclear* spins during collisions. It is generally anticipated that high  $P_{Xe}$  values are achievable via SEOP only in the low xenon-density regime (19, 25), because: (a) higher Xe densities increase the destruction of the alkali metal polarization from non-spin-conserving collisions at a rate that is orders of magnitude worse than those of other gases like N<sub>2</sub> and He (26-28); and (b) higher total pressures tend to quench the three-body van der Waals contribution to Rb-Xe spin exchange—leaving the less-efficient two-body term to dominate (19, 24). Most large-scale polarizers, in particular all that are available commercially, operate in this low-Xe density regime. Applied research with HP<sup>129</sup>Xe is severely hampered owing to a lack of access to expensive proprietary commercial hyperpolarizers, and in order to stimulate development of HP<sup>129</sup>Xe applications, we present here a low cost, open-source design.

In our recent work (23, 29, 30) exploring batch-mode and stopped-flow (16) Rb/Xe SEOP under conditions of high resonant laser flux, an unexpected, inverse relationship was found between the optimal temperature for performing Rb/Xe SEOP and the in-cell Xe density. This effect was recently exploited to achieve surprisingly high  $P_{Xe}$  values at high in-cell Xe densities (e.g., ~52%, ~31%, ~22%, and ~11% at 50, 300, 500, and 2000 Torr Xe in a 75 cc cell) with <30 W of laser power (23). Expanding these small-scale experiments by over an order of magnitude and improving  $P_{Xe}$  is a scientific and engineering leap necessary for large-scale HP<sup>129</sup>Xe production suitable for applications in

## Reserved for Publication Footnotes

[1]For spin-1/2 particles like electrons and <sup>129</sup>Xe nuclei, polarization is defined as:  $P = (N_\alpha - N_\beta) / (N_\alpha + N_\beta)$ , where  $N_\alpha$  and  $N_\beta$  refer respectively to the numbers of spins in the  $\alpha$  ( $m_{S,I} = +1/2$ ) and  $\beta$  ( $m_{S,I} = -1/2$ ) magnetic sublevels; at thermal equilibrium,  $P_{Xe}$  is only  $\sim 2.85 \times 10^{-6}$  at 3 T and room temperature.

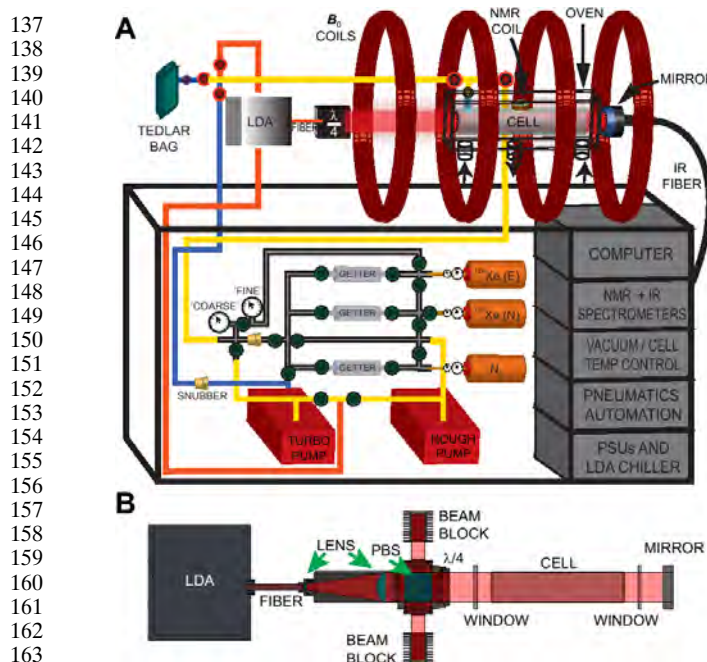


**Fig. 1.** (color online) The XeNA polarizer. (A)Schematic of the polarizer's key components (the liquid N<sub>2</sub> dewar that provides gas for oven heating and cooling is not shown). The optical path comprising beam expanding optics, polarizing beam-splitter cube, quarter-wave plate, and heat sinks is represented by ("λ/4"). For the gas cylinders, "N" and "E" designate xenon with naturally-abundant <sup>129</sup>Xe and isotopically-enriched <sup>129</sup>Xe, respectively. (B) Schematic showing the principal elements of the optical path.

humans. Here we present results[2] obtained with our collaboration's first-generation large-scale (~1 L/hr) <sup>129</sup>Xe polarizer for clinical, pre-clinical, and materials MRS/MRI applications. Comprised of mostly off-the-shelf components, our automated, modular polarizer is portable, easy to use, and employs an 'open-source' design that is readily implementable in other laboratories. Unlike most clinical-scale Xe polarizers, our hyperpolarizer runs in the xenon-rich gas regime (with up to 1800 Torr in a 500 cc optical pumping cell) in either single-batch or stopped-flow mode, in part negating the usual requirement to cryo-collect the HP <sup>129</sup>Xe—a process that otherwise increases the complexity of the device and can lead to significant losses of spin polarization during HP<sup>129</sup>Xe accumulation, storage, phase transitions (33), and transfer. Four independent methods were utilized to measure spin polarization, including: *in situ* field-cycled near-IR spectroscopy (29) (to probe Rb electron spin polarization); *in situ* low-field <sup>129</sup>Xe NMR (calibrated with thermal <sup>1</sup>H NMR); gas transfer to 47.5 mT for <sup>129</sup>Xe NMR (calibrated with thermal <sup>13</sup>C NMR); and gas transfer and subsequent <sup>129</sup>Xe NMR/MRI using a clinical 3 T scanner. Excellent agreement was observed among these different approaches; taken together, the <sup>129</sup>Xe polarization values reported here represent, by a significant margin, the highest yet achieved at such high Xe densities—and establish the feasibility of attaining near-unity polarization in single batches with HP<sup>129</sup>Xe quantities sufficient for clinical use. Long <sup>129</sup>Xe polarization lifetimes were obtained in Tedlar bags that are well-explained by current relaxation models (25), and that are more

[2]Portions of this work were presented previously in Refs. (31, 32).

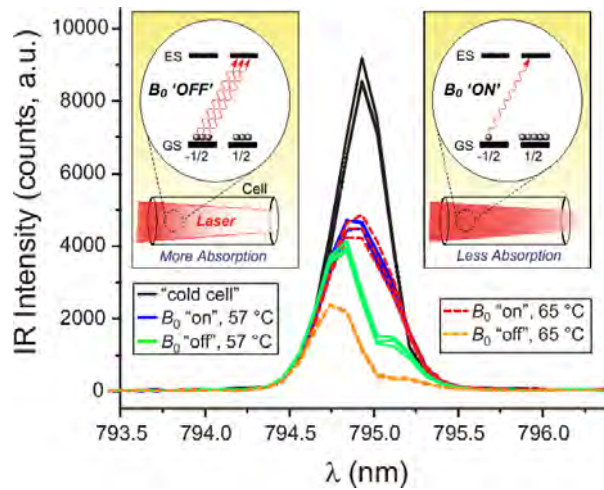


**Fig. 2.** (color online) *In situ* monitoring of global Rb electron spin polarization. Main figure: Examples of near-IR spectra of the pump laser transmitted through the cell acquired under the following conditions: room temperature ("cold cell", black solid lines); 57 °C and  $B_0=0$  mT (blue solid lines); 57 °C and  $B_0=5.26$  mT (green solid lines); 65 °C and  $B_0=5.26$  mT (red dashed lines); and 65 °C and  $B_0=0$  mT (orange dashed lines). Three scans for each condition are shown; error bars for  $\langle P_{Rb} \rangle$  values were determined by propagating the standard deviations of spectral integral values. Insets:Cartoons showing the effects of depletion pumping of electronic spin states of the alkali metal vapor on the transmitted laser intensity (assuming OP with with  $\sigma^+$  circularly polarized light; nuclear spin levels are not shown for simplicity). When the external magnetic field  $B_0$  is 'off' (left), optical pumping is highly inefficient, resulting in near-equal populations of the ground electronic spin states ( $m_J=+1/2$  &  $-1/2$ ) and a relatively high density of absorbers in the gas phase. The presence of an applied magnetic field provides a quantization axis and results in more efficient optical pumping. This results in unequal ground state populations, corresponding to high electronic spin polarization; the reduced number of atoms in the  $m_J=-1/2$  ground state gives rise to increased laser transmission (right).

than sufficient for gas-phase storage or accumulation necessary for some applications.

## Methods

**XeNA Polarizer.** Complete details of the design, components, assembly, and operation of our consortium's first-generation 'open-source' automated <sup>129</sup>Xe polarizer (dubbed "XeNA" for XEnon polarizatioN Automatized) will be provided elsewhere in a full report (Nikolaou et al., manuscript in preparation); however, brief descriptions of key aspects are provided below. XeNA is self-contained in a mobile chassis and is comprised of a laser system, an electromagnetic coil assembly, a vacuum / gas-handling manifold, on-board optical and NMR spectrometers (and other sensors) for quality assurance (QA) and feedback, and a computer/automation system (Fig. 1A).

The optical path (Fig. 1B) begins with a 200 W laser diode array (LDA, QPC Lasers) that produces frequency-narrowed (30) laser output at the Rb D<sub>1</sub> line (~794.8 nm; nominal FWHM~0.27 nm) The laser is tunable over >1 nm by adjusting the water-chiller temperature and/or the driving current, allowing the laser to be maintained on resonance at various output powers, as well as off-resonant SEOP (29, 30, 34). The laser beam passes through a short optical fiber preserving linear polarization and then expands to 2" diameter before collimation and entrance into a 2" polarizing beam-splitter (PBS) cube. The s-polarized beam component (<10% of incident power) is reflected 90° and discarded into a beam block; the main (p-polarized) beam is transmitted into a quarter-wave (λ/4) plate, which renders the beam circularly-polarized. This beam is then directed into the oven, which contains a cylindrical glass optical pumping cell (2" o.d., 9.75" long, 500 cc). Prior to installation the cell is coated with a silanizing agent (SurfSil, Pierce) to slow <sup>129</sup>Xe T<sub>1</sub> relaxation, and then loaded with <200 mg Rb in an inert atmosphere. SEOP may be performed once the cell has been loaded with a variable Xe/N<sub>2</sub> gas mixture. The N<sub>2</sub> gas helps suppress unwanted re-emission of non-polarized light from the electronically excited Rb (15) as well as other undesirable energetic processes (35); the N<sub>2</sub> also provides some additional collision-broadening of the Rb absorption line (36). The Teflon oven houses the cell and provides temperature control via a heated/cooling gas supply line from an external self-pressurized liquid N<sub>2</sub> dewar. The laser beam enters

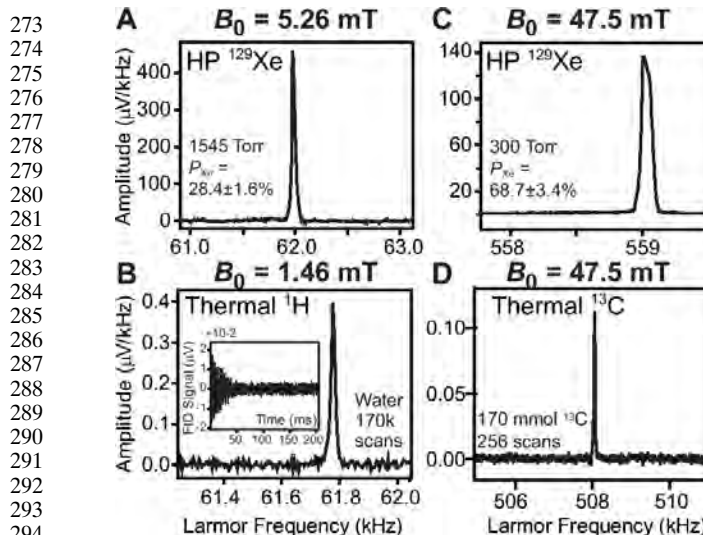


**Fig. 3.** (color online) Determination of  $^{129}\text{Xe}$  polarization at low and intermediate magnetic fields. (A) HP  $^{129}\text{Xe}$  NMR spectrum from the SEOP cell containing 1545 Torr Xe (and 455 Torr  $\text{N}_2$ ) acquired at 5.26 mT (62.0 kHz  $^{129}\text{Xe}$  frequency; 1 scan using a 59  $\mu\text{s}$  RF pulse corresponding to a  $30^\circ$  tipping angle—i.e.,  $T_{30} = 59 \mu\text{s}$ ). (B) Reference NMR spectrum from water  $^1\text{H}$  spins, 111 M  $^1\text{H}$  concentration, doped with 5 mM copper sulfate, thermally polarized at 1.46 mT (62.0 kHz  $^1\text{H}$  frequency; 170,000 scans;  $T_{30} = 16 \mu\text{s}$ ; TR=0.3 s;  $P_H = 5.0 \times 10^{-9}$ ). Inset:  $^1\text{H}$  FID for the spectrum in the main figure; SNR was used to calculate a relative error bar of 5.7% for  $P_{\text{Xe}}$  values calibrated with this signal. (C) HP  $^{129}\text{Xe}$  NMR spectrum recorded at 47.5 mT, 559 kHz  $^{129}\text{Xe}$  frequency, 1 scan, using  $T_{30} = 18 \mu\text{s}$  from a 52 mL spherical phantom following transfer of some of the cell contents (originally 300 Torr Xe, 1700 Torr  $\text{N}_2$ ) to the phantom. (D) Reference  $^{13}\text{C}$  NMR spectrum from 170 mmol of sodium 1- $^{13}\text{C}$  acetate, 14 g in 50 mL  $\text{D}_2\text{O}$ , also measured at 47.5 mT (508 kHz  $^{13}\text{C}$  frequency; 256 scans using  $T_{90} = 54 \mu\text{s}$ ; TR=200 s;  $P_C = 4.1 \times 10^{-8}$ ).

and exits through 3" anti-reflection (AR)-coated optical flats. The beam is retro-reflected back through the cell via a 3" mirror and directed into the optics assembly, where the PBS reflects the beam into a second beam block. The oven and cell reside in a homogeneous magnetic field provided by a four-coil electromagnet assembly (Acutran, 23.6" ID; nominal fields of 5.26 or 1.46 mT, corresponding to 62.0 kHz resonance frequency for  $^{129}\text{Xe}$  or  $^1\text{H}$ , respectively). The entire optics train and magnet assembly is contained in a light-tight Alumalite enclosure (MiniTec).

The manifold directs gas flow from high-pressure cylinders containing natural abundance xenon (26.44%  $^{129}\text{Xe}$ ), isotopically enriched xenon (~86%  $^{129}\text{Xe}$ ), and  $\text{N}_2$  gas, providing desired mixtures up to 2000 Torr total pressure. All experiments used naturally abundant  $^{129}\text{Xe}$  unless otherwise stated. Vacuum is provided by a mechanical rotary vane ('rough') pump and turbopump station (Edwards). After passing through  $\text{O}_2$  getters, the gases are loaded into the OP cell, with feedback provided by digital pressure gauges. Following SEOP, the HP $^{129}\text{Xe}$  mixture is flowed through PFA tubing and a Teflon filter (Millipore Wafergard) to get any residual Rb prior to collection in a Tedlar bag. The bag can be then detached and transported elsewhere for experiments. The glass valve on the OP cell has a mechanically actuated Teflon stopcock. The other manifold valves are automated pneumatic or solenoid valves, where Teflon surfaces are used for all valves downstream of the OP cell.

*In situ* QA for the SEOP process is provided by near-IR and NMR methods using an Ocean Optics HR4000 high-resolution near-IR optical spectrometer and a Magritek Kea2 low-field NMR spectrometer. The near-IR spectrometer detects via a fiber probe positioned immediately behind the 3" mirror. The NMR spectrometer uses a home-built NMR probe/surface coil. Both spectrometers are connected to the laptop computer mounted on the console. User operation of XeNA employs a GUI designed and programmed in open-source software (Processing.org), which drives a microcontroller box that houses the "brain" of the polarizer (an Arduino Mega 2560 REV3 microcontroller board), solid state relays, and a Burkert manifold enabling pneumatic valve operation. The micro-controller is responsible for control of all solenoid and pneumatic Teflon valves as well as communications with the oven temperature controller, pressure gauges, laser temperature monitor, and safety interlocks. Material costs for the hyperpolarizer were under \$125,000.

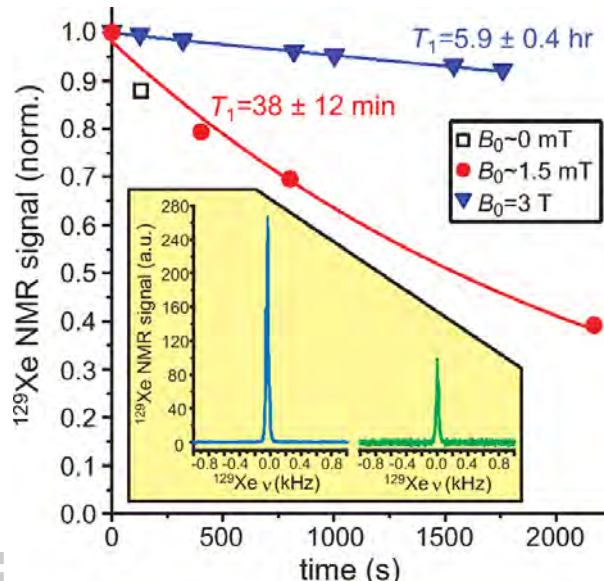


**Fig. 4.** (color online) High-field  $^{129}\text{Xe}$  measurements.  $T_1$  decay of normalized HP $^{129}\text{Xe}$  NMR signals from Xe gas transferred to Tedlar bags and measured at 3 T throughout the decay period (blue triangles) or stored at  $\sim 1.5$  mT (red circles) or  $\sim 0$  mT (white squares) and rapidly transferred to and from 3 T for brief acquisition periods. Loss from RF excitation pulsing was negligible, given a tipping angle of  $<1^\circ$ . Inset: Left:  $^{129}\text{Xe}$  NMR spectrum from HP $^{129}\text{Xe}$  in a Tedlar bag containing  $\sim 800$  cc gas, 38% Xe by volume following transport to a 3 T clinical MRI (34.09 MHz  $^{129}\text{Xe}$  frequency; one scan using  $1.4^\circ$  tipping-angle RF pulse). Gas compositions for this spectrum and the data in the main figure were nearly identical. Right: reference NMR spectrum from thermally polarized  $^{129}\text{Xe}$  spins in the 3 L spherical phantom containing a  $\text{Xe}/\text{O}_2$  mixture (32 scans with 90° RF pulses).

*Other experimental aspects.* Xenon was purchased from Nova Gases. MR spectra and images were obtained at 47.5 mT (37, 38) or 3 T field using a Magritek Kea2 with permanent magnet (559 kHz  $^{129}\text{Xe}$  frequency and 508 kHz  $^{13}\text{C}$  frequency) or a Siemens 3 T clinical MRI scanner (34.09 MHz  $^{129}\text{Xe}$  frequency), respectively. Elemental analysis of Tedlar bag contents (following SEOP runs) was performed by Element One (Wilmington, NC) to ensure that  $<5.0$  ng Rb was present in the bag after transfer.

## Results

An estimate of the spatial average of the Rb electron spin polarization,  $\langle P_{\text{Rb}} \rangle$ , can be obtained from measurement of the transmitted light of the pump laser while the magnetic field is cycled (29) (Fig. 2). Spectra are recorded from the laser beam transmitted through the cell in order to calculate absorbance values:

$$A = -\ln T = -\ln \left( \frac{I_{\text{hot}}}{I_{\text{cold}}} \right) \quad , \quad (1)$$

where  $A$  and  $T$  respectively denote the absorbance and transmittance, and  $I_{\text{hot}}$  and  $I_{\text{cold}}$  are the integrated intensities of the transmitted laser spectra obtained when a gas-loaded cell is respectively 'hot' and 'cold' (i.e., with and without significant Rb vapor present). With some simple assumptions, absorbance values may then be compared under the same conditions—except with or without the SEOP magnetic field ( $B_0$ ) on—in order to calculate an estimate of  $\langle P_{\text{Rb}} \rangle$ , according to a simple relation derived from Beer's Law (29):

$$\langle P_{\text{Rb}} \rangle = \frac{A}{A_0} - 1 \quad , \quad (2)$$

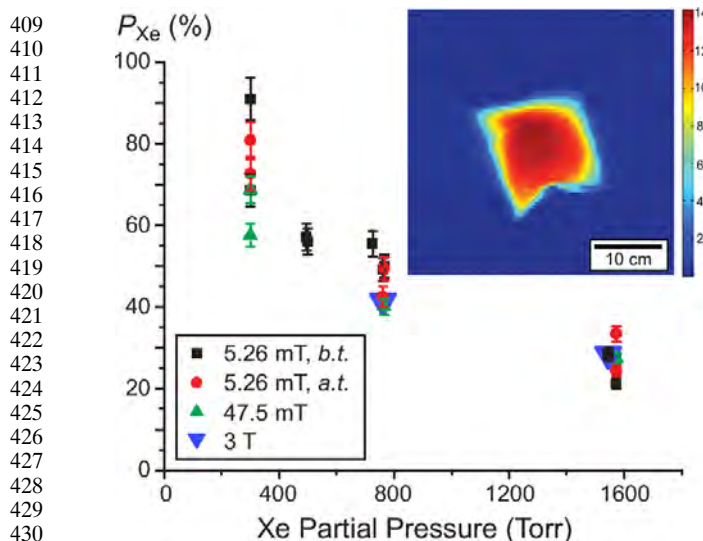


Fig. 5. (color online)  $^{129}\text{Xe}$  nuclear spin polarization values measured at 5.26 mT, 47.5 mT, and/or 3 T, plotted versus xenon partial pressure prior to SEOP. Labels ‘b.t.’ and ‘a.t.’ respectively refer to measurements obtained from Xe gas remaining within the SEOP cell before and after some of the gas was transferred to another container. Error bars are determined from the uncertainties in the spectral integral values obtained from the respective thermally-polarized reference samples. The value at 725 Torr was obtained with 82%-enriched  $^{129}\text{Xe}$ . Inset: 2D FLASH  $^{129}\text{Xe}$  projection image of hyperpolarized xenon gas in a Tedlar bag following transport to the 3 T MRI (FOV: 40 cm; slice thickness: 1.7 cm; matrix size: 80×80; TE/TR: 2.6/5.1 ms; RF tipping angle  $\sim 4^\circ$ ; and SNR  $\sim 40:1$ ).

where  $A_0$  is the absorbance when  $B_0=0$ . Examples of transmission spectra are shown in Fig. 2 for a cell containing 495 and 1300 Torr of Xe and  $\text{N}_2$ , respectively. Multiple near-IR spectra were obtained in rapid succession under a given set of conditions, and then averaged and integrated. One set of scans was obtained at 57 °C, roughly 10 minutes into the SEOP process; the corresponding values of  $\langle P_{\text{Rb}} \rangle$  and  $P_{\text{Xe}}$  measured with low-field NMR (see below) were  $43\pm9\%$  and  $48.3\pm2.8\%$ , respectively.[3] As part of the SEOP optimization process, the temperature of the cell was raised to 65 °C and after several minutes the sequence was repeated. Improved values of  $\langle P_{\text{Rb}} \rangle$  and  $P_{\text{Xe}}$  of  $71\pm6\%$  and  $57\pm3\%$ , respectively, were obtained.

The Xe polarization process was monitored directly via NMR under three different sets of conditions (Figs. 3&4). First, low-field  $^{129}\text{Xe}$  NMR can be used to measure  $P_{\text{Xe}}$  within the OP cell—during or after the SEOP process. Fig. 3A shows an example of a HP $^{129}\text{Xe}$  NMR spectrum obtained at 5.25 mT from a cell containing 1545 Torr Xe following SEOP and cool-down. Low-field NMR is calibrated using a thermal  $^1\text{H}$  reference signal obtained separately using the same NMR circuit at the same Larmor frequency of 62 kHz, and tuning/matching conditions detecting  $^1\text{H}$  at 1.46 mT from an identical cell filled with 5 mM CuSO<sub>4</sub> doped water (Fig. 3B). As part of our initial tests of the efficiency of the Xe-transfer process,  $P_{\text{Xe}}$  measurement was also performed at an intermediate field of 47.5 mT located approximately 2 m away from the polarizer. Fig. 3C shows an example of a HP $^{129}\text{Xe}$  NMR spectrum obtained at this field from a portion of HP $^{129}\text{Xe}$  within a cell containing 300 Torr Xe following automated transfer

to a ~50 cc polypropylene spherical phantom connected to the polarizer via  $\frac{1}{4}$  OD PFA tubing and located within the field of the permanent magnet.  $^{129}\text{Xe}$  polarization (here,  $68.7\pm3.4\%$ ) was calibrated using a thermal  $^{13}\text{C}$  reference signal obtained from 170 mmol of sodium 1 $^{13}\text{C}$  acetate in 99.8% D<sub>2</sub>O located in an identical phantom, Fig. 3D. Comparison with *in situ* 5.26 mT  $^{129}\text{Xe}$  NMR polarimetry taken from the OP cell during the same experiment before transferring the gas to 47.5 mT magnet ( $68.5\pm3.9\%$ ) indicated no polarization loss within error, and thus a highly efficient HP $^{129}\text{Xe}$  transport process.

The hyperpolarizer was delivered to Brigham & Women’s Hospital in Boston, MA and installed adjacent to a clinical MRI suite in February 2012. Optimization of the cell cool-down and automated Xe transfer process allowed Xe transfer to Tedlar bags via expansion and subsequent bag transport to a 3 T clinical MRI. The inset of Fig. 4 shows an example of a high-field HP $^{129}\text{Xe}$  NMR spectrum from a Tedlar bag containing ~800 cc gas (38% Xe by volume, given an initial cell loading of 760 Torr Xe / 1240 Torr N<sub>2</sub>). The  $P_{\text{Xe}}$  value is calibrated using a thermal  $^{129}\text{Xe}$  NMR signal from a 3 L spherical reference sample containing 4 atm Xe with 86%  $^{129}\text{Xe}$  enrichment and 2 atm O<sub>2</sub> with a  $T_1$  of 0.99 s. Again, little loss of polarization was suffered throughout the transfer / transport process, given values of  $42.8\pm2.4\%$  and  $41\pm2\%$  for  $P_{\text{Xe}}$  measured in the cell prior to transfer and at 3 T in the Tedlar bag, respectively. The latter % $P_{\text{Xe}}$  corresponds to a ~144,000-fold polarization enhancement over the thermal equilibrium value.\* The strong NMR signals obtained from the HP $^{129}\text{Xe}$  gas allowed the polarization decay to be monitored under a variety of conditions. Figure 4 shows  $^{129}\text{Xe}$   $T_1$  relaxation data for HP $^{129}\text{Xe}$  in Tedlar bags recorded at 3 T, but stored at different field strengths: following exponential fits,  $T_1$  decay times of  $38\pm12$  min and  $5.9\pm0.4$  hr were observed for  $^{129}\text{Xe}$  gas in Tedlar bags at 1.5 mT and 3 T, respectively. Such long  $T_1$  values bode well for a variety of applications where gas-phase storage and/or accumulation of HP $^{129}\text{Xe}$  is needed (25).

$^{129}\text{Xe}$  polarization values for various Xe densities, operating conditions, and measurement magnetic fields are summarized in Fig. 5. The data exhibit good run-to-run and method-to-method agreement across the various measurements for the given Xe cell loadings (~300–1600 Torr), despite the fact that the  $P_{\text{Xe}}$  values were measured at different fields, with different NMR acquisition methodologies, and different thermal reference samples. The data include values for in-cell  $P_{\text{Xe}}$  values of  $90.9\pm5.2\%$ ,  $57.1\pm3.3\%$ ,  $50.1\pm2.9\%$ , and  $33.4\pm1.9\%$  measured for Xe loadings of 300, 495, 765, and 1570 Torr, respectively;  $P_{\text{Xe}}$  values of  $41\pm1.6\%$  and  $28\pm1.1\%$  with ~760 and ~1545 Torr Xe loadings were obtained following transfer to Tedlar bags and subsequent transport to the 3 T scanner, permitting imaging with high SNR (~40) to be demonstrated, Fig. 5 inset. Moreover, these post-transfer values are ~2.7 times greater than previous bests in  $P_{\text{Xe}}$  achieved near such high Xe densities; when combined with the increase in cell volume, these results constitute a ~18-fold improvement in HP $^{129}\text{Xe}$  production over the previous best results obtained at such high in-cell Xe densities (23).

## Discussion

The overall performance of the polarizer is the result of a number of aspects of the SEOP process that are both fundamental and technical in nature (30). SEOP can be treated as a simple relaxation process (24), which at steady state, simplifies to give (16):

$$P_{\text{Xe}}(t=\infty) = \frac{\gamma_{\text{SE}}}{\gamma_{\text{SE}} + \Gamma_{\text{Xe}}} \langle P_{\text{Rb}} \rangle \quad , \quad (3)$$

[3]  $P_{\text{Xe}}$  cannot be higher than  $\langle P_{\text{Rb}} \rangle$  (see Eq. (3)); however, the difference between these values is less than the uncertainty.

545 where  $\gamma_{SE}$  is the Rb/Xe spin exchange rate and  $\Gamma_{xe}$  is the  $^{129}\text{Xe}$   
 546 nuclear spin destruction rate ( $=1/T_1$ ); thus, it is convenient to  
 547 categorize aspects of the hyperpolarizer and its operation as  
 548 factors that respectively help optimize  $\langle P_{Rb} \rangle$ ,  $\gamma_{SE}$ , and/or  $\Gamma_{xe}$ .  
 549 First, the most important factor in maximizing global  $\langle P_{Rb} \rangle$  is the  
 550 cell illumination by the laser. At a given position ( $r$ ) within the  
 551 cell, the local  $P_{Rb}$  is given by (16):  
 552

$$P_{Rb}(r) = \frac{\gamma_{OP}(r)}{\gamma_{OP}(r) + \Gamma_{SD}} \quad , (4)$$

556 Where  $\gamma_{OP}(r)$  is the local optical pumping rate (given by the  
 557 integrated product of the laser flux and the Rb absorption cross-  
 558 section (36)), and  $\Gamma_{SD}$  is the Rb electronic spin destruction  
 559 rate, which is dominated by non-spin-conserving collisions with  
 560 Xe (specifically, via the spin-rotation interaction (26, 28)) and  
 561 is high under our conditions because of its proportionality to  
 562  $[\text{Xe}]$ . Correspondingly, the laser power employed here is also  
 563 high—about 170 W for most experiments, mostly resonant or  
 564 near-resonant with the Rb D<sub>1</sub> line. In fact, the resonant photon  
 565 flux is roughly six-fold greater than in Ref. (23), but this increase  
 566 explains only part of the improvement in HP $^{129}\text{Xe}$  performance.  
 567 Care was also taken with the optical path to ensure complete  
 568 illumination throughout the optical pumping cell with near-unity  
 569 laser polarization, with no dark regions (either near the edges  
 570 or from longitudinal optical nodes), and with additional photon  
 571 flux provided by retro-reflection. Control of the cell temperature  
 572 is also key for SEOP optimization. Previously it was shown that  
 573 there can be an inverse relationship between Xe density and  
 574 the optimal temperature for SEOP, where higher  $[\text{Xe}]$  favors  
 575 lower cell temperatures (23, 30)—an effect that may be explained  
 576 in part by the need to maintain uniform illumination throughout  
 577 the cell. Although  $\gamma_{SE}$  is proportional to the Rb density  
 578 (39)—ostensibly favoring *higher* cell temperatures—maintaining  
 579 a high “photon-to-Rb” ratio (in part by *limiting* [Rb]) can be  
 580 particularly important for preserving global  $\langle P_{Rb} \rangle$  as Xe density  
 581 is increased, and Xe-induced Rb spin-destruction becomes domi-  
 582 nant.[4] For example, ongoing simulations (40) predict a high  $\Gamma_{SD}$   
 583 value of  $\sim 134,300 \text{ s}^{-1}$  for the experimental conditions of the  
 584 65 °C data in Fig. 2, dominated by Xe collisions (26–28). However,  
 585 the high resonant photon flux at the front of the cell should give  
 586 nearly a 9-fold greater optical pumping rate ( $\gamma_{OP} \sim 1.16 \times 10^6 \text{ s}^{-1}$ );  
 587 using Eq. (4), such values for  $\Gamma_{SD}$  and  $\gamma_{OP}$  would correspond to  
 588  $P_{Rb} \sim 89.6\%$ . Maintaining a relatively low Rb density allows the  
 589 laser to penetrate efficiently to ensure high photon flux and Rb  
 590 polarization throughout the cell, consistent with the experimental  
 591 value ( $\langle P_{Rb} \rangle = 71 \pm 6\%$ ). Thus, particularly in the limit where  
 592  $\Gamma_{xe}$  is negligible, maximizing  $\langle P_{Rb} \rangle$  is more important than  $\gamma_{SE}$ ,  
 593 once  $\gamma_{SE}$  is sufficiently high. Indeed, our high  $P_{xe}$  values were  
 594 enabled in part by our ability to achieve long in-cell  $^{129}\text{Xe}$   $T_1$   
 595 ( $=1/\Gamma_{xe}$ ) decay times. As one example, following SEOP with a  
 596 cell containing 495 Torr Xe and cool-down to 33 °C (where Rb  
 597 should be condensed), a cell  $T_1$  of  $1.9 \pm 0.6$  hr was measured at  
 598 5.26 mT. Given a typical build-up time constant measured for  
 599 one experiment of  $(\gamma_{SE} + \Gamma_{xe})^{-1} = 8.5$  min, this in-cell  $^{129}\text{Xe}$   $T_1$   
 600 translates to a spin-exchange rate of  $\gamma_{SE} \sim 1.8 \times 10^{-3} \text{ s}^{-1}$ —roughly an  
 601 order of magnitude greater than  $\Gamma_{xe}$ . Thus, according to Eq. (3)  
 602  $P_{xe}$  should closely approach  $\langle P_{Rb} \rangle$  under these conditions, again  
 603 in good agreement with the Fig. 2 experiments.

In addition to long HP $^{129}\text{Xe}$  relaxation times measured in OP cells, very slow polarization decay was also observed following

[4] An additional contribution to the interplay of Xe density and SEOP temperature may be poor energy dissipation caused by reduced thermal conductivity of the gas for Xe-rich mixtures—a possibility we are currently studying with *in situ* Raman spectroscopy (Whiting, Newton *et al.*, manuscripts in preparation).

transfer to Tedlar bags. Generally,  $^{129}\text{Xe}$  relaxation rates are  
 613 determined by several potential contributions (adapted from Ref.  
 614 (25)):

$$\Gamma_{xe} = \Gamma_i + \Gamma_g + \Gamma_{O2} + \Gamma_w \quad , (5) \quad 615$$

616 where  $\Gamma_i$  is the ‘intrinsic’—and essentially  
 617 unavoidable—contribution from spin-rotation interactions  
 618 of transient and persistent Xe-Xe dimers ( $\Gamma_i = \Gamma_t + \Gamma_p$  (41)),  $\Gamma_g$   
 619 results from diffusion through field gradients,  $\Gamma_{O2}$  results from  
 620 dipolar interactions with residual paramagnetic O<sub>2</sub> in the gas  
 621 mixture, and ( $\Gamma_w = \Gamma_{w,e-} + \Gamma_{w,N}$ ) includes contributions from  
 622 Xe/wall collisions involving interactions with surface spins of  
 623 unpaired electrons and nuclei, respectively.  $\Gamma_{w,e-}$  can be neglected for  
 624 Tedlar (polyvinyl fluoride); moreover  $\Gamma_g$  can be neglected for  
 625 the 3 T measurements given the homogeneous field. Saam and  
 626 co-workers recently provided a semi-empirical formula for  $\Gamma_i$   
 627 that when adapted for our conditions, is given by (25):  
 628

$$\Gamma_i = \frac{[Xe]}{56.1 \text{ hr}} + \frac{1}{4.59 \text{ hr}} \left[ 1 + (3.65 \times 10^{-3}) B_0^2 \left( 1 + 0.51 \frac{[N_2]}{[Xe]} \right)^{-1} \right] \quad , (6) \quad 629$$

630 where the two additive terms respectively correspond to  $\Gamma_t$  and  
 631  $\Gamma_p$ ,  $B_0$  is in Tesla, the gas densities are in amagat[5], and 0.51 is  
 632 a factor that takes into account the differential break-up rate of  
 633 persistent Xe dimers from collisions with N<sub>2</sub>. Using values for  
 634 [Xe] and [N<sub>2</sub>] of 0.35 and 0.58 amg, Eq. (6) predicts a limiting  
 635 value of  $1/\Gamma_{xe} = 7.8$  hr (with 10% uncertainty), in relatively good  
 636 agreement with our experimental value of  $5.9 \pm 0.4$  hr at 3 T,  
 637 and indicating effective suppression of other relaxation pathways.  
 638 Given the expected absence of paramagnetic wall sites, if we  
 639 assume that (a) relaxation from wall collisions involving surface  
 640 nuclear spins (42) (e.g., <sup>1</sup>H and <sup>19</sup>F) is essentially quenched at  
 641 high field and (b) that the remaining contribution to  $\Gamma_{xe}$  is from  
 642 residual O<sub>2</sub> (with a relaxivity of  $\sim 0.4$  Hz/amg (43)), then the  
 643 differential relaxation rate would correspond to an upper limit for  
 644 the O<sub>2</sub> partial pressure of  $\sim 2 \times 10^{-2}$  Torr—a reasonable amount.  
 645 While  $\Gamma_p$  is the limiting factor for our high-field  $^{129}\text{Xe}$  relaxation,  
 646 the accelerated decay at 1.5 mT ( $T_1 = 38 \pm 12$  min) is consistent  
 647 with  $\Gamma_{w,N}$  providing the dominant mechanism. Driehuys *et al.* (42)  
 648 showed that at low field ( $\sim 0$ –10 mT), dipolar relaxation with  
 649 <sup>1</sup>H ‘wall’ spins was the primary contributor to  $^{129}\text{Xe}$  polarization  
 650 decay in cells with organosilane coatings, with  $T_1 < 50$  min at  
 651 1.5 mT and 297 K. Although Tedlar may lack the nanoscale Xe  
 652 permeability of SurfaSil coatings (42), it does possess a high sur-  
 653 face density of <sup>1</sup>H and <sup>19</sup>F spins and likely provides an attractive  
 654 surface for transient Xe adsorption. More detailed studies of  
 655  $^{129}\text{Xe}$  relaxation in Tedlar containers will be the subject of future  
 656 efforts.

657 On a technical level, SEOP efficiency is aided by the presence  
 658 of *in situ* monitoring of the Rb spectral absorption and  $^{129}\text{Xe}$   
 659 NMR signals, which provide immediate feedback to allow optimi-  
 660 zation of the SEOP process in real time. Afterwards, additional  
 661  $^{129}\text{Xe}$  polarization losses are mitigated by (a) rapid cool-down of  
 662 the cell while reducing the resonant laser power in kind (to further  
 663 decrease the heat load, while still providing sufficient illumination  
 664 to avoid “dark” Rb—a procedure that allows only a few percent  
 665 loss of  $P_{xe}$ ), as well as (b) suppressing exposure to O<sub>2</sub> and other  
 666 paramagnetic materials throughout the gas lines, (c) moving the  
 667 HP $^{129}\text{Xe}$  quickly into the sample or transport vessel, and (d)  
 668 avoiding Xe phase transitions and other relaxation-susceptible  
 669 portions of the Xe phase diagram (33). Indeed, Xe cryo-collection  
 670

[5] 1 amagat (amg) =  $2.6873 \times 10^{19} \text{ cm}^3$ , equal to the density of an ideal gas at 0 °C and  
 760 Torr.

681	/sublimation prior to transfer to the sample is optional for XeNA,	749
682	but it is normally a requirement with other polarizer designs	750
683	operating with standard "xenon-lean" gas mixtures. We should	751
684	add that not cryo-collecting the Xe does result in dilution of the	752
685	HP <sup>129</sup> Xe with N <sub>2</sub> gas and leaves behind significant fractions of	753
686	the SEOP mixture in the cell following the expansion process;	754
687	however, both of these issues can be mitigated respectively by	755
688	using Xe-rich mixtures and by the addition of a large automated	756
689	gas piston (16) where the cell contents can be expanded into a	757
690	much larger volume prior to transfer to the sample or transport	758
691	vessel.	759
692	<b>Conclusion</b>	760
693	We have presented results from a clinical-scale ( $\sim 1$ L/hr)	761
694	hyperpolarizer that produces batches of spin-polarized <sup>129</sup> Xe	762
695	sufficient for clinical use. The polarizer's 'open-source' design	763
696	and automated operation should facilitate implementation of	764
697	HP <sup>129</sup> Xe technology into other labs, including clinical settings.	765
698	Good agreement was obtained among the four independent	766
699	methods for characterizing the spin polarization. The ability to	767
700	achieve high $P_{Xe}$ values at high Xe densities, combined with	768
701	stopped-flow operation, negates the usual requirement of Xe	769
702		770
703		771
704	1. Goodson BM (2002) Nuclear magnetic resonance of laser-polarized noble gases in molecules, materials, and organisms. <i>J Magn Reson</i> 155:157-216.	772
705	2. Bifone A & Cherubini A (2003) Hyperpolarised Xenon in Biology. <i>Prog Nucl Magn Reson Spectrosc</i> 42:1-30.	773
706	3. Mugler JP, et al. (1997) MR imaging and spectroscopy using hyperpolarized Xe-129 gas: Preliminary human results. <i>Magn Reson Med</i> 37:809-815.	774
707	4. Lewoods JC, et al. (2001) Hyperpolarized He-3 gas production and MR imaging of the lung. <i>Concepts Magn Reson</i> 13:277-293.	775
708	5. Moller HE, et al. (2002) MRI of the Lungs Using Hyperpolarized Noble Gases. <i>Magn Reson Med</i> 47:1029-1051.	776
709	6. Bidinosti CP, et al. (2004) MRI of the lung using hyperpolarized He-3 at very low magnetic field (3 mT). <i>Magn Reson Mat Phys Biol Med</i> 16:255-258.	777
710	7. Patz S, et al. (2007) Hyperpolarized Xe-129 MRI: A viable functional lung imaging modality? <i>Eur J Radiol</i> 64:335-344.	778
711	8. Bifone A, et al. (1996) NMR of laser-polarized xenon in human blood. <i>Proc Natl Acad Sci USA</i> 93:12932-12936.	779
712	9. Chen RY, et al. (1980) Tissue-blood partition coefficient for xenon: temperature and hematocrit dependence. <i>J Appl Physiol</i> 49:178-183.	780
713	10. Acosta RH, Blümlein P, Münnemann K, & Spiess H-W (2012) Mixture and dissolution of laser polarized noble gases: Spectroscopic and imaging applications. <i>Prog Nucl Magn Reson Spectrosc</i> 66:40-69.	781
714	11. Rubin SM, et al. (2000) Evidence of nonspecific surface interactions between laser-polarized xenon and myoglobin in solution. <i>Proc Natl Acad Sci USA</i> 97:9472-9475.	782
715	12. Jansch HJ, Gerhard P, & Koch M (2004) Xe-129 on Ir(111): NMR study of xenon on a metal single crystal surface. <i>Proc Natl Acad Sci USA</i> 101:13715-13719.	783
716	13. Schroder L, et al. (2006) Molecular imaging using a targeted magnetic resonance hyperpolarized biosensor. <i>Science</i> 314:446-449.	784
717	14. Shea DA & Morgan D (2010) The Helium-3 Shortage: Supply, Demand, and Options for Congress.	785
718	15. Driehuys B, et al. (1996) High-volume production of laser-polarized Xe-129. <i>Appl Phys Lett</i> 69:1668-1670.	786
719	16. Rosen MS, et al. (1999) Polarized 129Xe optical pumping/spin exchange and delivery system for magnetic resonance spectroscopy and imaging studies. <i>Rev Sci Instrum</i> 70:1546-1552.	787
720	17. Ruth U, et al. (1999) Production of nitrogen-free, hyperpolarized 129Xe gas. <i>Appl Phys B</i> 68:93-97.	788
721	18. Zook AL, Adhyaru BB, & Bowers CR (2002) High capacity production of > 65% spin polarized xenon-129 for NMR spectroscopy and imaging. <i>J Magn Reson</i> 159:175-182.	789
722	19. Mortuz MG, et al. (2003) Spin-exchange optical pumping of high-density xenon-129. <i>J Chem Phys</i> 118:1581-1584.	790
723	20. Knagge K, Prange J, & Raftery D (2004) A continuously recirculating optical pumping apparatus for high xenon polarization and surface NMR studies. <i>Chem Phys Lett</i> 397:11-16.	791
724	21. Ruset IC, Ketel S, & Hersman FW (2006) Optical Pumping System Design for Large Production of Hyperpolarized 129Xe. <i>Phys Rev Lett</i> 96:053002.	792
725	22. Schrank G, Ma Z, Schoeck A, & Saam B (2009) Characterization of a low-pressure high-capacity Xe-129 flow-through polarizer. <i>Physical Review A</i> 80: 063424.	793
726	23. Whiting N, et al. (2011) Interdependence of Xenon Density and Temperature on Rb/129Xe Optical Pumping Efficiency at High Xenon Densities. <i>J Magn Reson</i> 208:298-304.	794
727	24. Walker T & Happen W (1997) Spin-exchange optical pumping of noble-gas nuclei. <i>Rev Mod Phys</i> 69:629-642.	795
728	25. Anger BC, et al. (2008) Gas-phase spin relaxation of 129Xe. <i>Phys Rev A</i> 78(4):043406.	796
729		797
730		798
731		799
732		800
733		801
734		802
735		803
736		804
737		805
738		806
739		807
740		808
741		809
742		810
743		811
744		812
745		813
746		814
747		815
748		816